Development of a CFD Model for Stirred Tank applications

by

Darnell Francois Engelbrecht

Thesis presented in partial fulfillment for the Degree of Master of Science

In the Department of Mechanical Engineering
University of Cape Town

November 13, 2006

Abstract

Stirred tanks are widely used in industry for industrial processes such as mixing, wastewater treatment and flotation processes. Computational fluid dynamics (CFD) provides a useful tool for determining detailed information about the flow fields in stirred tanks. Many numerical studies have been carried out on single phase flow fields, however, multiphase studies have not been investigated as comprehensively. The development of multiphase CFD models of stirred tanks has significant implications for industrial processes. Existing processes could be optimized while predictive models could aid in the design of flotation systems. For example, important processes such as bubble-particle collision, attachment and detachment could be characterized in terms of stirred tank hydrodynamics. In addition, collector and frother models could be incorporated into CFD models to predict the flotation process in greater detail.

This thesis deals with the development of a multiphase model for stirred tank applications. The general purpose, commercially available CFD code, FLUENT 6.2, is used to model a Rushton turbine-agitated stirred tank with $T = 0.14$ m.

A single phase model was developed as a basis for the multiphase model. The MRF impeller model was used in conjunction with the standard k-ϵ turbulence model to model the impeller rotation and turbulence respectively. The higher order QUICK discretisation scheme was used for all single phase simulations. The single phase data was primarily evaluated in axial profiles of mean velocity and turbulent kinetic energy. In addition, the single phase data was also evaluated in terms of mean and turbulent RMS velocities, turbulent dissipation rates and power draw.

The MRF and sliding mesh models were used for the multiphase model. The Eulerian mixture model was used in conjunction with the dispersed k-ϵ turbulence model to model turbulence. The spargers in the stirred tank were modeled as velocity inlets and a single bubble size (0.2 mm) was assumed. The higher order QUICK discretisation scheme was used for the sliding mesh model, while first order upwind differencing was used for the MRF model. Initial concentrations of gas hold up, i.e., 0.15 % (GH 1), 25 % (GH 2) and 70 % (GH 3) of the experimental gas hold up reported by Deglon (1998), were patched into the stirred tank with a view to shortening calculation times.

A solution from a MRF simulation (GH 4) was also used as the input to the sliding mesh model for the same reason. Initial concentrations of gas hold up were not patched into the tank for MRF simulations, as these calculations times are substantially shorter than those of the sliding mesh. The effect of grid density on the flow field was investigated using the MRF model. The multiphase model was evaluated primarily in terms of mean and turbulent RMS velocities, turbulent dissipation rates, power draw and gas hold up. In addition, axial profiles of mean velocity and turbulent kinetic energy were also used to compare the multiphase data to published experimental data.

It was found that the single phase model accurately predicted the axial mean velocity and turbulent kinetic energy profiles. Bulk tank data poorly predicted experimental mean and turbulent RMS velocities as well as turbulent dissipation rates. The poor correlation was attributed to inaccuracies associated with the experimental measurement technique used to measure these parameters. Mean velocity predictions in the impeller stream and at the impeller tip were satisfactory and good, respectively. RMS velocity predictions were good in the impeller stream and satisfactory at the impeller tip, while turbulent dissipation rate predictions were good in the impeller stream and at the impeller tip. Power draw predictions were accurate for all simulations.

Axial profiles of mean velocity and turbulent kinetic energy for the multiphase model showed good correlation with published experimental and numerical profiles. However, for sliding mesh simulations, profiles corresponding to concentrations of gas hold up which were patched into the stirred tank (GH 1, GH 2 and GH 3) were inconsistent with increasing impeller rotations. No such inconsistencies were observed for profiles resulting from the use of the MRF solution (GH 4) as an input to the sliding mesh model. The fact that profiles corresponding to GH 1, GH 2 and GH 3 were not identical for increasing impeller rotations indicated that the flow fields corresponding to these initial patched concentrations were not fully developed. Profiles corresponding to the MRF simulations,to determine the effect of grid density, showed good correlation with the published experimental and numerical data.

Bulk tank data poorly predicted mean and turbulent RMS velocities as well as turbulent dissipation rates. The reason is the same as for the single phase model. For the sliding mesh model, mean velocity predictions in the impeller stream and at the impeller tip were accurate, apart for simulations corresponding to GH 1. Predictions correspond-

ing to GH 1 were, for the most part, inconsistent with predictions corresponding to GH 2, GH 3 and GH 4. Turbulent RMS velocities were satisfactory in the impeller stream and the impeller tip, but poor correlation was observed for turbulent dissipation rate at the impeller tip for both impeller models. This poor correlation was attributed to the difference in measurement techniques used in this study and the study carried out by Deglon (1998).

Power draw was accurately predicted by both impeller models and it was found that power draw was unaffected by gas hold up. Gas hold up was found to be dependent on the initial gas hold up in the stirred tank. Furthermore, both impeller models under predicted the experimental gas hold up due to the absence of collectors and surfactants in the numerical model.

It was concluded that the single phase model could accurately predict single phase experimental data. Furthermore, it was concluded that patching initial concentrations of gas hold up into the stirred tank did not produce a fully developed flow field, even after 30 impeller rotations. It is therefore recommended that the solution to an MRF simulation be used as the input to the sliding mesh model, as this case produced consistent results.

Declaration

I hereby declare that the above thesis is my own unaided work, both in conception and execution and that apart from the normal guidence of my supervisors, I have received no assistance apart from that stated below. Except as stated below, neither substance or any part of the thesis has been submitted in the past, or is being, or is to be submitted for a degree in the University or any other University. In addition, I hereby grant the University free license to reproduce the above thesis in whole or in part, for the purpose of research.

Signature of Candidate ..... Date 17 NOVEMBER 2006

Darnell Francois Engelbrecht

Signed by candidate

Acknowledgments

First and foremost, I would like to thank my parents for their love, guidance, support and understanding for 24 years. I would like to dedicate this to them. I would also like to thank my brother and sister for their guidance and support over the years.

Special thanks to my co-supervisor, Dr Dave Deglon for constructive criticism and guidance throughout this project. Special thanks also to my supervisor, Dr Chris Meyer, for his guidance throughout this project as well as insightful philosophical conversations about everything and anything. I wish you well for your trip to Norway and would say break a leg, but...

I would like to thank Danie de Kock at Qfinsoft for technical support.

Thanks also to Dwain Dunn for superb technical support for two years. Combined thanks to Amy Barty, Vaneshen Naidoo, Dwain Dunn, JP Pelteret and Kevin Appa for their parts in "D's Law" and other things we spoke about that might not interest anybody else but Verimark and Glomail at best. Good times...

Thanks also to Wendall Coenraad for proof reading the first part of this thesis. To all my friends from home, there are too many names so I wont mention them. Thanks for beer, parties, trips to Cape Town, movies, more beer...I couldn't have done any of this without your support.

Many thanks to interlibrary loans at UCT for getting me almost all the papers in my references. I would have no literature review were it not for them.

Last but not least, thanks to people like Anthea Heideman, Adri La Meyer, Tom Brakel, Vahid Monadjem, Nazneen Karbanee and Haneem Hendricks for being calming influ-

ences for the past 2 to 6 years.

My biggest thanks, however, must be reserved for the SAB, Boddingtons, Guinness, Mitchells, Grolsch and other countless breweries. When I got knocked down, the idea of a certain pub ale always got me going again.

Contents

Nomenclature

Symbols

a Averaged

b_i Body force (N)

C Off bottom impeller clearance (m)

C_μ, $C_{1\epsilon}$, $C_{2\epsilon}$ k-ϵ model constants $(dimensionless)$

C_D Drag coefficient $(dimensionless)$

D Impeller diameter (m)

F Force (N)

f Drag function $(dimensionless)$

g Gravitational acceleration $(m.s^{-2})$

G_k Generation of turbulent kinetic energy $(kg.m^{-1}s^{-3})$

H Height of fluid in tank (m)

d_b Bubble diameter (m)

J Baffle width (m)

J_g Superficial gas velocity (ms^{-1})

K Interphase momentum coefficient $(kg.m^{-3}s^{-1})$

k Turbulent kinetic energy $(m^2.s^{-2})$

L Impeller blade width (m)

$\dot{m}$ Mass transfer $(kg.s^{-1})$, mass flow rate $(kg.s^{-1})$

M Number of secondary phases

N Angular velocity $(m.s)$

p Pressure (Pa)

Pe Peclet number $(dimensionless)$

R Interaction term $(kg.m^{-2}s^{-1})$

r Radial distance from impeller (m)

Re Reynolds number $(dimensionless)$

S_i Source Term

T Tank height (m)

t Time (s)

$\overline{u}$ Time-averaged velocity $(m.s^{-1})$

u Velocity $(m.s^{-1})$

u', v', w' Turbulent fluctuating velocity $(m.s^{-1})$

U_θ Tangential velocity $(m.s^{-1})$

U_r Radial velocity $(m.s^{-1})$

U_z Axial velocity $(m.s^{-1})$

u_{swarm} Bubble-swarm velocity $(m.s^{-1})$

U_{tip} Impeller tip velocity $(m.s^{-1})$

$\overrightarrow{v}_{dr}$ Drift velocity $(m.s^{-1})$

W Impeller blade height (m)

x Cartesian coordinate direction (m)

z Vertical distance from tank bottom (m)

Greek Symbols

α Volume fraction (*dimensionless*)

δ Kronecker delta

Δt Time step (s)

ϵ Turbulent energy dissipation rate ($m^2.s^{-3}$)

Γ Diffusion coefficient

μ Dynamic viscosity ($kg.m^{-1}s^{-1}$)

μ_t Turbulent viscosity ($kg.m^{-1}s^{-1}$)

ω Specific dissipation rate (s^{-1})

ϕ Gas Holdup (*dimensionless*), Arbitrary transported variable

Π_{ϵ_q} Dispersed turbulence coefficient

Π_{k_q} Dispersed turbulence coefficient

ρ Density ($kg.m^{-3}$)

$\widehat{\rho}$ Effective density ($kg.m^{-3}$)

σ_k, σ_ϵ Turbulent Prandtl numbers (*dimensionless*)

$\overline{\overline{\tau}}$ Strain tensor

τ_p Particulate relaxation time (s)

ε_{ijk} Permutation operator

δx Characteristic length (m)

Subscripts

ϵ Turbulent dissipation rate ($m^2.s^{-3}$)

i Coordinate direction (*dimensionless*), Instantaneous

j Coordinate direction (*dimensionless*)

k Turbulent kinetic energy ($m^2.s^{-2}$)

l Coordinate direction (*dimensionless*)

p Phase p

q Phase q

s Solids phase

Acronyms

CFD Computational Fluid Dynamics

DNS Direct Numerical Simulation

Exp Experimental

GH Gas hold up (*dimensionless*)

I-O Inner-Outer

IBC Impeller Boundary Conditions

IR Impeller Rotations

LDV Laser Doppler Velocimetry

LES Large Eddy Simulation

MRF Multiple Reference Frames

QUICK Quadratic Upwind Interpolation Differencing Scheme

RANS Reynolds Averaged Navier-Stokes

RMS Root-Mean Squared

SM Sliding Mesh

TKE Turbulent Kinetic Energy ($m^2.s^{-2}$)

UD Upwind differencing

Glossary

Averaged	Referring to instantaneously measured data averaged circumferentially.
Bulk Tank	Outer region of the stirred tank, excluding the region encapsulating the impeller.
Gas Hold Up	Fraction by volume of the gas phase in the mixture.
Impeller Discharge Stream	Region of the stirred tank swept by the outflow of the impeller. Also known as the impeller swept region or impeller discharge stream.
Instantaneous	Referring to instantaneously measured data.
Lower Vortex	Vortex formed in the region below the impeller as a result of the radial flow pattern induced by the impeller.
Mid Baffle Plane	Measurement plance located midway between two baffles.
Off Bottom Clearance	Clearance between the impeller and bottom of the tank.

Patching	Specifying values of an arbitrary variable in one or more cell zones.
Reynolds Stresses	The mean forces imposed on the flow field by turbulent velocity fluctuations.
Superficial Gas Velocity	The volume per unit time of gas entering the tank divided by the tank cross-sectional area.
Upper Vortex	Vortex formed in the region above the impeller as a result of the radial flow pattern induced by the impeller.

List of Figures

List of Tables

Chapter 1

Introduction

Stirred tanks are widely used in many industrial processes such as mixing, wastewater and flotation processes. Baffled tanks are used most frequently, as the baffles prevent solid body rotation which hinders mixing. Stirred tanks can be agitated by a range of impellers, depending on the flow field required. Factors such as off bottom clearance (C) and clearance between the impeller and baffles also influence the flow field. Extensive

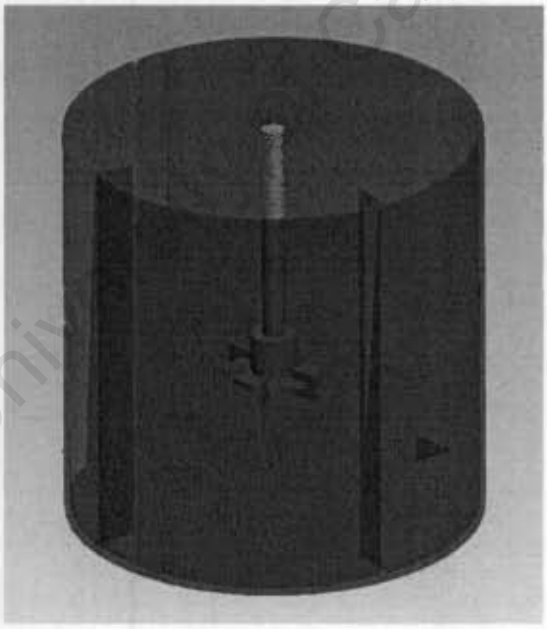

Figure 1.1: Baffled stirred tank agitated by a Rushton turbine

experimental studies (Cutter, 1966; van't Riet and Smith, 1973, 1975; Günkel and Weber, 1975; van der Molen and van Maanen, 1978; Yianneskis et al., 1987; Costes and Couderc, 1988; Wu and Patterson, 1989; Wu et al., 1989) have been carried out on single phase flows in stirred tanks. The influence of previously mentioned parameters, such as

off bottom clearance as well as impeller type, on the flow field has been reported. The single phase flow field is therefore well understood in terms of turbulence parameters, power draw and mean velocities.

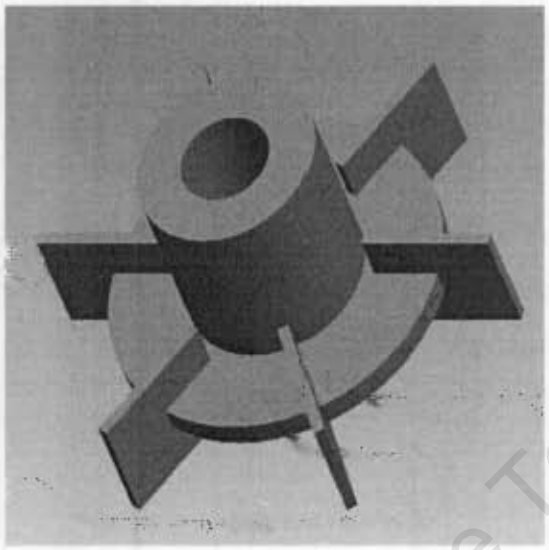

Figure 1.2: Rushton turbine impeller

Computational Fluid Dynamics (CFD) is a useful tool for determining detailed information about the flow field in stirred tanks. Many numerical studies (Ranade et al., 1989; Kresta and Wood, 1991; Luo et al., 1993; Tabor et al., 1996; Ranade, 1997; Brucato et al., 1998; Jenne and Reuss, 1999; Campolo et al., 2003; Aubin et al., 2004; Siwale, 2004; Hartmann et al., 2004; Deglon and Meyer, 2006) have been carried out on single phase flow fields. Turbulence parameters, power draw and mean velocities were often found to be accurately predicted by CFD.

Numerically, multiphase flows in stirred tanks have not been investigated as comprehensively as single phase flows. However, studies have been presented by Bakker (1992), Gosman et al. (1992), Ranade and van den Akker (1994), Ranade and Deshpande (1999), Koh et al. (2000) and more recently by Lane et al. (2002), Deen et al. (2002), Koh and Schwarz (2003), Gentric *et al* (2005), Kerdouss et al. (2006), Khopkar et al. (2005) and Sun et al. (2006). The development of multiphase CFD models of stirred tanks has significant implications for industrial applications. Existing processes could be optimized and streamlined while predictive models could also aid in the design of bubble columns and flotation systems. For example, important flotation subprocesses

such as bubble-particle collision, attachment and detachment could be characterized in terms of stirred tank hydrodynamics. In addition to this, collector and frother models could be developed to predict the flotation process in greater detail.

The purpose of this study was to develop a multiphase model for a Rushton turbine-agitated stirred tank. The sliding mesh and MRF impeller models will be used to model the impeller rotation, while the k-ϵ turbulence model will be used to model turbulence. The multiphase model will be primarily evaluated in terms of gas hold up and power draw, while mean velocity and turbulence parameters will also be of interest.

This thesis begins with a literature review, where key aspects of CFD are discussed and a review of multiphase studies on stirred tanks in CFD is presented.

The CFD methodology for this thesis is presented in Chapter 3. Boundary conditions specific to the each impeller model and the secondary (gas) phase as well as those applicable to the single and multiphase models are described. The chapter is concluded with a description of techniques for reproducing phase averaged and phase resolved experimental data.

The results for the single phase and multiphase models are presented in Chapter 4. The single phase model was evaluated in terms of axial profiles of mean velocity and turbulent kinetic energy. An extensive single phase experimental data set published by Wu and Patterson (1989) as well as a numerical data set presented by Siwale (2004) were used to validate the single phase model. The single phase model was then further validated in terms of mean velocities, turbulence parameters and power draw using experimental data published by Deglon (1998). The multiphase model was validated using a multiphase experimental data set, containing detailed turbulence parameter information for an aerated stirred tank, published by Deglon (1998). The multiphase model was evaluated in terms of mean velocity, turbulence parameters, power draw and gas hold up. In addition, axial profiles of mean velocity and turbulent kinetic energy were compared to those published by Wu and Patterson (1989) and Siwale (2004).

The thesis is concluded in Chapter 5 and recommendations are made based on the conclusions drawn.

Chapter 2

Literature Review

This literature review begins with an overview of the governing equations of fluid flow followed by an overview of discretisation, turbulence modeling and grid resolution. Impeller modeling techniques are subsequently presented, followed by a description of numerical multiphase models. The literature review is concluded with a review of multiphase modeling of stirred tanks using CFD.

2.1 Governing Equations

The conservation equations which govern fluid flow are given by the continuity and Navier-Stokes equations, which are time-averaged to yield the Reynolds averaged Navier-Stokes equations. These sets of equations are presented below.

2.1.1 Continuity Equation

The continuity (mass) equation for a general case, it is given by

$$\frac{\partial \rho}{\partial t} + \frac{\partial}{\partial x_i}(\rho u_i) = 0 \tag{2.1}$$

For an incompressible fluid, the continuity equation is given by

$$\frac{\partial}{\partial x_i}(\rho u_i) = 0 \tag{2.2}$$

2.1.2 Navier-Stokes Equations

The Navier-Stokes equations govern fluid flow. They are given by the momentum equations in each of the coordinate directions. The momentum equation is given by

$$\frac{\partial}{\partial t}(\rho u_i) + \frac{\partial}{\partial x_j}(\rho u_i u_j) = \rho b_i - \frac{\partial p}{\partial x_i} + \mu(\frac{\partial}{\partial x_i}[\frac{\partial u_i}{\partial x_j} + \frac{\partial u_j}{\partial x_i}] - \frac{2}{3}\frac{\partial u_k}{\partial x_k}) + S_i \tag{2.3}$$

Where S_i is a momentum source term.

2.1.3 Time Averaging

Through time averaging, transported properties can be divided into average and fluctuating components. For example, velocity can be written as

$$u_i = \overline{u}_i + u_i^{'} \tag{2.4}$$

Where $\overline{u}_i$ and $u_i^{'}$ are the average and fluctuating velocity components. The average velocity is defined by

$$\overline{u}_i = \frac{1}{t}\int_{t_1}^{t_2} u_i dt \tag{2.5}$$

Where $t_1 \ll t \ll t_2$. After many cycles of time averaging, the fluctuating components, given by $u_i^{'}$ in equation 2.4, average to zero (Marshall and Bakker, 2003). Scalar quantities, such as pressure, can be defined in a similar manner to equations 2.4 and 2.5. Substituting the time averaged equations into the instantaneous continuity and momentum equations yields

$$\frac{\partial}{\partial x_i}(\rho\overline{u}_i) = 0 \tag{2.6}$$

and

$$\frac{\partial}{\partial t}(\rho\overline{u}_i) + \frac{\partial}{\partial x_j}(\rho\overline{u}_i\overline{u}_j + \rho\overline{u_i^{'}u_j^{'}}) = \rho b_i - \frac{\partial p}{\partial x_i} + \mu(\frac{\partial}{\partial x_i}[\frac{\partial \overline{u}_i}{\partial x_j}) + \frac{\partial \overline{u}_j}{\partial x_i}] - \frac{2}{3}\frac{\partial \overline{u}_k}{\partial x_k}) + S_i \tag{2.7}$$

Equation 2.7 can be rewritten as

$$\frac{\partial}{\partial t}(\rho\overline{u}_i) + \frac{\partial}{\partial x_j}(\rho\overline{u}_i\overline{u}_j) = \rho b_i - \frac{\partial p}{\partial x_i} + \mu(\frac{\partial}{\partial x_i}[\frac{\partial \overline{u}_i}{\partial x_j}) + \frac{\partial \overline{u}_j}{\partial x_i}] - \frac{2}{3}\frac{\partial \overline{u}_k}{\partial x_k}) + S_i - \rho\overline{u_i^{'}u_j^{'}} \tag{2.8}$$

Equation 2.8 is known as the time-averaged, or Reynolds Averaged Navier Stokes (RANS) equation. Additional terms, represented here by the last term on the right-hand side of equation 2.8, $\rho\overline{u_i^{'}u_j^{'}}$, now appear in the momentum equation. These terms are known as the Reynolds stresses, which need to be modeled to close the RANS equations.

2.2 Discretisation

Discretisation involves converting the governing equations from a differential form into an algebraic form. Discretisation schemes must possess certain properties in order to yield physically and numerically realistic results. Versteeg and Malalasekera (1995) defined fundamental properties for discretisation, namely conservativeness, boundedness and transportiveness.

To ensure conservativeness of the transported property, ϕ, for the entire solution domain, the flux of ϕ leaving a control volume must be equal to the flux of ϕ entering the adjacent control volume through the same face. Boundedness states that in the absence of sources, the internal values of a property ϕ should be bounded by its boundary values. For transportiveness, the cell Peclet number is defined as

$$Pe = \frac{\rho u \delta x}{\Gamma} \tag{2.9}$$

Where ρ is the fluid density, u is the fluid velocity, δx is the characteristic length and Γ is the diffusion coefficient. The Peclet number is a measure of the relative strengths of convection and diffusion. For high Peclet numbers, i.e., $Pe \rightarrow \infty$, convection dominates and ϕ will be strongly influenced by conditions upstream. For low Peclet numbers, i.e., $Pe \rightarrow 0$, the flow will be strongly diffusive and ϕ will be spread equally in all directions. The directionality of influence is known as transportiveness. Widely used discretisation schemes will be presented below and will be described in terms of accuracy and the degree to which flow directionality, or transportiveness, is taken in to account.

2.2.1 First Order Upwind Differencing Scheme

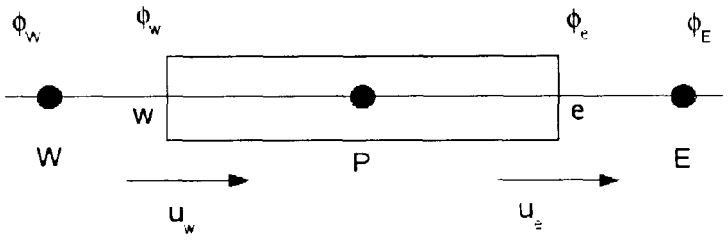

Figure 2.1: First order upwind scheme for flow in the positive direction

For upwind differencing, the face value of ϕ is derived from quantities upstream, or *upwind* to the direction of the normal velocity. The first order upwind differencing

scheme is only first order accurate, but it does take the directionality of the flow into account. For flow in the positive direction, as in figure 2.1, where $u_w > 0, u_e > 0$

$$\phi_w = \phi_W \tag{2.10}$$

and

$$\phi_e = \phi_P \tag{2.11}$$

For flow in the negative direction, as in figure 2.2, where $u_w < 0, u_e < 0$

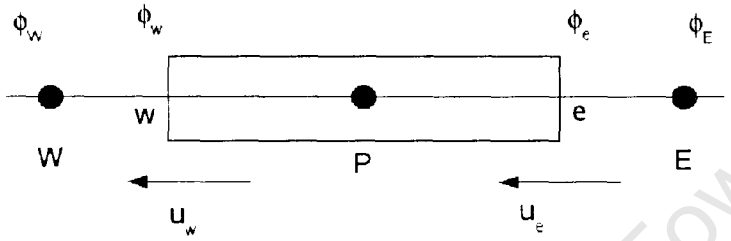

Figure 2.2: First order upwind scheme for flow in the negative direction

$$\phi_w = \phi_P \tag{2.12}$$

and

$$\phi_e = \phi_E \tag{2.13}$$

Versteeg and Malalasekera (1995) stated that a major drawback of the upwind differencing scheme is that is produces erroneous results when the flow is not aligned with the grid. This error is commonly referred to as false diffusion. It has been reported by Han et al. (1981) that grid refinement can reduce false diffusion, however the amount of grid refinement required to compensate for false diffusion is often impractical, as relatively fine grids would be required.

2.2.2 Central Differencing Scheme

The central differencing scheme is a second order accurate discretisation scheme which assumes that the transported variable ϕ varies linearly between two nodal positions. Therefore, with reference to figures 2.1 and 2.2

$$\phi_e = \phi_E(\frac{x_e - x_P}{x_E - x_P}) + \phi_P(1 - \frac{x_e - x_P}{x_E - x_P}) \tag{2.14}$$

For a uniform grid, the degree of influence on a node is equal in all directions. Siwale (2004) found that the central differencing scheme, in conjunction with a high grid

density, accurately predicted experimental power numbers and turbulent kinetic energy values. However, Versteeg and Malalasekera (1995) have stated that for $Pe > 2$, the central differencing scheme may lead to physically impossible solutions. Furthermore, the central differencing scheme does not take flow directionality into account.

2.2.3 Hybrid Discretisation Scheme

The Hybrid discretisation scheme is a combination of the central and upwind differencing schemes. The central differencing scheme is employed for $Pe < 2$ and the upwind scheme for $Pe \geq 2$. It has been stated by Han et al. (1981) that for convection dominated flows, the Hybrid scheme is only marginally superior to the upwind differencing scheme and that using it places restrictions on the density of the grid used. Furthermore, it's accuracy, due to Taylor series truncation, is only first order.

2.2.4 Quadratic Upwind Interpolation Differencing Scheme

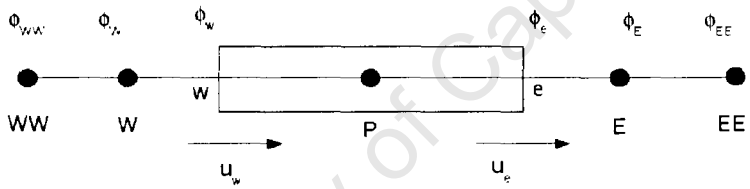

Figure 2.3: Schematic representation of the QUICK scheme

The Quadratic Upwind Interpolation Differencing (QUICK) scheme uses three-point upstream-weighted interpolation for cell face values (Versteeg and Malalasekera, 1995). A parabola is fitted to the nodal values at either side of a face and at a point upstream of a face. For figure 2.3, when $u_w > 0$

$$\phi_w = \frac{3}{4}\phi_W + \frac{3}{8}\phi_P - \frac{1}{8}\phi_{WW} \tag{2.15}$$

For figure 2.3, when $u_e > 0$

$$\phi_e = \frac{3}{4}\phi_P + \frac{3}{8}\phi_E - \frac{1}{8}\phi_W \tag{2.16}$$

Siwale (2004) reported that the QUICK scheme, in conjunction with a high grid density, accurately predicted power numbers and turbulent kinetic energies that were in good agreement with experimental values. Aubin et al. (2004) reported that the QUICK scheme was more accurate in predicting turbulent kinetic energy than the upwind differencing scheme.

2.3 Turbulence Modeling

Turbulence modeling is required to provide accurate information about real, i.e. non-idealized, flows. To resolve turbulence all the way down to the smallest scales (turbulence micro scales), Direct Numerical Simulation (DNS) of the Navier-Stokes equations is required. However, DNS is impractical as a very fine grid resolution and substantial calculation times are required.

Two alternative approaches have been developed to modify the Navier-Stokes equations so that turbulence micro scale fluctuations are taken into account, namely the Reynolds Averaged Navier-Stokes (RANS) equations and Large Eddy Simulations (LES). Both approaches introduce additional terms into the governing equations which need to modeled to achieve closure for the unknown variables. For Large Eddy Simulations, the flow field is explicitly solved at spaces larger than the grid spacing (Derksen and van den Akker, 1999). At smaller scales, isotropic turbulence is assumed and a simple turbulence model is applied. The rationale behind LES is that large eddies are dictated by geometry and flow boundaries and that momentum, mass, energy and other passive scalars are transported mostly by these eddies. LES has been used by researchers such as Eggels (1996), Derksen and van den Akker (1999) and Hartmann et al. (2004). These authors reported accurate predictions of experimental data. By resolving only the large eddies, a much coarser mesh and larger time-steps sizes than those used for DNS can be used. One advantage LES has over RANS models is that it uses only one semi-empirical parameter in its formulation, while RANS models typically use 5 to 10 parameters (Derksen and van den Akker, 1999). Furthermore, through explicitly resolving large scale turbulence, LES models less turbulence than RANS models and is therefore seen to be more accurate than RANS modeling. For this same reason, however, LES is more computationally intensive than RANS turbulence models. The RANS equations model all the turbulence scales and therefore requires less computational effort than DNS or LES.

Launder and Spalding (1974) stated that a good turbulence model should have extensive universatility and should not be too complex to use. Universatility, as implied by the authors, meant that a single set of empirical constants or functions, inserted into the relevant equations, should provide close simulation of a wide range of flows. The k-ϵ turbulence model meets these requirements. It will be described in section 2.3.1 and other RANS models will be briefly discussed.

2.3.1 The k-ϵ Turbulence Model

The standard k-ϵ turbulence model is a two-equation, semi-empirical, isotropic model based on the Boussinesq hypothesis. It relates the Reynolds stresses to the mean velocity gradients by means of the following equation

$$-\rho\overline{u_i'u_j'} = \mu_t(\frac{\partial u_i}{\partial x_j} + \frac{\partial u_j}{\partial x_i}) - \frac{2}{3}(\rho k + \mu_t\frac{\partial u_i}{\partial x_i})\delta_{ij} \tag{2.17}$$

In equation 2.17, k is a function of the fluctuating velocities and is given by

$$k = \frac{1}{2}(\overline{u_i'u_i'} + \overline{v_i'v_i'} + \overline{w_i'w_i'}) \tag{2.18}$$

The k-ϵ model solves two additional transport equations for k and ϵ, where these transport equations are given by

$$\frac{\partial}{\partial t}(\rho k) + \frac{\partial}{\partial x_i}(\rho k u_i) = \frac{\partial}{\partial x_j}[(\mu + \frac{\mu_t}{\sigma_k})\frac{\partial k}{\partial x_j}] + G_k - \rho\epsilon \tag{2.19}$$

and

$$\frac{\partial}{\partial t}(\rho\epsilon) + \frac{\partial}{\partial x_i}(\rho\epsilon u_i) = \frac{\partial}{\partial x_j}[(\mu + \frac{\mu_t}{\sigma_k})\frac{\partial \epsilon}{\partial x_j}] + C_{1\epsilon}\frac{\epsilon}{k}G_k + C_{2\epsilon}\rho\frac{\epsilon^2}{k} \tag{2.20}$$

$C_{1\epsilon}$ and $C_{2\epsilon}$ are model constants and σ_k and σ_ϵ are the turbulent Prandtl numbers for k and ϵ. In equations 2.19 and 2.20, G_k represents the generation of turbulent kinetic energy due to the mean velocity gradients (FLUENT, 2005) and is given by

$$G_k = \mu_t(\frac{\partial u_i}{x_j} + \frac{\partial u_j}{x_i})\frac{\partial u_j}{x_i} \tag{2.21}$$

The turbulent viscosity is a function of k and ϵ and is given by

$$\mu_t = \rho C_\mu\frac{k^2}{\epsilon} \tag{2.22}$$

where C_μ is a model constant. The model constants for the k-ϵ model are given in table 2.1. Launder and Spalding (1974) tested the applicability of the standard k-ϵ model to

Table 2.1: Model Constants for the k-ϵ turbulence model (Launder and Spalding, 1974)

C_μ	$C_{1\epsilon}$	$C_{2\epsilon}$	σ_k	σ_ϵ
0.09	1.44	1.92	1.00	1.30

nine different types of flow. The authors reported good agreement between numerical

and experimental results. However, both Launder and Spalding (1974) and Abujelala and Lilley (1984) reported that the standard k-ϵ model inaccurately predicted swirling flows. Two variants of the k-ϵ model, namely the Renormalization group (RNG) and Realizable k-ϵ models, have been developed in an effort to overcome the shortcomings of the standard k-ϵ model. The RNG k-ϵ model takes swirl into account and uses an analytical formula to calculate the turbulent Prandtl numbers (σ_k and σ_ϵ). The RNG model has also been formulated to suite low Reynolds number flows. The Realizable k-ϵ model is consistent with the physics of turbulent flow in that it satisfies certain mathematical constraints on the Reynolds Stresses. However, one major limitation of the Realizable model is that it produces non-physical turbulent viscosities for flows involving stationary and rotating reference frames (FLUENT, 2005), e.g. Multiple Reference Frames.

Most researchers have used the standard k-ϵ model to model turbulence in stirred tanks (Ranade et al., 1989; Kresta and Wood, 1991; Ranade and van den H.E.A. Akker, 1994; Morud and Hjertager, 1996; Brucato et al., 1998; Ng et al., 1998; Montante et al., 2001; Campolo et al., 2003). Other researchers have employed the variants of the k-ϵ turbulence model. Aubin et al. (2004) employed the standard and RNG k-ϵ models and found that the results from the two models did not differ significantly. Siwale (2004) also employed the standard and RNG k-ϵ models and found the standard k-ϵ model to more accurately predict turbulence kinetic energy and mean velocity profiles.

Hartmann et al. (2004) used both the k-ω turbulence model and LES to model a Rushton turbine-agitated stirred tank with T=0.15m. The authors generally found good agreement for velocity profiles with the exception of the tangential velocity at the impeller tip, which was over-predicted. Moreover, the authors found that both turbulence models failed to accurately predict turbulent kinetic energy. Aubin et al. (2004) modeled a six blade, 45° pitched blade turbine-agitated tank with T=0.19 m using the standard and RNG k-ϵ turbulence models. Poor correlation between experimental and numerical values of turbulent kinetic energy was reported. Montante et al. (2001) modeled a Rushton turbine-agitated stirred tank with T=0.290 m using the standard k-ϵ model. While the authors reported good agreement between experimental and numerical velocity profiles, they too found that their numerical model poorly predicted turbulent kinetic energy. The three previously mentioned groups attributed the discrepancy between experimental and numerical results to the shortcomings of the turbulence

model.

Siwale (2004) modeled a tank with T=0.15 m, using the k-ϵ model and found good agreement between experimental and numerical data sets for both velocity and turbulent kinetic energy profiles. Wechsler et al. (1999) modeled a tank with T = 0.152 m, using the standard k-ϵ model and found good agreement for mean velocities and reasonable agreement for turbulent kinetic energy.

2.3.2 The k-ω Turbulence Model

The k-ω model is a two equation, isotropic turbulence model which also makes use of the Boussinesq hypothesis (see equation 2.17) to relate the Reynolds stresses to the mean velocity gradients and is numerically similar to the k-ϵ model. In addition to solving an equation for the turbulent kinetic energy, k, the model also solves a transport equation for the specific dissipation, ω, which is the inverse of the time scale associated with turbulence.

2.3.3 The Reynolds Stress Model

The Reynolds Stress model (RSM) closes the RANS equations by calculating the Reynolds stresses and solving transport equations for each of them. With the introduction of the Reynolds stresses, six additional transport equations need to be solved for three dimensional flows and four for two dimensional flows. For most flows, turbulence models based on the Boussinesq hypothesis, such as the k-ϵ model, perform well (FLUENT, 2005). However, the Reynolds stress model is better suited for highly anisotropic flows.

2.4 Grid Resolution

The grid densities used by various researchers are given in table 2.2 (Note that the grid densities given refer to the maximum control volumes used by the respective researchers). The domain refers to the portion of the stirred tank modeled, e.g., a 180 ° domain refers to half of the stirred tank.

Due to computational restrictions in the past, researchers were limited by the amount of control volumes that could be used. Bakker (1992) used grid densities of 21 500, 23 900 and 25 000 and reported good agreement with experimental data for mean velocity

Table 2.2: Grid densities used by various researchers

Reference	T (m)	Domain	Number of Cells
Kresta and Wood (1991)	0.456	45 °	23 400
Bakker (1992)	0.444	90 °	25 000
Luo et al. (1993)	0.147	180 °	151 200
Fokema et al. (1994)	0.15	90 °	17 200
Ranade and van den Akker (1994)	0.3	180 °	13 500
Harvey et al. (1995)	0.145	90 °	619 750
Tabor et al. (1996)	0.27	180 °	120 000
Ranade (1997)	0.3	180 °	61 100
Ng et al. (1998)	0.1	180 °	240 000
Ranade and Deshpande (1999)	0.3	180 °	176 400
Jenne and Reuss (1999)	0.444	90 °	194 500
Wechsler et al. (1999)	0.152	90 °	1 003 500
Bartels et al. (2002)	0.152	180 °	2 082 800
Deen et al. (2002)	0.222	180 °	370 900
Lane et al. (2002)	1.0	60 °	44 000
Campolo et al. (2003)	0.294	360 °	450 000
Aubin et al. (2004)	0.19	360 °	155 000
Hartmann et al. (2004)	0.15	360 °	228 000
Siwale (2004)	0.15	180 °	1 900 000
Khopkar et al. (2005)	0.2	180 °	352 700
Kerdouss et al. (2006)	0.292	180 °	280 000

profiles. However, the author stated that the turbulent RMS velocity was under predicted in the outflow if the impeller. Harvey et al. (1995) used grid densities of 89 000, 223 000 and 619 750 control volumes and reported good agreement with experimental data for radial and axial velocities. However, the authors reported an over prediction of the tangential velocities and no turbulence data was reported. Tabor et al. (1996) used grid densities of 50 000 and 120 000 control volumes. The authors reported good agreement for mean velocity profiles but made no mention of turbulence parameters. Grid resolution greatly influences the accuracy of a CFD solution. In order to get a realistic, grid independent solution, simulations would need to be carried out on succes-

sively fine grids until no noticeable difference in solution is observed. Grid dependence studies were carried out by Ng et al. (1998) with grid densities of 46 000, 103 000, 140 000 and 240 000 control volumes, Wechsler et al. (1999) with grid densities of 15 700, 125 400 and 1 003 500 control volumes and by Siwale (2004) with grid densities of 33 000, 230 000, 800 000 and 1 900 000. Ng et al. (1998) found that all but the coarsest grid produced similar results. The authors found turbulent kinetic energy was under predicted by 50 percent in certain regions. The error was attributed to factors such as the turbulence model used, the time step size, wall region treatment and grid resolution. The authors went on to say that further grid refinements were unlikely to improve the prediction of turbulent kinetic energy. However, the studies of Wechsler et al. (1999) and Siwale (2004) showed that very fine grids (in excess of 1 000 000 control volumes) were required to attain grid independence for turbulent kinetic energy. Some researchers (Montante et al., 2001; Hartmann et al., 2004; Aubin et al., 2004) have attributed poor numerical results to RANS turbulence models, specifically the k-ϵ model. However, the results reported by Siwale (2004) and Wechsler et al. (1999) suggest that the poor results reported by Hartmann et al. (2004), Aubin et al. (2004) and Montante et al. (2001) might be due to numerical errors rather than the deficiencies of the k-ϵ model.

2.5 Impeller Models

A major problem in modeling stirred tanks is the relative motion between the stationary baffles and rotating impeller. Various steady and unsteady approaches have been proposed to accommodate for this. The most common impeller models will be described in sections 2.5.1 to 2.5.4.

2.5.1 Multiple Reference Frames Model

When the clearance between the impeller and baffles is of the order of or greater than the impeller diameter, the flow pattern in the region of the impeller is unaffected by the flow in the rest of the tank (Tabor et al., 1996; Aubin et al., 2004). Therefore, the problem can be assumed to be time-independent with respect to the impeller.

A frame of reference, rotating in the fluid zone containing the impeller, is used to calculate flow variables. The impeller is therefore stationary in the MRF formulation.

The velocity vectors for the stationary and rotating reference frames are related by the following expression

$$U_i = u_i + \varepsilon_{ijk}\omega_j x_k \tag{2.23}$$

Where U_i and u_i are the velocity vectors for the stationary and rotating reference frames, ε_{ijk} is the permutation operator, ω_j is the angular velocity and x_k is the position relative to the axis of rotation.

The MRF model is appropriate for tank geometries where there is sufficient spacing between the impeller blades and baffles (Tabor et al., 1996) and where the interactions between the two are relatively weak (FLUENT, 2005).

2.5.2 Sliding Mesh Model

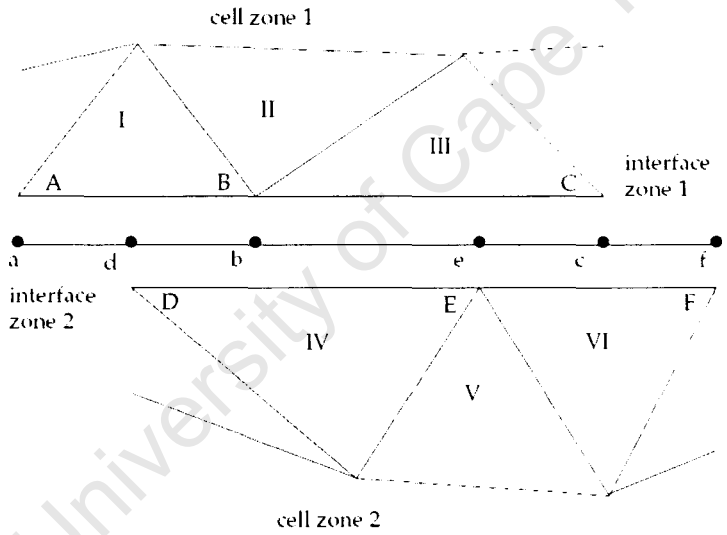

Figure 2.4: Schematic representation of the sliding intersection (FLUENT, 2005)

The Sliding Mesh (SM) model is a fully transient method which allows the computation to take place simultaneously across the whole flow field and enhances numerical stability and accuracy (Tabor et al., 1996). Two or more cell zones are used where one or more cell zones move, by either rotating or translating, relative to other cell zones. Interface zones, shown in figure 2.4, are defined for each distinct face zone at the sliding boundary. Each zone moves relative to each other at this interface at discrete time-steps. The intersection across the the interface zones is determined at each new time step to compute the interface flux. With respect to figure 2.4, the interface zones

are made up of faces A-B, B-C, D-E and E-F. The intersection of the interfaces are represented by faces a-d, d-b, b-e, e-c and c-f. Faces produced where the two cell zones overlap (faces a-d, d-b, b-e, e-c and c-f) are grouped to form an interior zone. The flux across interface cell IV will be calculated using faces d-b and b-e, instead of face D-E, for example. Therefore, as the grids move relative to each other, node alignment along the grid interface is not required (FLUENT, 2005). The number of faces at the intersection varies as the zones move relative to one another.

Luo et al. (1993) modeled half a stirred tank from rest and found that the flow pattern reached a steady state after 6 impeller rotations, at which point data was sampled. Tabor et al. (1996) also modeled half a stirred tank using the MRF model to generate the flow field and subsequently ran the sliding mesh model for 10 complete impeller rotations before sampling data. However, Wechsler et al. (1999) stated that when starting the sliding mesh from rest, 10 to 30 impeller rotations are required to overcome the start up flow patterns. Deen et al. (2002) modeled half a stirred tank and ran the sliding mesh model for 20 impeller rotations, using the flow field from another simulation for the starting conditions. The solution from an MRF simulation can therefore be used as an initial condition for sliding mesh simulations. The sliding mesh resolves the full flow field and is time-dependent, therefore it is more computationally expensive than the MRF model.

2.5.3 Computational Snapshot Model

For the Computational Snapshot approach, the impeller is considered fixed in position. The flow field generated by an impeller is mainly governed by pressure and centrifugal forces generated by the impeller rotation and the corresponding rotating flows (Deshpande and Ranade, 2003). The rotation of the impeller blades cause suction at the back and equivalent ejection at the front of the blades. Ranade (1997) modeled the suction and ejection on the impeller blades by specifying mass sources and sinks at the computational cells at the front and back sides of the blades respectively. This approach was also used by Ranade and van den Akker (1994), Ranade and Deshpande (1999), Ranade et al. (2001), Deshpande and Ranade (2003) and Khopkar et al. (2005). However, Luo et al. (1993) have stated that the representation of the impeller action by momentum sources contains many uncertainties about the magnitude and distribution of the body forces acting on the impeller.

2.5.4 Impeller Boundary Conditions Model

The Impeller Boundary Conditions (IBC) model is a steady-state model where the rotation of the impeller is modeled by applying experimentally derived boundary conditions to the outflow of the impeller. The IBC model was used successfully by Ranade and Joshi (1989), Kresta and Wood (1991), Fokema et al. (1994), Brucato et al. (1998) and Jenne and Reuss (1999). The biggest limitation of the IBC model is its reliance on experimental data. Furthermore, because the impeller geometry is not explicitly modeled, flow features such as the trailing vortex pair described by van't Riet and Smith (1973; 1975) and Yianneskis et al. (1987) are not captured.

2.6 Multiphase Models

Generally, two approaches are available for modeling multiphase flows, namely the Euler-Euler approach and the Euler-Lagrange approach. The Euler-Euler approach treats different phases as interpenetrating continua while the Euler-Lagrange approach treats the fluid phase as a continuum and the dispersed phase is solved by tracking the secondary phase through the flow field. Euler-Lagrange models assume that the secondary phase occupies a small volume fraction (FLUENT, 2005). Therefore, these models are inappropriate for applications where the second phase is not negligible.

As the volume of one phase cannot be occupied by that of another, phase volume fractions are introduced. Volume fractions represent the space occupied by each phase. The volume of phase q, V_q, is defined by

$$V_q = \int_V \alpha_q dV \tag{2.24}$$

where

$$\sum_{q=1}^{n} \alpha_q = 1 \tag{2.25}$$

The effective density of phase q is

$$\widehat{\rho}_q = \alpha_q \rho_q \tag{2.26}$$

Continuity and momentum equations are satisfied for each phase individually. These equations are closed through constitutive relations by means of empirical information. Various Euler-Euler models will be described in sections 2.6.1 to 2.6.3.

2.6.1 The Eulerian Model

The Eulerian model solves a set of momentum and continuity equations for each phase. The phases are coupled by means of pressure and interphase coefficients. The continuity equation for phase q is given by

$$\frac{\partial}{\partial t}(\alpha_q \rho_q) + \frac{\partial}{\partial x_q}(\alpha_q \rho_q \vec{v_q}) = \sum_{p=1}^{n}(\dot{m}_{pq} - \dot{m}_{qp}) + S_q \tag{2.27}$$

where $\dot{m}_{pq}$ is the mass transfer from phase p to phase q, $\dot{m}_{qp}$ is the mass transfer from phase q to phase p and S_q is a source term. $\vec{v_q}$ is the velocity of phase q. The momentum equation is given by

$$\frac{\partial}{\partial t}(\alpha_q \rho_q \vec{v}_q) + \nabla \cdot (\alpha_q \rho_q \vec{v}_q \vec{v}_q) = -\alpha_q \nabla p + \nabla \cdot \bar{\bar{\tau}}_q + \alpha_q \rho_q \vec{g} + \sum_{p=1}^{n}(\vec{R}_{pq} + \dot{m}_{pq}\vec{v}_{pq} - \dot{m}_{qp}\vec{v}_{qp}) + \vec{F} \tag{2.28}$$

Where

$$\vec{F} = (\vec{F}_q + \vec{F}_{lift,q} + \vec{F}_{vm,q}) \tag{2.29}$$

and $\bar{\bar{\tau}}_q$ is the q^{th} phase strain tensor given by

$$\bar{\bar{\tau}}_q = \alpha_q \mu_q (\nabla \vec{v}_q + \nabla \vec{v}_q^T) + \alpha_q (\lambda - \frac{2}{3}\mu_q) \nabla \cdot \vec{v}_q \bar{\bar{I}} \tag{2.30}$$

Where μ_q and λ_q are the shear and bulk viscosities for phase q, F_q is an external body force, $F_{lift,q}$ is a lift force and $F_{vm,q}$ is a virtual mass force. $\vec{R}_{pq}$ is an interaction term between the phases and p is the pressure, common for all phases. The interaction term is given by

$$\sum_{p=1}^{n} \vec{R}_{pq} = \sum_{p=1}^{n} K_{pq}(\vec{v}_p - \vec{v}_q) \tag{2.31}$$

Where K_{pq} is the interphase momentum exchange coefficient. For fluid-fluid flows, each secondary phase is assumed to form droplets or bubbles (FLUENT, 2005). The exchange for these types of flows is given generally as

$$K_{pq} = \frac{\alpha_q \alpha_p \rho_p f}{\tau_p} \tag{2.32}$$

Where f is the drag function and τ_p is the particulate relaxation time, defined as

$$\tau_p = \frac{\rho_p d_p^2}{18 \mu_q} \tag{2.33}$$

Here, d_p is the bubble diameter of phase p. For the calculation of the drag function, f, the Schiller and Naumman (1933) model is given by

$$f = \frac{C_D Re}{24} \tag{2.34}$$

Where

$$C_D = \begin{cases} \frac{24(1+0.15Re^{0.687})}{Re} & Re \leq 1000 \\ 0.44 & Re > 1000 \end{cases} \tag{2.35}$$

Re is the relative Reynolds number, which for the primary and secondary phases, p and q, is obtained from

$$Re = \frac{\rho_q |\vec{v}_p - \vec{v}_q| d_p}{\mu_q} \tag{2.36}$$

The relative Reynolds number for secondary phases p and r is given by

$$Re = \frac{\rho_{rp} |\vec{v}_r - \vec{v}_p| d_{rp}}{\mu_r p} \tag{2.37}$$

Where $\mu_r p = \alpha_p \mu_p + \alpha_r \mu_r$ is the mixture viscosity for phases p and r.

The dispersed k-ϵ model is an appropriate turbulence model when concentrations of the secondary phase are dilute (FLUENT, 2005). For this case, interparticulate collisions are negligible and the primary phase dominates the the random motion of the secondary phases. The turbulent viscosity, $\mu_{t,q}$, is defined in terms of the turbulent kinetic energy of phase q as

$$\mu_{t,q} = \rho_q C_\mu \frac{k_q^2}{\epsilon_q} \tag{2.38}$$

The transport equations for k and ϵ are given by

$$\frac{\partial}{\partial t}(\alpha_q \rho_q k_q) + \frac{\partial}{\partial x_i}(\alpha_q \rho_q \vec{U}_q k_q) = \nabla \cdot (\alpha_q \frac{\mu_{t,q}}{\sigma_k} \nabla k_q) + \alpha_q G_{k,q} - \alpha_q \rho_q \epsilon_q + \alpha_q \rho_q \Pi_{k_q} \tag{2.39}$$

and

$$\frac{\partial}{\partial t}(\alpha_q \rho_q \epsilon_q) + \frac{\partial}{\partial x_i}(\alpha_q \rho_q \vec{U}_q \epsilon_q) = \nabla \cdot (\alpha_q \frac{\mu_{t,q}}{\sigma_k} \nabla \epsilon_q) + \alpha_q \frac{\epsilon_q}{k_q}(C_{1\epsilon} G_{k,q} - C_{2\epsilon} \rho_q \epsilon_q) + \alpha_q \rho_q \Pi_{\epsilon_q} \tag{2.40}$$

Where Π_{k_q} and Π_{ϵ_q} represent the influence of the dispersed phases on the continuous phase q. Π_{k_q} is given by

$$\Pi_{k_q} = \sum_{p=1}^{M} \frac{K_{pq}}{\alpha_q \rho_q} (< \vec{v}_q'' \cdot \vec{v}_p'' > + (\vec{U}_p - \vec{U}_q) \cdot \vec{v}_{dr}) \tag{2.41}$$

which can be simplified to

$$\Pi_{k_q} = \sum_{p=1}^{M} \frac{K_{pq}}{\alpha_q \rho_q} (k_{pq} - 2k_q + \overrightarrow{v}_q \cdot \overrightarrow{v}_{dr}) \tag{2.42}$$

Where k_{pq} is the covariance of the velocities of the continuous phase q and the dispersed phase p. Π_{ϵ_q} is given by

$$\Pi_{\epsilon_q} = C_{3\epsilon} \frac{\epsilon_q}{k_q} \Pi_{k_q} \tag{2.43}$$

$G_{k,q}$ is the production of turbulent kinetic energy, given by equation 2.21. All other terms are as described for the single phase k-ϵ model.

2.6.2 The Volume of Fluid Model

The Volume of Fluid (VOF) model relies on the fact that two or more phases are not interpenetrating. For each phase added to a model, a volume fraction of the added phase is introduced in the computational cell. The volume fraction of all the phases sum to unity in each control volume.

2.6.3 The Mixture Model

The mixture model is similar to the VOF model in that only one fluid is modeled. It differs from the VOF model by allowing phases to be interpenetrating and to have different velocities. The mixture model solves continuity, momentum and energy equations for the mixture and also solves the volume fraction equation for the secondary phase and algebraic expressions for the relative velocities.

2.7 Review of Multiphase Studies using CFD

A review of CFD studies of multiphase flows in stirred tanks will be presented below. Literature will be reviewed in terms of impeller models and turbulence models employed as well as reported results such as mean velocities, gas hold up and turbulence parameters where possible.

Bakker (1992) modeled a 90 ° section of a 0.444 m diameter stirred tank using a single phase flow pattern as the input for the gas-liquid model. An in-house code was used to determine the gas hold up, bubble size, mass transfer, bubble break-up and coalescence.

The standard k-ϵ and algebraic stress turbulence models were used to model turbulence and experimental profiles were applied in the outflow of the impeller to model the rotation of the impeller. The author generally reported good agreement between experimental and numerical results.

Gosman et al. (1992) carried out simulations for gas-liquid and solid-liquid flows using a 90 ° model of stirred tank (with $T = 1.83$ m and $T = 0.294$ m respectively) for the calculation domain. The Eulerian mixture model was employed and the standard k-ϵ model was used to model turbulence. Experimentally derived boundary conditions were applied to the volume swept by the impeller blades to simulate the rotation of the impeller. For solid-liquid flows, mean velocities were generally well predicted. However, the RMS velocities were under predicted above and below the impeller. The authors also reported an under prediction of gas hold up near the free surface of the tank and in the upper region (upper vortex) of the tank, above the impeller. Under predictions of gas hold up were also reported in the impeller stream and in the lower region (lower vortex) of the tank. The authors attributed the discrepancy to inadequate grid resolution and the assumptions of spherical bubbles and constant bubble radii.

Ranade and van den Akker (1994) modeled a 180 ° section of a stirred tank using a the computational snapshot approach to simulate the impeller rotation and the standard k-ϵ model to model turbulence in conjunction with the Eulerian multiphase model. Good agreement between experimental and numerical profiles for axial and tangential velocity were reported. However, turbulent kinetic energy was found to be poorly predicted in certain regions of the tank.

Morud and Hjertager (1996) simulated a two dimensional model of a stirred tank with T=0.222 m. The standard k-ϵ model was used to model turbulence and the impeller and baffles were treated as source and sink terms respectively. The Eulerian mixture model was used. The authors reported good predictions of tangential velocities and radial velocities. However, axial velocities were over predicted. Good predictions of gas volume fraction were reported.

Ranade and Deshpande (1999) modeled a 180 ° section of a stirred tank with $T = 0.3$ m using the standard k-ϵ model to model turbulence and the computational snapshot approach to simulate the impeller rotation. The authors stated that the grids used

were too coarse to capture the trailing vortices behind the impeller blades. However, the authors went on to say that the computational snapshot approach was adequate for simulating flow properties in the bulk tank.

Deen et al. (2002) used the Eulerian mixture model to simulate gas-liquid flow in a stirred tank with T = 0.222 m, using a 180 ° numerical model as the calculation domain. The sliding mesh model was used to simulate the rotation of the impeller and the standard k-ϵ model was used to model turbulence. The authors reported a 30 percent reduction in mean velocities in the impeller swept region for the aerated tank when compared to the unaerated tank. Good agreement between experimental and numerical radial velocity profiles was reported. However, the authors reported an over prediction of axial velocity profiles.

Lane et al. (2002) used the Eulerian model to simulate gas-liquid flow in a 60 ° numerical model of a 1 m diameter stirred tank. The authors used the standard k-ϵ model in conjunction with the MRF model to model turbulence and the impeller rotation respectively. Bubble size variations resulting from bubble break-up and coalescence were also modeled. Although the flow pattern predicted the experimental flow pattern, the gas hold up was under predicted. The authors stated that the difference was most likely due to the specification of the bubble drag coefficient. No mean velocity or turbulence data was presented.

Khopkar et al. (2005) simulated gas-liquid flow using a 180 ° numerical model as the calculation domain for a stirred tank with $T = 0.2$ m. The Eulerian multiphase model was used to model the mixture, the standard k-ϵ model was used to model turbulence and the computational snapshot approach was used to model the impeller rotation. The authors reported good overall prediction of mean velocities, however the radial and tangential velocities were over predicted in the impeller discharge stream. The authors produced only a qualitative comparison of gas hold up, comparing gas distributions in the region of the impeller. The CFD predictions were found to inaccurately predict the gas hold up. The authors stated that the experimental results were very sensitive with respect to the way in which data was processed, which could have resulted in the discrepancy between the two sets of results.

Gentric et al. (2005) modeled two stirred tanks, one being a scaled up version of the

other using a calculation domain of 180 ° for each model. The Eulerian multiphase model was used. The MRF model was used to simulate the rotation of the impeller and the standard k-ϵ model was used to model turbulence. Single phase flow fields were compared with two-phase flows by means of contour plots. The authors reported that the numerical gas hold up was in accordance with the experimental gas hold up. No mean velocity or turbulence data was presented.

Kerdouss et al. (2006) simulated gas-liquid flow in a 180 ° section of a 0.292 m diameter stirred tank agitated by two Rushton turbines. The MRF model was used to account for the impeller rotation, the dispersed k-ϵ model was used to model turbulence and bubble break-up and coalescence were modeled. The authors reported good quantitative agreement with experimental data for gas holdup and bubble size distributions. No mean velocity or turbulence data was presented.

Sun et al. (2006) modeled a surface-aerated stirred tank with $T = 0.38$ m using the standard k-ϵ model to model turbulence and the Inner-Outer (I-O) model to model the impeller rotation. The I-O model is a variation of the MRF model, where the major difference is that the two cell zones partially overlap. A 180 ° numerical model was used as the calculation domain. The authors reported satisfactory agreement for gas hold up close to the liquid surface but stated that the gas hold up in the bulk region was substantially under predicted.

2.8 Discussion

From the studies presented in the literature, the combination of the k-ϵ turbulence model and Eulerian mixture model is appropriate for simulating the flow field in an aerated stirred tank. However, the choice of impeller model is not as uniform among researchers.

The MRF and sliding mesh models are the most accurate impeller models in that no experimental data is required and there is no uncertainty, as stated by Luo et al. (1993), about body forces acting on the impeller.

Therefore, based on suggestions in the literature, the Eulerian mixture model will be used in conjunction with the k-ϵ turbulence model. The MRF and sliding mesh models will be used to model the impeller rotation and results of the two model compared.

These models will be described in detail in Chapter 3.

Chapter 3

CFD Methodology

3.1 Geometry

The numerical model was modeled as a flat-bottomed, bottom aerated tank and was identical to the experimental tank used by Deglon (1998). The tank consisted of four equally spaced baffles and was agitated by a Rushton turbine-impeller. A 180 ° model was used as the calculation domain for the single phase model, while 180 ° and 360 ° models were used as the calculation domain for the multiphase model. The ratios of impeller dimensions are consistent with those of Rushton et al. (1950). The tank has a diameter of $T = 0.14$ m. Other dimensions for the tank are given in table 3.1.

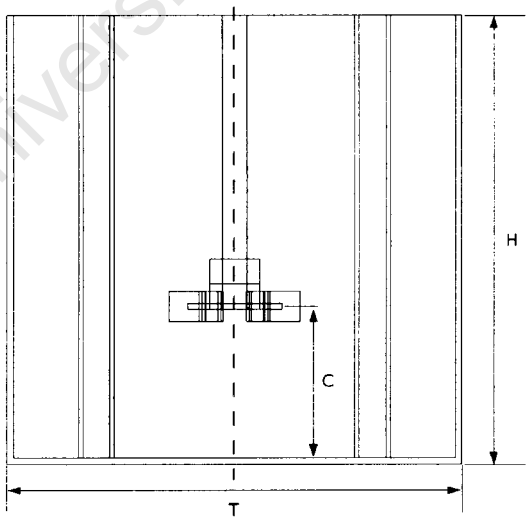

Figure 3.1: Stirred tank dimensions

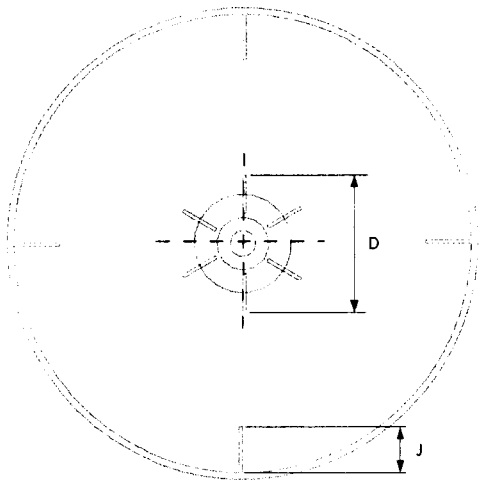

Figure 3.2: Impeller diameter and baffle dimensions

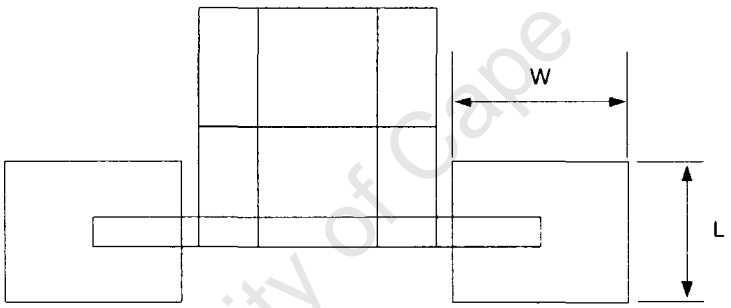

Figure 3.3: Impeller dimensions

Table 3.1: Stirred tank dimensions used in this study

H	H/T	C/T	J/T	D	W:L:D
0.14	1	1/3	1/10	0.047	4:5:20

3.2 Single Phase Model

The single phase model will form the basis for the multiphase model. It will provide an overall picture of the flow field, in terms of mean velocity and turbulence, which can be used to determine trends between the experimental and numerical data.

3.2.1 Grid Resolution

A grid of approximately 758 000 control volumes was used. Care was taken to refine the grid in regions where large gradients were expected, e.g. near the impeller blades and baffles. The control volume distribution is shown in table 3.2 for the regions illustrated in figures 3.4 and 3.5.

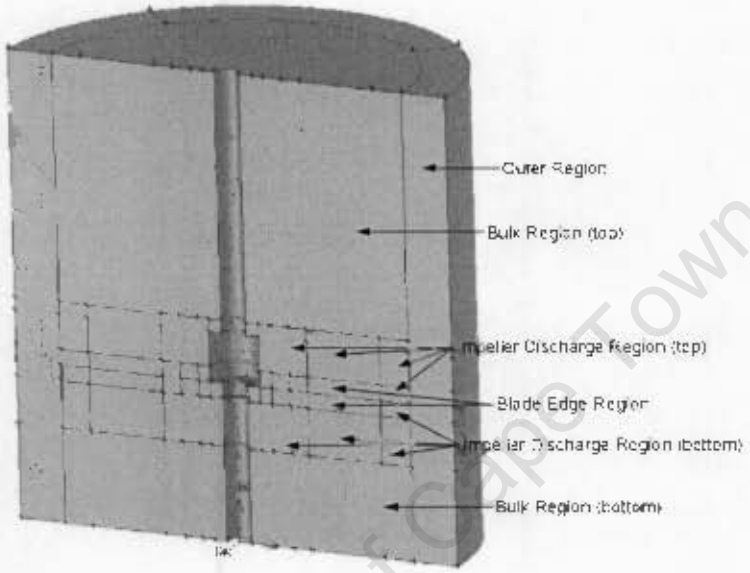

Figure 3.4: Cell zones in the stirred tank

Table 3.2: Control volume distribution for this study

Blade Region	46 656
Hub region	38 880
Blade Edge Region	31 104
Impeller Discharge Region (top)	85 536
Impeller Discharge Region (bottom)	93 312
Bulk Region (top)	174 960
Bulk Region (bottom)	155 520
Outer Region	132 192
total	758 160

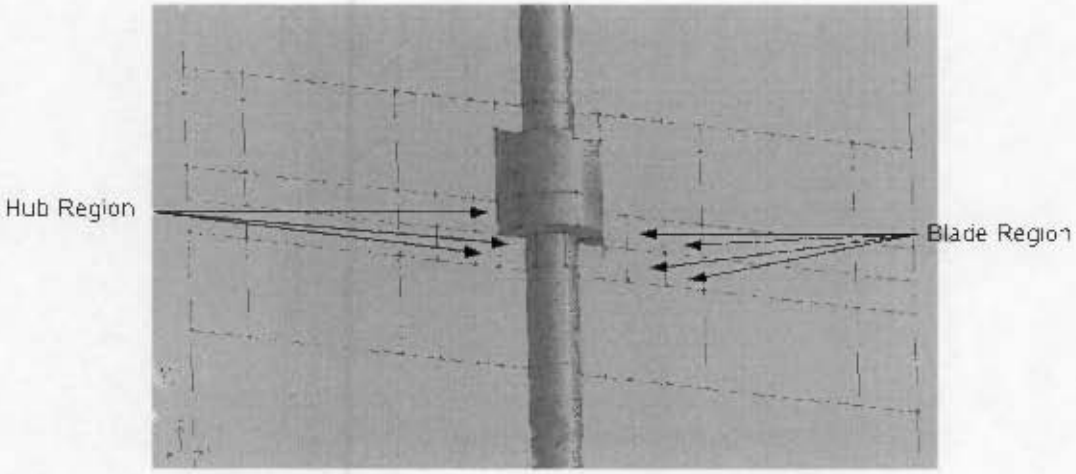

Figure 3.5: Cell zones in the region of the impeller

3.2.2 Discretisation Schemes

Initially, the first order upwind differencing scheme was used to discretise momentum and turbulence parameters. Momentum was then discretised again using the QUICK scheme, where the solutions from the upwind differencing simulations were used as the starting conditions. The SIMPLE algorithm was used to couple pressure and velocity.

3.2.3 Fluid Zones

Two fluid zones were defined, one encompassing the impeller and another encompassing the rest of the tank volume. The region encompassing the impeller extended 1.5 blade heights above and below and half the impeller diameter (D/2) away from the impeller blades, which is consistent with the work of Siwale (2004).

3.2.4 Boundary Conditions

Periodic Boundaries

The flow field in a stirred tank is symmetrical, therefore only half of the tank was used as the calculation domain. Periodic boundary conditions were applied to the periodic planes shown in figure 3.6. This meant that the flow exiting one face was identical to the flow entering the face periodically linked to it. This is consistent with the methods

of Tabor et al. (1996), Siwale (2004), Deglon and Meyer (2006) and Kerdouss et al. (2006).

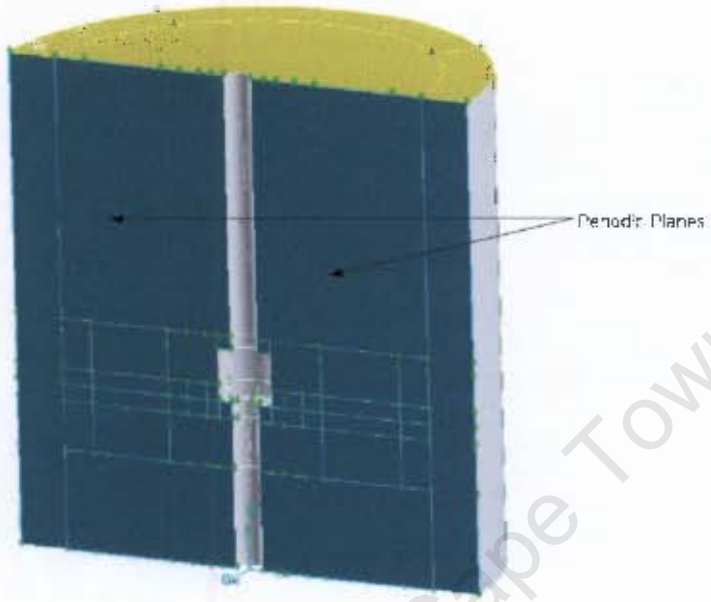

Figure 3.6: Periodic planes for the stirred tank

Boundary Layer and Wall Boundaries

Standard wall functions proposed by Launder and Spalding (1974) were used to resolve the boundary layer in the near-wall region. Wall functions are semi-empirical formulas used to bridge the viscous region of the boundary layer to the fully turbulent flow away from the wall (FLUENT, 2005).

The walls were modeled as infinitely thin faces. No-slip boundary conditions were applied to all the walls, ensuring that the fluid immediately adjacent to the walls moved at the same speed as the walls. With the exception to the sections of the impeller shaft in the stationary frame of reference, all walls were modeled as stationary walls. The sections of the impeller shaft in the stationary reference frame were set as rotating walls and the rotational speed of the impeller were specified for these walls. The impeller shaft was extended to the bottom of the tank to keep the grid as uniform as possible. This is consistent with the work of Deen et al. (2002).

3.3 Multiphase Model

The multiphase model geometry was identical to that of the single phase model. The MRF model as well as the sliding mesh models were used to model the impeller rotation. Wall and periodic boundary conditions were common to both the single phase and multiphase models. Furthermore, only half of the stirred tank was modeled for the MRF model for the reasons outlined in section 3.2.4. This model will be referred to as the 180 ° model from now on. The full geometry will be modeled using the sliding mesh model. This model will be referred to as the 360 ° model. The multiphase model is described in detail in this section.

3.3.1 Discretisation Schemes

First order upwind differencing was used to discretise momentum, volume fraction and turbulence parameters for the MRF model. The QUICK scheme was used to discretise momentum and volume fraction for the sliding mesh model. First order upwind differencing was used to discretise turbulence parameters for the sliding mesh model as the extra computational expense required for higher order discretisation on turbulence models was not justified. The phase-coupled SIMPLE algorithm was used to couple pressure and velocity for both impeller models.

3.3.2 Fluid Zones

Three fluid zones were defined, one zone encompassing the impeller region and another the rest of the stirred tank. The third fluid zone was defined as a volume of air above the tank, to facilitate the natural degassing of air. Adding a gas zone at the liquid surface has also been reported to diminish instabilities (Kerdouss et al., 2006). The height of the volume of air above the tank was equivalent to the height of the tank (H). The region encompassing the impeller extended 1.5 blade heights above and below and half the impeller diameter (D/2) away from the impeller blades, which is consistent with the single phase model as well as the work of Siwale (2004).

3.3.3 Boundary Conditions

Wall boundaries were specified as they were for the single phase model. Furthermore, the tank wall was extended upwards to encapsulate the volume of air above the tank.

Other boundary conditions specific to the secondary phase as well as the sliding mesh and MRF impeller models will be described below.

Spargers

The spargers were modeled as segments (shown in figure 3.7) instead of circles as in the study carried out by Deglon (1998) in order to keep the grid as structured as possible. The sparger dimensions were such that their areas were identical to those used by De-

Figure 3.7: Spargers for the numerical model

glon (1998).

Two common approaches for modeling the air flow through the spargers in stirred tanks and bubble columns are by means of source terms (Spicka et al., 2001; Deen et al., 2002; Lane et al., 2002; Rigopoulos and Jones, 2003; Khopkar et al., 2005; Gentric et al., 2005) or velocity inlets (Morud and Hjertager, 1996; Kerdouss et al., 2006). The spargers in this study were modeled as velocity inlets. The gas velocity at the spargers was determined from the superficial velocity used by Deglon (1998) . The gas volume fraction is very difficult to measure experimentally at the spargers, therefore a gas volume fraction was estimated assuming quiescent conditions in the immediate vicinity of the spargers. The equation for the bubble-swarm velocity, u_{swarm}, is given by

$$u_{swarm} = \frac{J_g}{\phi} \tag{3.1}$$

Where J_g is the superficial gas velocity and ϕ is the gas volume fraction. The bubble-swarm velocity can be approximated using the gas hold up for the lowest impeller

rotational speed used by Deglon (1998) (310 RPM) and the superficial gas velocity. The gas hold up can then be calculated from the previously mentioned swarm velocity and be assumed to be the volume fraction of air at the spargers.

Air Free Surface

An outflow boundary was prescribed at the top surface, i.e., above the volume of air, to allow air to freely leave the system.

MRF Model Boundary Conditions

Periodic boundaries were specified as they were for the single phase model. Separate cell zones were defined for the fluid zones described in section 3.2.3. The faces separating the bulk tank from the region encapsulating the impeller were grouped and defined as an interior boundary. The interior boundary is located at 1.5 blade heights above and below and half the impeller diameter (D/2) away from the impeller blades. The interior boundary is shown in figure 3.8.

Sliding Mesh Model Boundary Conditions

For the Sliding Mesh model, separate cell zones must have distinct faces on each side of the sliding boundary. The faces from each cell zone are defined as interface boundaries. The interface boundaries are shown in figure 3.9. The sliding boundary is situated at 1.5 blade heights above and below and half the impeller diameter (D/2) away from the impeller blades.

3.3.4 Initial Gas Hold Up

Gas hold up requires a substantial calculation time to reach a steady state. For this reason, it was decided to patch various initial gas hold up concentrations into the stirred tank with a view to shortening the time to a solution. Initial concentrations of 0.15, 25 and 70 percent of the gas hold up values measured by Deglon (1998) were patched into the tank. In addition to this, the 360 ° model was simulated using the MRF model and this flow field was then used as the input for the sliding mesh model. These initial patched values will be referred to as GH1, GH2, GH3 and GH 4 from now on.

Zero concentration of air was patched into the stirred tank for the MRF model, as

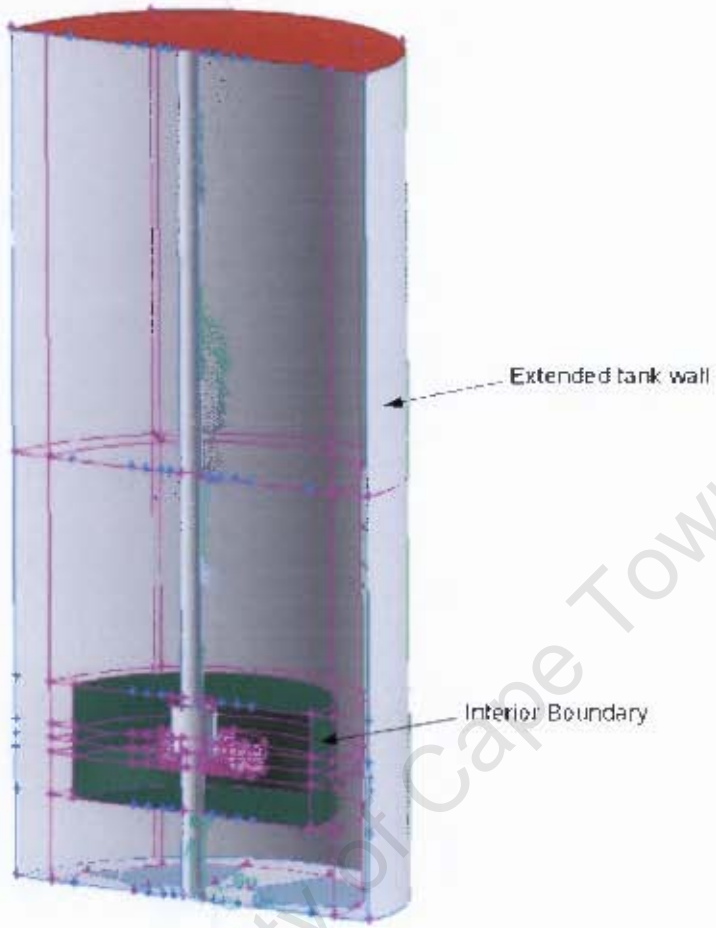

Figure 3.8: Wall and interface boundary conditions in tank

calculation times for this model were significantly shorter than those for the sliding mesh model.

3.3.5 Multiphase Model

The Eulerian multiphase model was used for this study. This model was used by Gosman et al. (1992), Ranade and van den Akker (1994), Lane et al. (2002) and Khopkar et al. (2005). The Schiller and Naumann (1933) model was used for interphase momentum transfer and virtual mass and lift forces were not considered. If bubbles are small and the superficial gas velocity is low, it can be assumed that the flow is not seriously disturbed by the presence of gas (van't Riet and Smith, 1973). Furthermore, Khopkar et al. (2005) reported that the turbulent dispersion terms were only significant in the impeller stream and that even there, the influence of the dispersion terms on the overall results were not

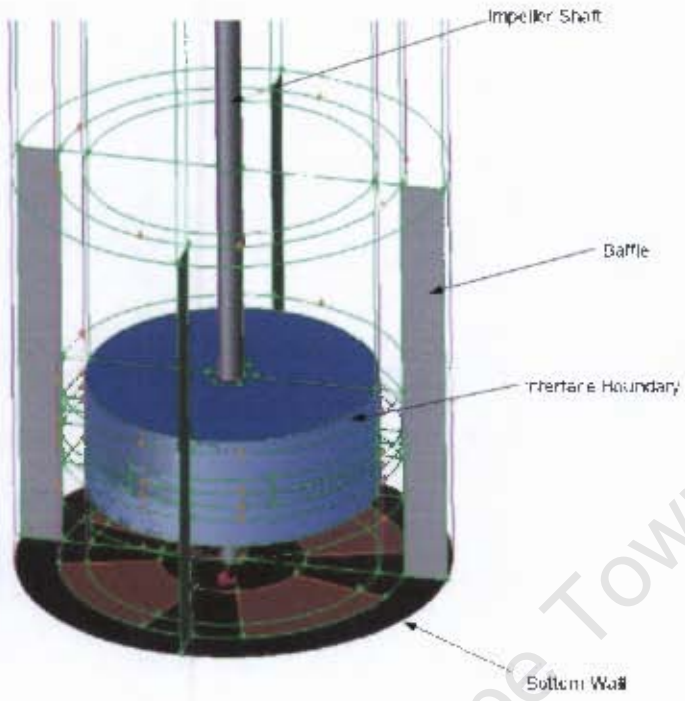

Figure 3.9: Wall and interface boundary conditions in tank

quantitatively significant. For these reasons, the dispersed k-ϵ model (as opposed to the per-phase k-ϵ model) was used to model turbulence.

3.3.6 Grid Resolution and Bubble Size

FLUENT® treats the bubbles as a dispersed phase in each control volume and it is assumed that a bubble and the fluid encapsulating the bubble form a continuum. For the dispersed k-ϵ model, the primary phase dominates the motion of the secondary phase and the influence of individual bubbles on the flow field becomes insignificant. Therefore, to avoid numerical instability and to ensure that the influence of the secondary phase on the flow field is insignificant, the bubble should be smaller than the grid spacing. The smallest grid interval size occurred at the impeller shaft, as shown in figures 3.10 and 3.11.

A single bubble size, corresponding to the experimental value of d_b 0.2 mm, given by Deglon (1998), was used. Single bubble sizes were also used by Ranade and van den Akker (1994) (6 mm), Ranade and Deshpande (1999) (2 mm), Deen et al. (2002) (2 and 4 mm), Khopkar et al. (2005) (4 mm) and Kerdouss et al. (2006) (2 mm). Bubble

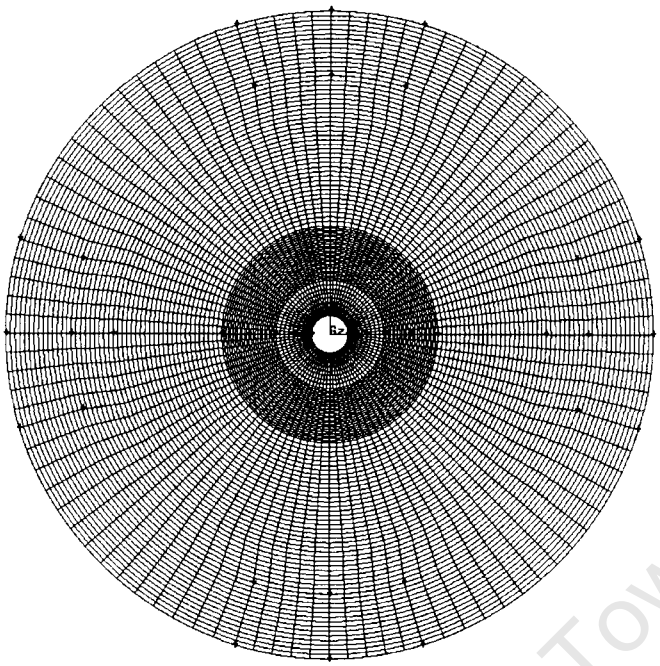

Figure 3.10: Plan view of tank mesh

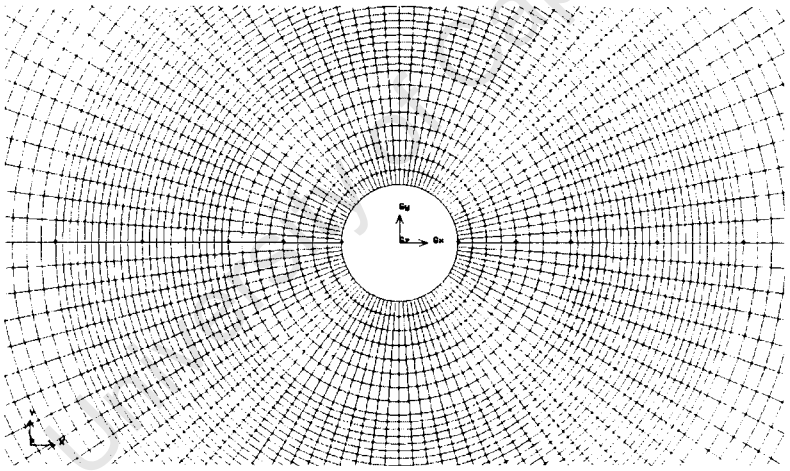

Figure 3.11: Close up view of tank mesh (impeller shaft at the center)

break-up and coalescence were not considered. The densities for the grids used for the MRF and sliding mesh models are given in table 3.3. Note that the regions defined in table 3.3 are the same regions defined in figures 3.4 and 3.5. The grid densities range from 246 000 to 1.2 million cells for the MRF model, while a grid of approximately 1.35 million cells was used for the sliding mesh model (Grid SM).

Table 3.3: Control volume distribution for various grids

	Grid 1	Grid 2	Grid 3	Grid 4	Grid SM
Blade Region	11 520	11 520	11 520	30 720	11 520
Hub region	5 040	5 040	5 040	10 752	5 760
Blade Edge Region	17 280	36 000	37 440	101 376	22 080
Impeller Discharge Region (top)	23 688	36 792	37 800	62 496	69 984
Impeller Discharge Region (bottom)	23 688	36 792	37 800	62 496	74 208
Bulk Region (top)	42 300	131 400	199 800	330 336	376 512
Bulk Region (bottom)	23 688	73 584	126 900	209 808	142 464
Outer Region	28 188	45 360	85 176	121 632	188 160
Air Section	70 560	140 436	224 280	241 392	450 240
Total	245 952	516 924	765 168	1 171 008	1 340 928

3.4 Data Validation

Wu and Patterson (1989) presented an extensive phase averaged LDV data set in the form of axial profiles of mean velocities and RMS turbulent velocities. The profiles were presented for a Rushton turbine-agitated stirred tank with $T = 0.27$ m. Experimental studies by Costes and Couderc (1988), Wu and Patterson (1989) and Dyster et al. (1993) have shown that for turbulent flow in geometrically similar stirred tanks, mean velocity and turbulent kinetic energy profiles normalized with the impeller tip velocity (U_{tip}) and the impeller tip velocity squared (U_{tip}^2) respectively, were independent of impeller speed. For these reasons, the data presented by Wu and Patterson (1989) was used to validate the single phase model. In addition, numerical data presented by Siwale (2004) was used to further validate the single phase model, as the numerical model used by the author was similar to the model used in this study. Finally, experimental data published by Deglon (1998) was also used to validate the single phase model. For the purpose of comparison with the data presented by Deglon (1998), the single phase model was evaluated in terms of mean velocities, turbulence parameters and power draw for a range of impeller speeds.

The multiphase model was validated using multiphase experimental data published by Deglon (1998), as this data set contained detailed turbulence parameter information for

an aerated stirred tank. Data measurement techniques will be described in this section followed by a motivation for the use of the previously mentioned experimental and numerical data sets as validation for this study.

3.4.1 Data Measurement

The points used for data sampling in this study correspond to those used by Deglon (1998) (see figure 3.12). For this study, data was sampled instantaneously and the instantaneous data was also averaged, in an effort to reproduce phase resolved as well as phase unresolved experimental data.

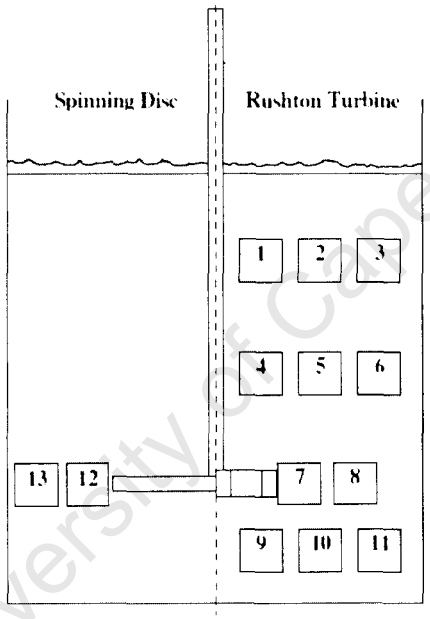

Figure 3.12: Measurement points used in this study (Deglon, 1998)

In the case of phase-resolved data, the impeller position is recorded with each measurement. However, the impeller position is not taken into account with phase unresolved measurements. As information about the impeller angle is not contained in phase unresolved data, only phase averaged data can be obtained. Techniques for simulating phase averaged and phase resolved data will be presented in this section.

Circumferential Averaging

To simulate phase averaged data, measurements were sampled at points along radially clipped surfaces (see figure 3.13), where the number of points is dependent on the grid density. The surfaces were made as thin as possible to approximate lines. The data along each surface was averaged to yield one value per measurement location, shown in figure 3.12.

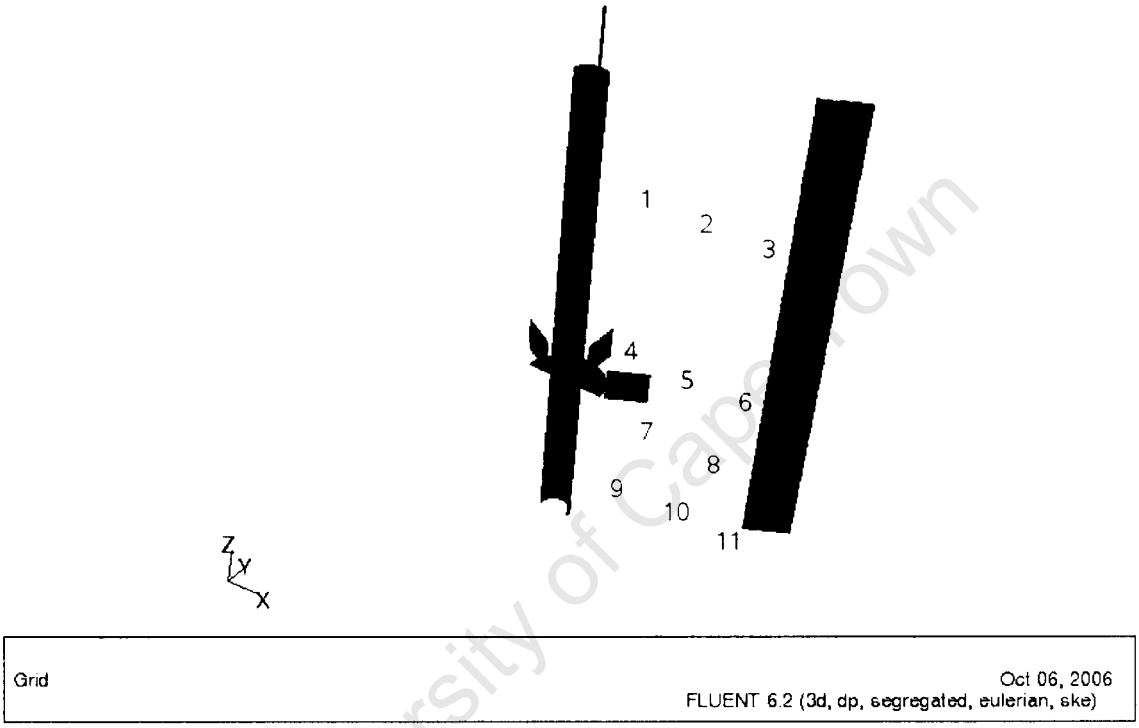

Figure 3.13: Clipped surfaces used for measurement in tank

Instantaneous Measurements

Instantaneous measurements were made at point surfaces corresponding to the points used by Deglon (1998) in figure 3.12, at 45° to the baffle plane, i.e., midway between two baffles. These points are shown in figure 3.14.

3.4.2 Experimental Data

As previously stated, the single phase model will be validated with single phase data presented by Wu and Patterson (1989), Siwale (2004) and Deglon (1998). The multi-phase model will be primarily validated using data published by Deglon (1998). Even

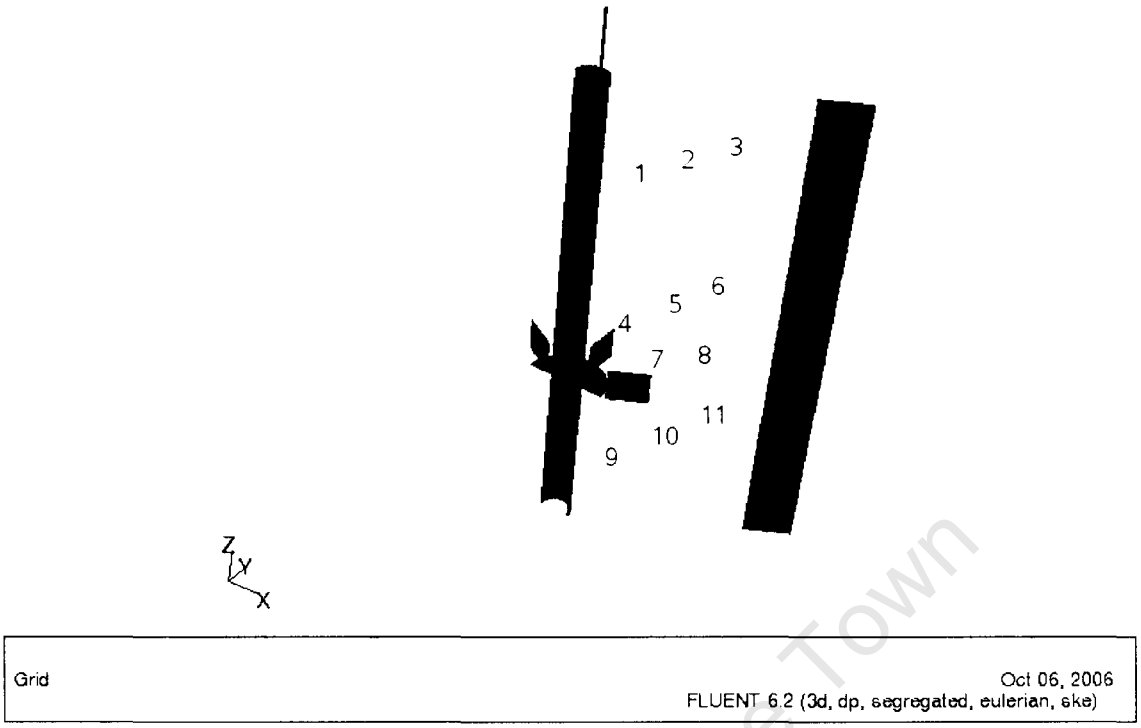

Figure 3.14: Instantaneous measurement points used in this study

though the electrochemical probe used by the author produced only "reasonably" accurate velocity measurements, accurate RMS velocities were reported assuming isotropic turbulence. This data set was used as the benchmark for this study in the absence of a more accurate data set. Furthermore, it will be useful to compare the multiphase data to the data published by Wu and Patterson (1989). Even though the authors presented only single phase data, the measurement technique used is more accurate than that used by Deglon (1998) and the profiles are not expected to differ significantly in the outflow of the impeller. For these reasons, the Wu and Patterson (1989) will be for additional validation for the multiphase model.

Chapter 4

Results and Discussion

The results for the single and multiphase models are presented in this chapter. Single phase data was validated in terms of axial profiles of mean velocity and turbulent kinetic energy using experimental data published by Wu and Patterson (1989) and numerical data presented by Siwale (2004). In addition, the single phase results were further validated with single phase data published by Deglon (1998). In the absence of a more accurate data set, the multiphase model was validated with experimental data published by Deglon (1998). Multiphase data was also validated using experimental data published by Wu and Patterson (1989) and numerical data presented by Siwale (2004). Even though these authors presented only single phase data, the correlation between these data sets and the multiphase data from this study was of interest. The results are discussed at the end of this chapter.

4.1 Single Phase Results

4.1.1 Comparison with Wu and Patterson and Siwale Data

Mean Velocity Profiles

The radial velocity profiles for the entire range of impeller speeds are plotted in figure 4.1. Radial velocities are slightly over predicted in the impeller discharge stream, but predictions are generally accurate. Tangential velocity profiles are plotted in figure 4.2 for the entire range of impeller speeds. Tangential velocities are slightly over predicted in the impeller stream, but the predictions are otherwise consistent with the profiles of Wu and Patterson (1989) and Siwale (2004).

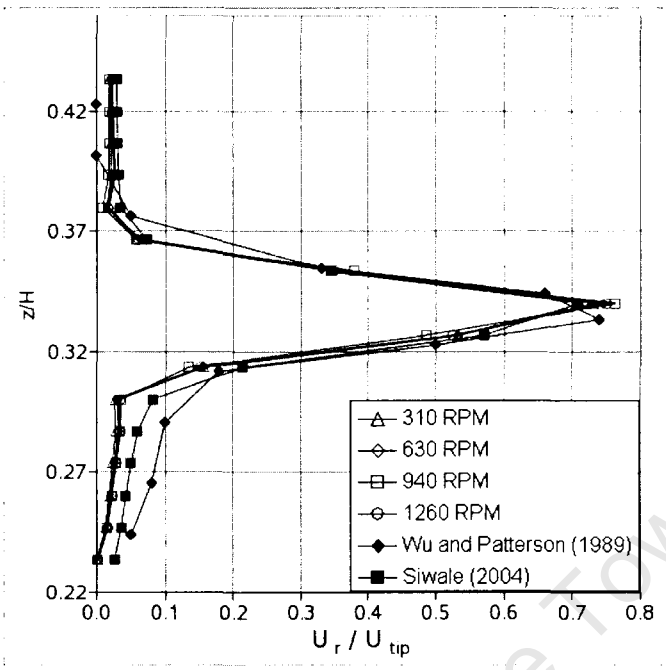

Figure 4.1: Axial profiles of normalized radial velocity at r/T =0.185

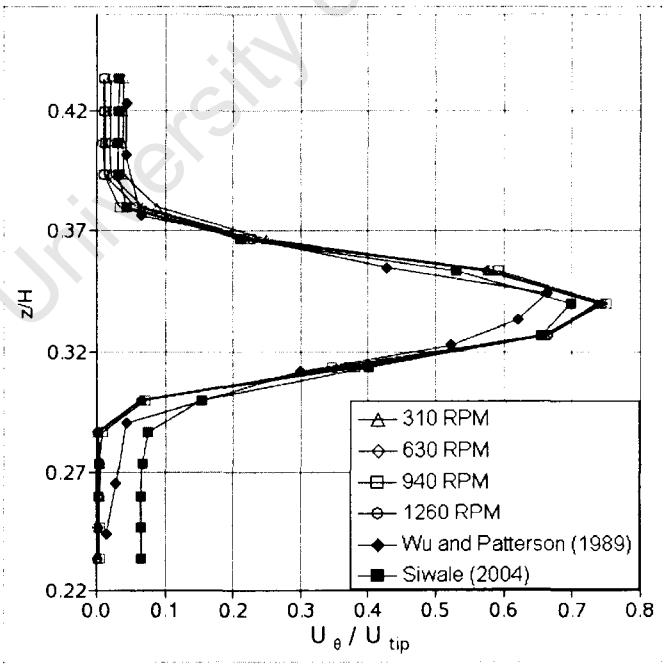

Figure 4.2: Axial profiles of normalized tangential velocity at r/T =0.185

Turbulent Kinetic Energy Profiles

Turbulent kinetic energy profiles for the entire range of impeller speeds at normalized radial distances of r/T = 0.185 and r/T = 0.285 are plotted in figures 4.3 and 4.4. The profiles show good correlation with those of Siwale (2004) and follow the same trend as those of Wu and Patterson (1989).

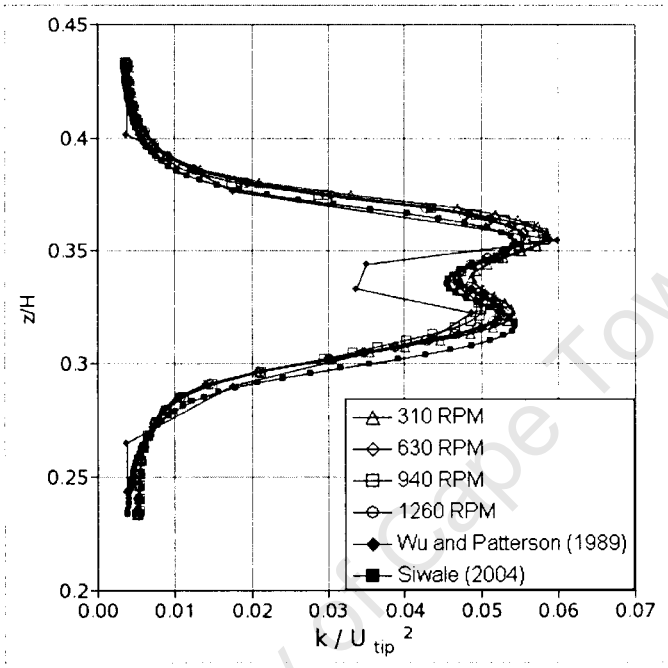

Figure 4.3: Axial profiles of normalized TKE at r/T =0.185

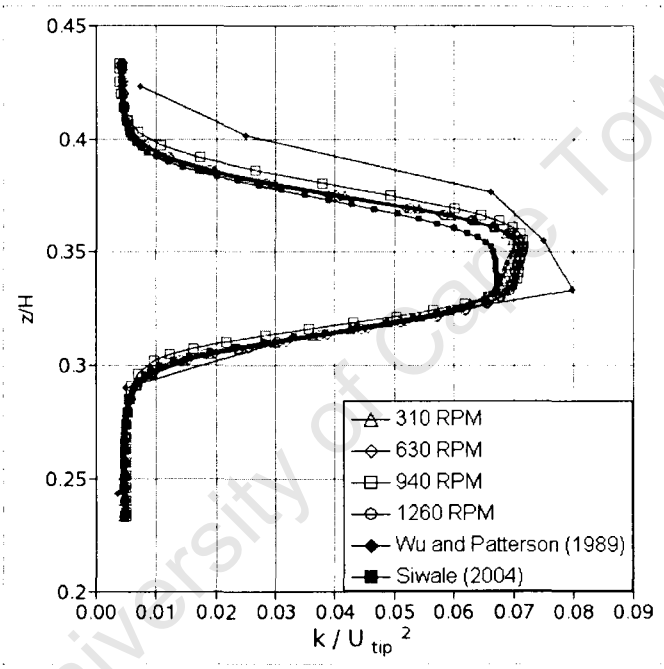

Figure 4.4: Axial profiles of normalized TKE at r/T =0.285

4.1.2 Comparison with Deglon Data

Mean Tangential Velocity

The numerical and experimental tangential velocities in the bulk tank for a range of impeller speeds are plotted in figure 4.5. The bulk tank velocities for both studies (Deglon (1998) and current study) were arithmetically averaged from the sum of the measurement points 1 - 6 and 9 - 11 (see figure 4.5) in the tank. There is generally poor agreement between the numerical and experimental data. The significant difference in the two data sets is thought to be due to the inaccuracy associated with the measurement technique (electrochemical probe) used by Deglon (1998). The numerical and

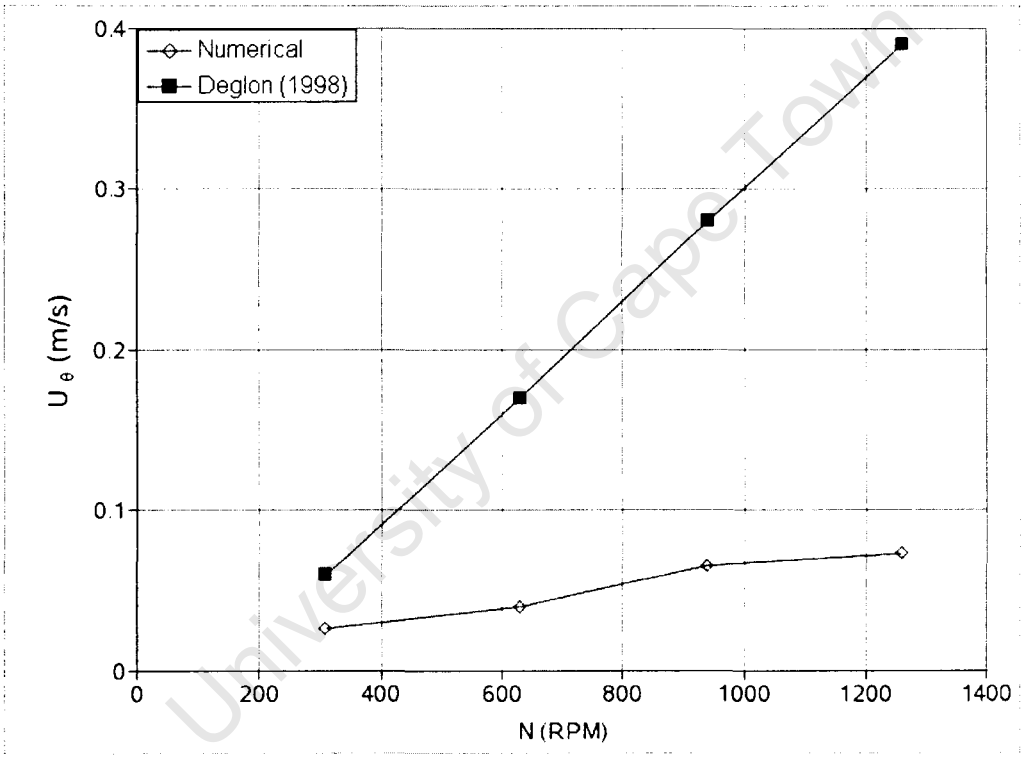

Figure 4.5: Mean tangential velocity vs impeller speed in the bulk tank

experimental mean velocities in the impeller stream are shown in figure 4.6. For this case, the agreement between the data sets is improved, compared to the bulk tank.

The numerical and experimental velocities at the impeller tip are shown in figure 4.7. With the exception of the last data point, the correlation between the tangential components from the two data sets is good.

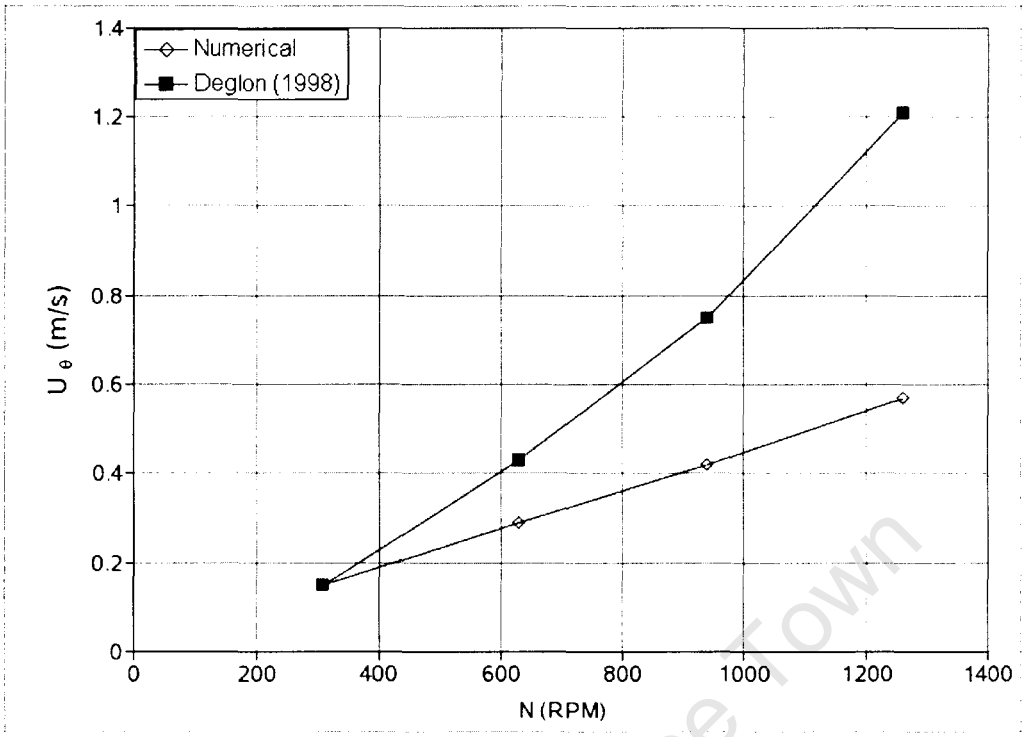

Figure 4.6: Mean tangential velocity vs impeller speed in the impeller stream

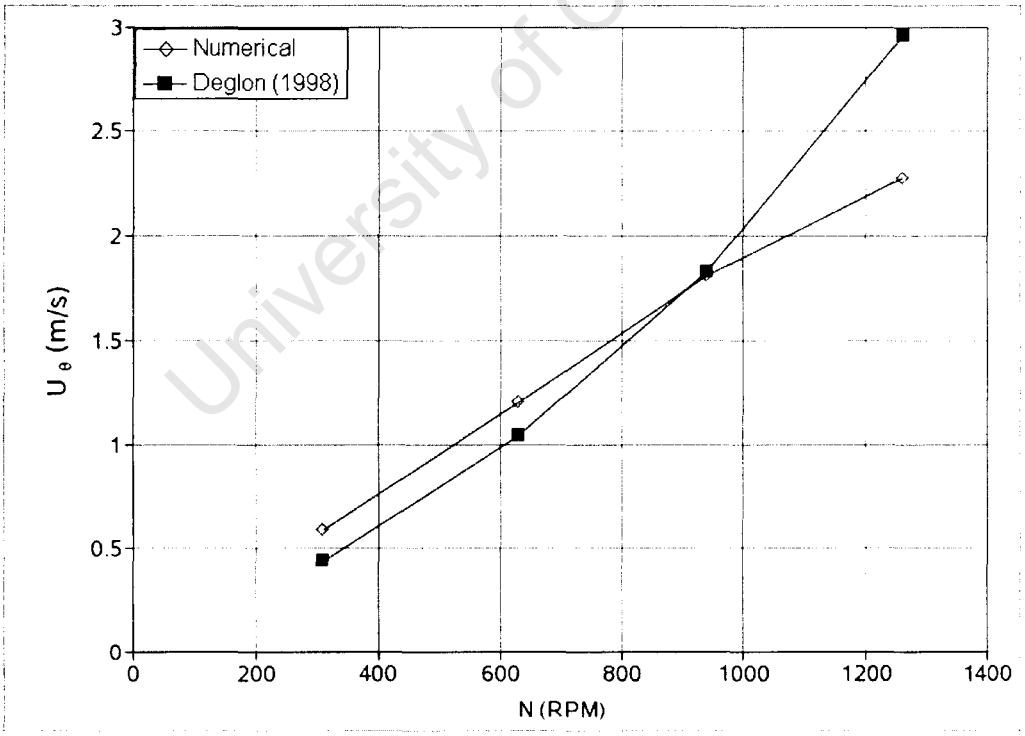

Figure 4.7: Mean tangential velocity vs impeller speed at the impeller tip

Turbulent RMS Velocity

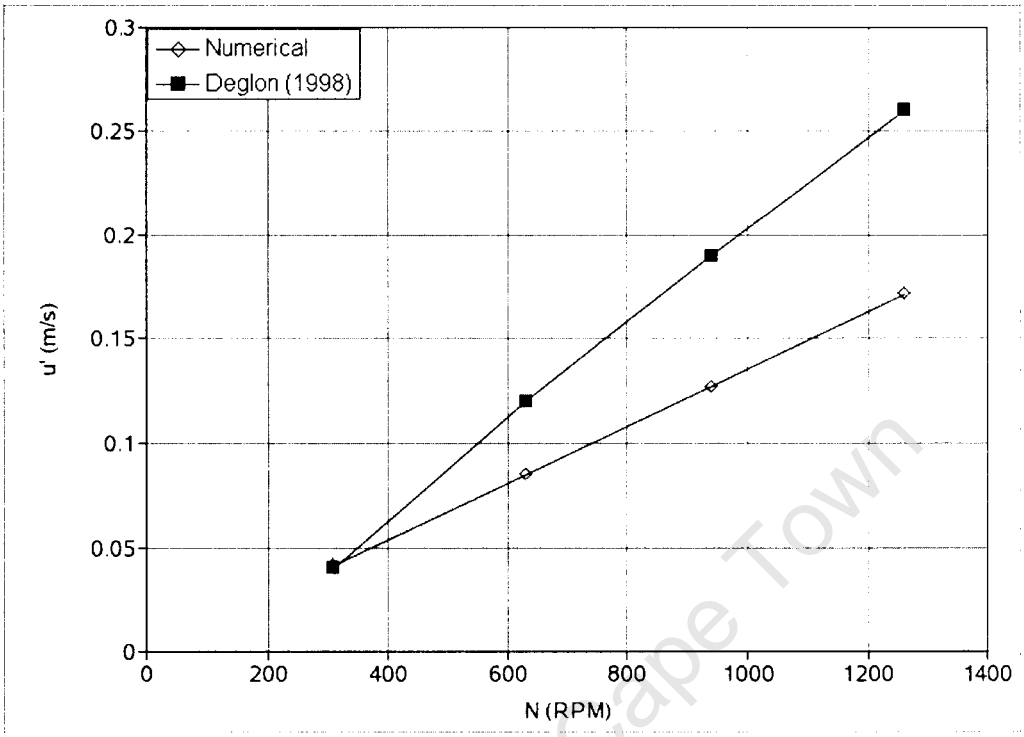

Figure 4.8: RMS velocity vs impeller speed in the bulk tank

The numerical and experimental turbulent RMS velocities in the bulk tank are plotted in figure 4.8. In the bulk tank, the correlation between the experimental and numerical data is generally poor and even though the trends are similar, the discrepancy is exacerbated with increasing impeller speeds. The poor correlation here is also thought to be due to the measurement technique used by Deglon (1998).

The numerical and experimental turbulent RMS velocities in the impeller stream are plotted in figure 4.9. Agreement is good over the full range of impeller speeds.

The numerical and experimental turbulent RMS velocities at the impeller tip is shown in figure 4.10. RMS velocities are under predicted over the range of impeller speeds, however the two sets of results are comparable.

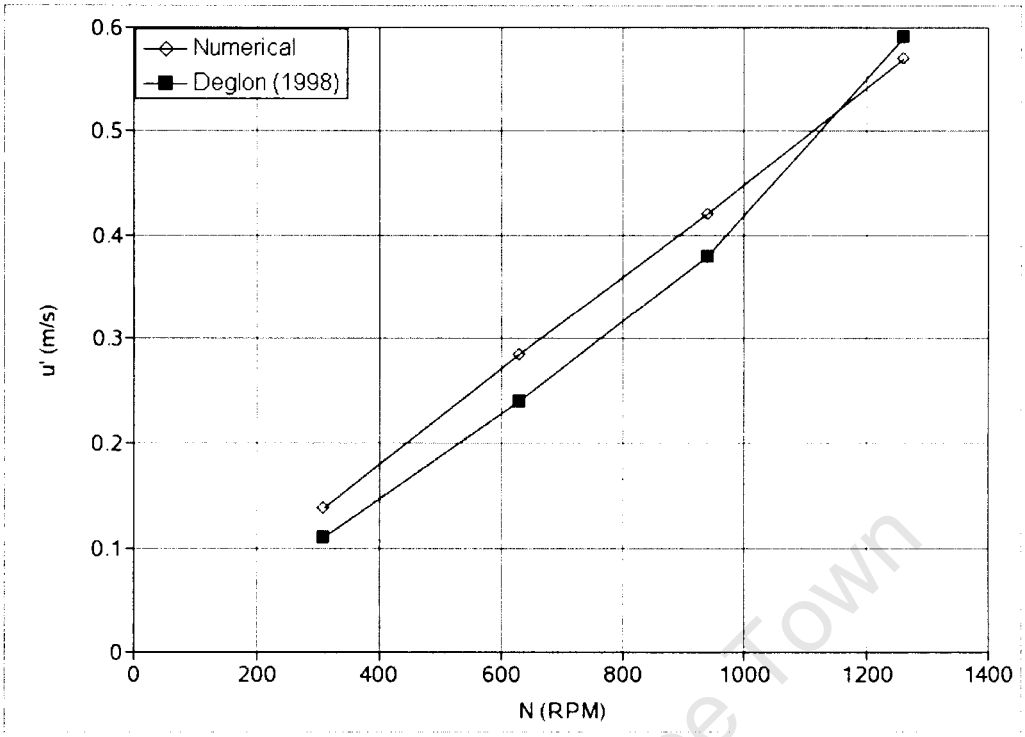

Figure 4.9: RMS velocity vs impeller speed in the impeller stream

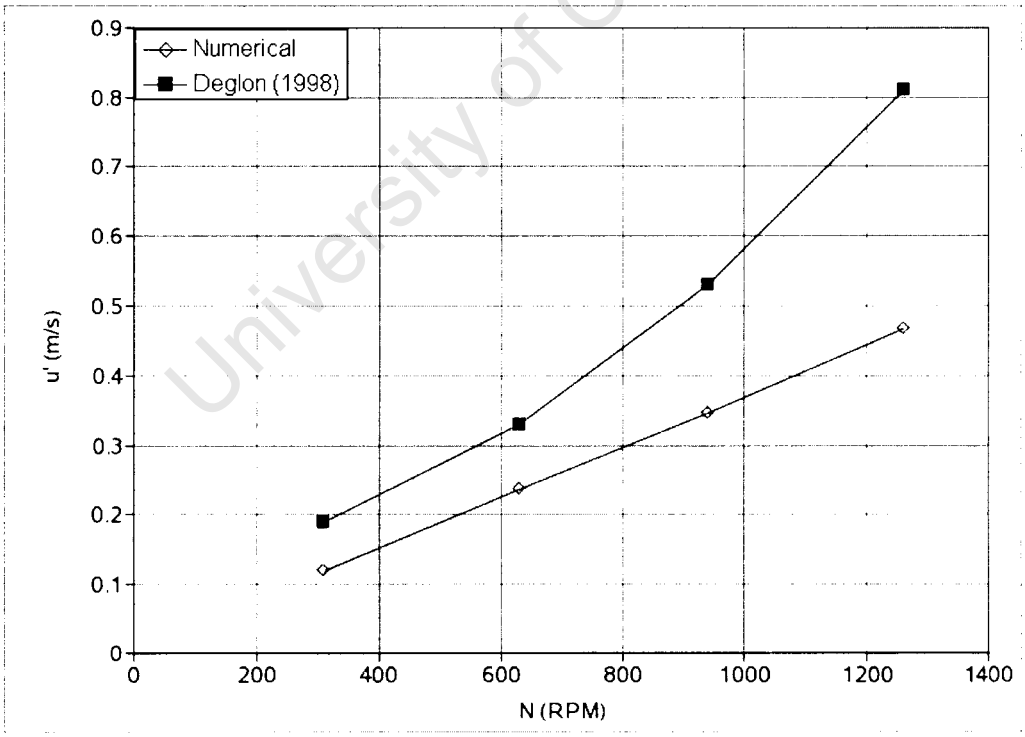

Figure 4.10: RMS velocity vs impeller speed at the impeller tip

Turbulent Dissipation Rate

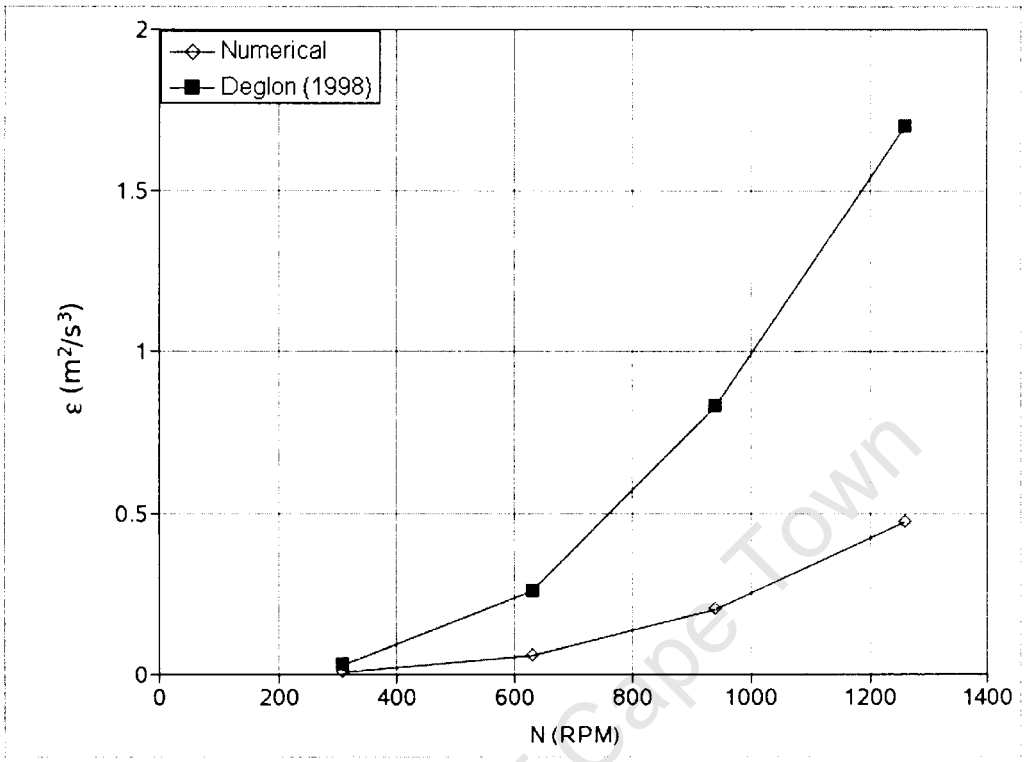

Figure 4.11: Turbulent dissipation rate vs impeller speed in the bulk tank

The numerical and experimental turbulent dissipation rates in the bulk tank are plotted in figure 4.11. The agreement between the two sets of data is poor, but the trends are similar. The reason for the poor correlation is the same as the one for the poor mean and RMS velocity correlation, i.e., possible inaccuracies associated with the measurement technique used by Deglon (1998).

The numerical and experimental turbulent dissipation rates in the impeller stream and at the impeller tip are plotted in figures 4.12 and 4.14. The trends for the two sets of data are similar and the agreement is significantly improved compared to the bulk tank. The correlation between experimental and numerical data is good.

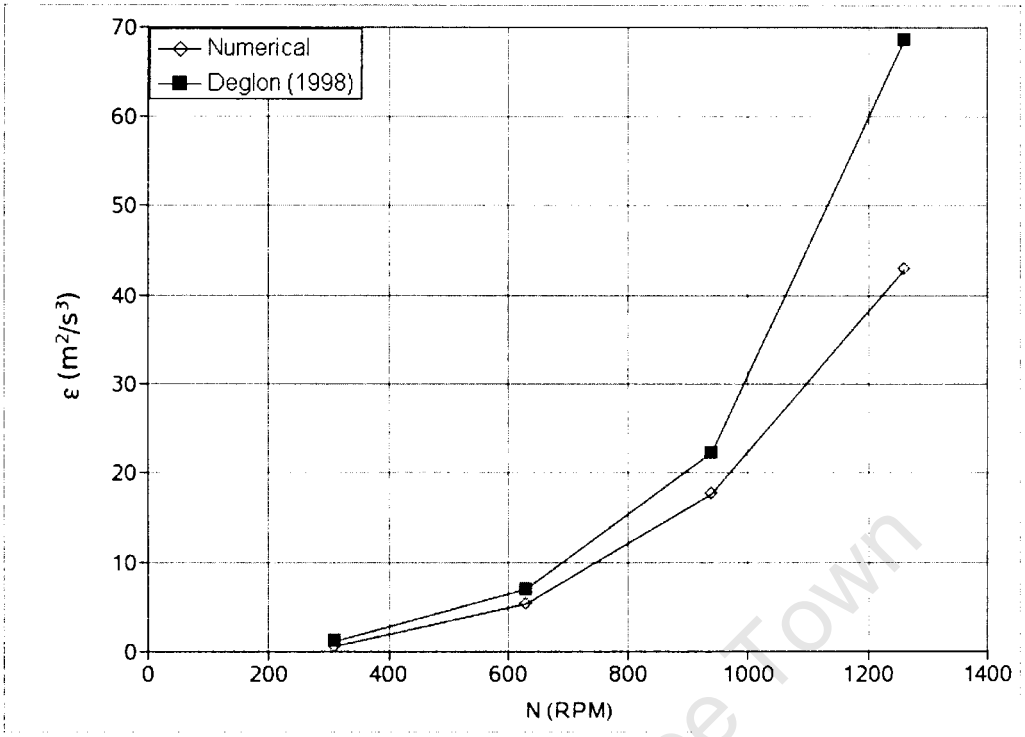

Figure 4.12: Turbulent dissipation rate vs impeller speed in the impeller stream

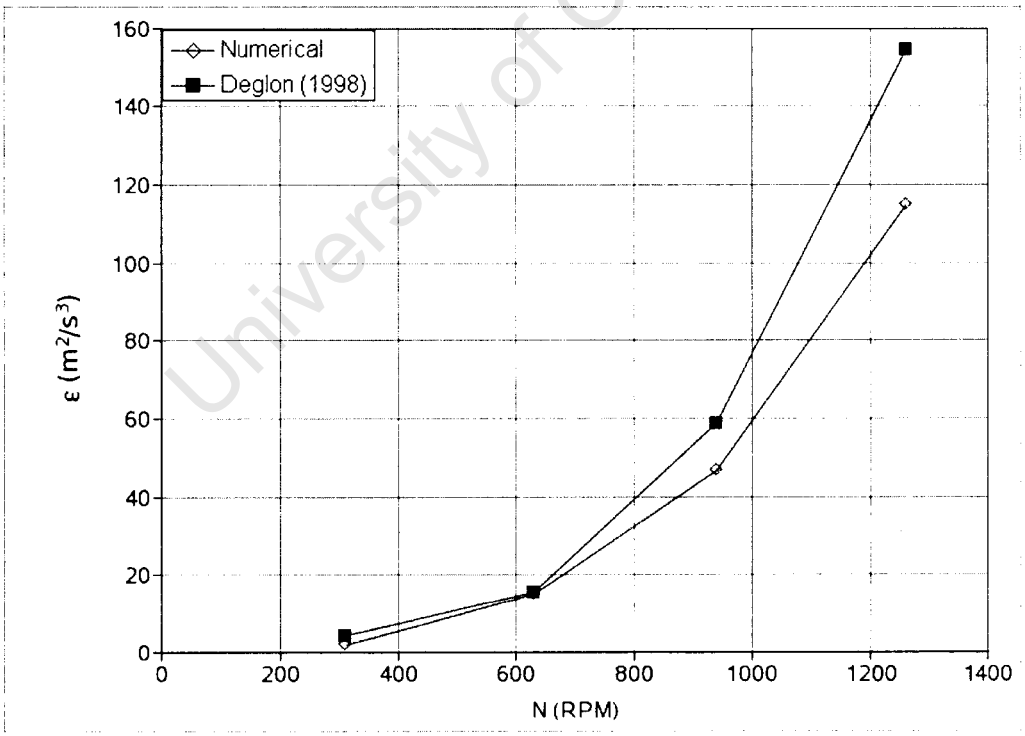

Figure 4.13: Turbulent dissipation rate vs impeller speed at the impeller tip

Power Draw

Power per unit mass for the numerical and experimental tanks are plotted in figure 4.14. The numerical data accurately predicts the experimental data. This is expected as a higher order discretisation scheme was used for all simulations and the experimental torque (and therefore power) measurements were reported to an accuracy of 0.05 Watts by Deglon (1998).

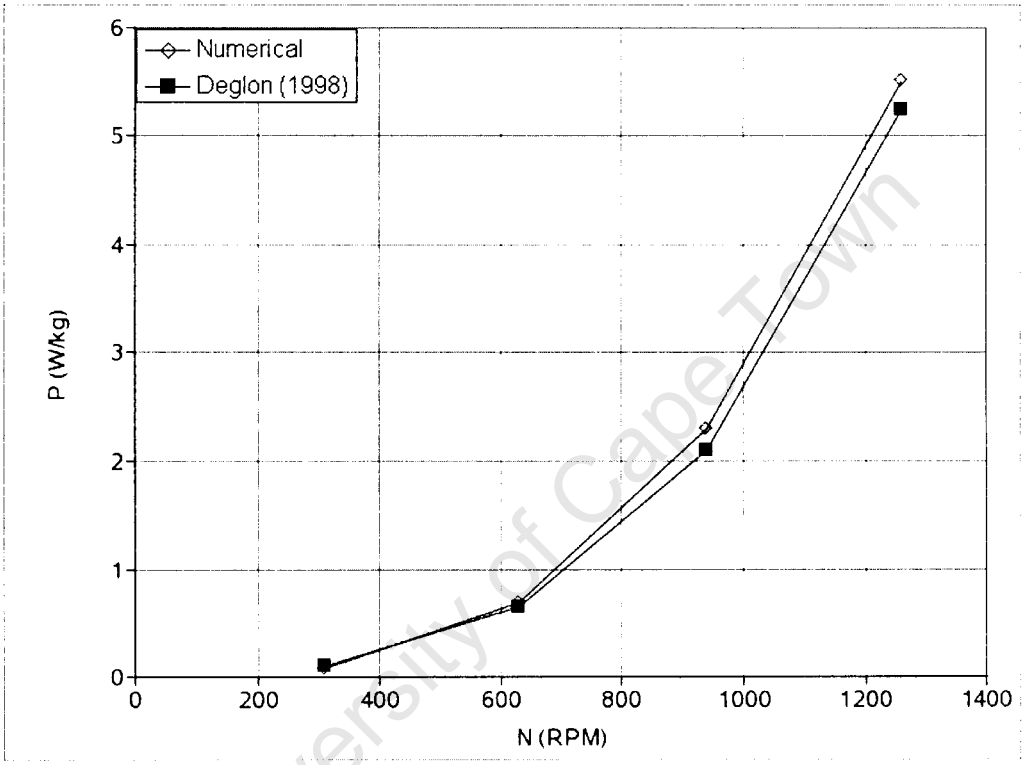

Figure 4.14: Power draw vs impeller rotational speed

4.2 Multiphase Results

The results for the multiphase model described in Chapter 3 are presented here. Simulations were carried out for an impeller rotational speed of 940 RPM. The Eulerian mixture model was used, in conjunction with the MRF and sliding mesh models to model the impeller rotation. The dispersed k-ϵ turbulence model was used to model turbulence. The first order implicit solver formulation was used and a fixed time step,

Table 4.1: Time step size and time steps per revolution

$N(RPM)$	No of Intervals	Δt	Number of Δt per revolution
940	48	6.65 X 10 $^{-04}$	96

shown in table 4.1, was used for all sliding mesh simulations. The number of control volumes at the sliding interface as well as the impeller rotational speed were used to determine the time step size. These are shown in table 4.1. Using this method to determine the time step resulted in the grid moving by one control volume per time step at the sliding interface. This is consistent with the methods of Wechsler et al. (1999) and Deen et al. (2002).

A convergence criterion of 1×10^{-3} for all residuals was used for all simulations. However, the MRF model did not converge to this criterion, as residuals typically converged to between 2×10^{-3} and 5×10^{-3}. In light of this, simulations were carried for 30 000 iterations (after which all residuals converged to the within the previously mentioned range) before data was sampled.

The results were firstly compared to experimental and numerical data presented by Wu and Patterson (1989) and Siwale (2004), respectively and evaluated in terms of axial profiles of mean velocity and turbulent kinetic energy. It should be noted that Wu and Patterson (1989) as well as Siwale (2004) presented only single phase data. However, the single phase data provides a useful benchmark against which to gauge the state of the multiphase flow field. Therefore, while exact correlation between the two data sets was not expected, the trends for, or more specifically any possible similarity between the trends for the single and multiphase data sets, were of interest. In addition, data was further validated using experimental data published by Deglon (1998). The model was evaluated in terms of mean velocities, turbulent dissipation rate, power draw

and gas hold up. The results are discussed at the end of this chapter.

4.2.1 Comparison with Wu and Patterson and Siwale Data

Siwale (2004) and Wechsler et al. (1999) reported that fine grids (in excess of 1 000 000 control volumes) were necessary to resolve turbulent kinetic energy. For this reason, the influence of grid density on mean velocity and turbulent kinetic energy profiles was investigated using the MRF impeller model. The influence of initial gas hold up concentrations on mean velocity and turbulent kinetic energy profiles was also investigated, using the sliding mesh model. The initial concentrations were GH 1, GH 2, GH 3, corresponding to 0.15 %, 25 % and 70 % of the experimental gas hold up measured by Deglon (1998), respectively. A MRF solution (GH 4) was also used as the initial condition for the sliding mesh model

Mean Velocity Profiles

Radial and tangential velocity profiles, resulting from an initial gas hold up of GH 1, are plotted in figures 4.15 and 4.17. Mean velocities are under predicted in the impeller stream, however the correlation with the Wu and Patterson (1989) and Siwale (2004) profiles improves with increasing impeller rotations. Contrary to the profiles resulting from an initial gas hold up of GH 1, profiles corresponding to an initial gas hold up concentration of GH 4 are consistent at 10, 20 and 30 impeller rotations (see figures 4.16 and 4.18). Profiles for GH 2 and GH 3 were consistent with those presented and are therefore not shown. The profiles presented are consistent with those of Wu and Patterson (1989) and Siwale (2004).

Radial and tangential velocity profiles for the grids investigated are plotted in figures 4.19 and 4.20. Note that Grid SM refers to the 360 ° model (sliding mesh grid), while all other grids refer to the 180 ° model. The mean velocity profiles are consistent with those of Wu and Patterson (1989) and Siwale (2004).

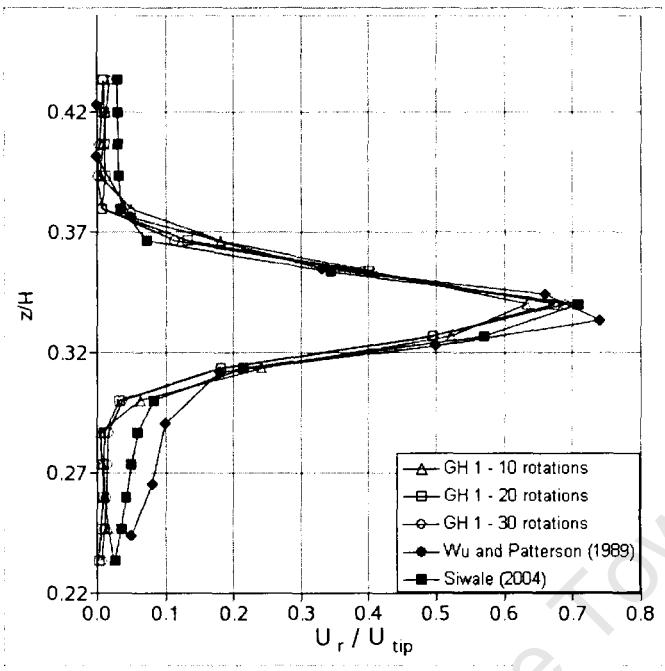

Figure 4.15: Axial profiles of normalized radial velocity for GH 1 at r/T = 0.185

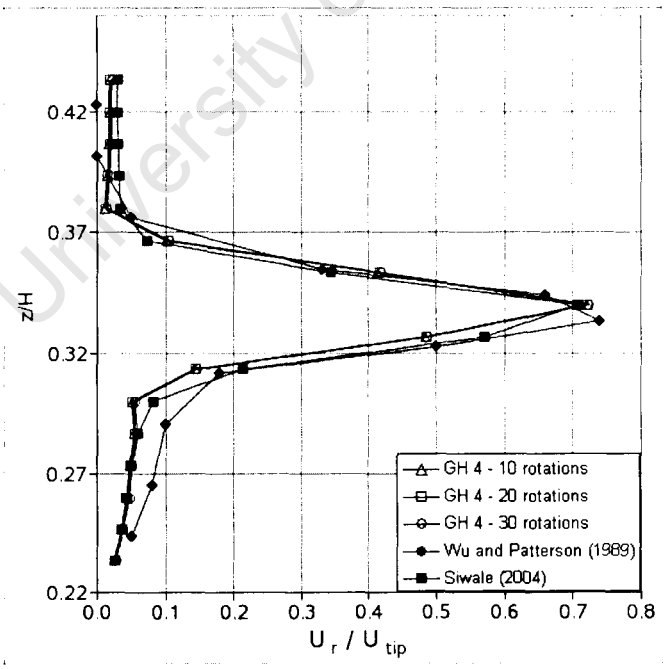

Figure 4.16: Axial profiles of normalized radial velocity for GH 4 at r/T = 0.185

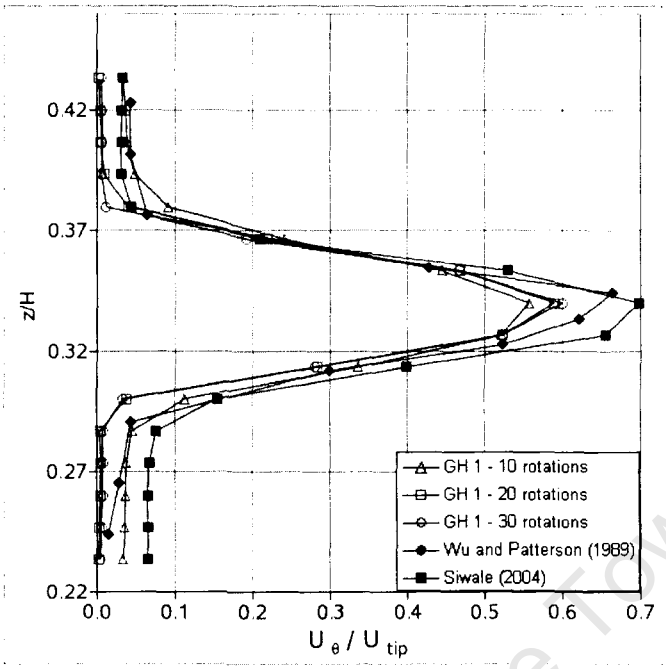

Figure 4.17: Axial profiles of normalized tangential velocity for GH 1 at r/T = 0.185

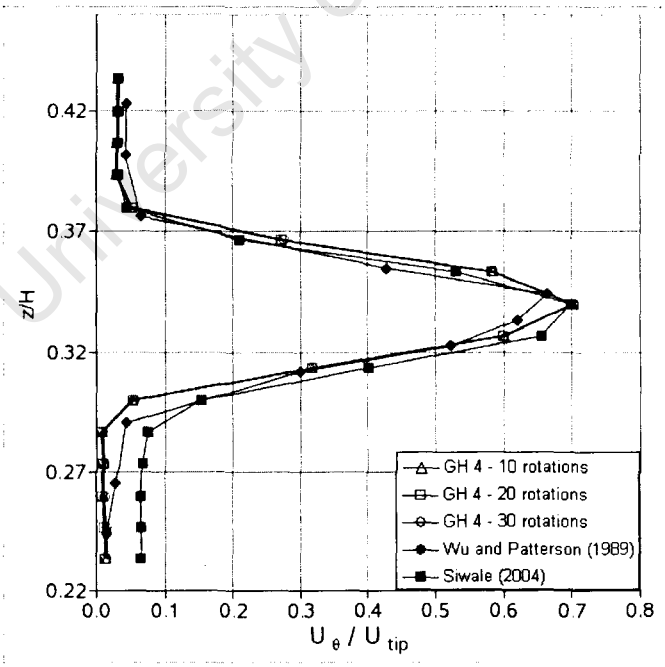

Figure 4.18: Axial profiles of normalized tangential velocity for GH 4 at r/T = 0.185

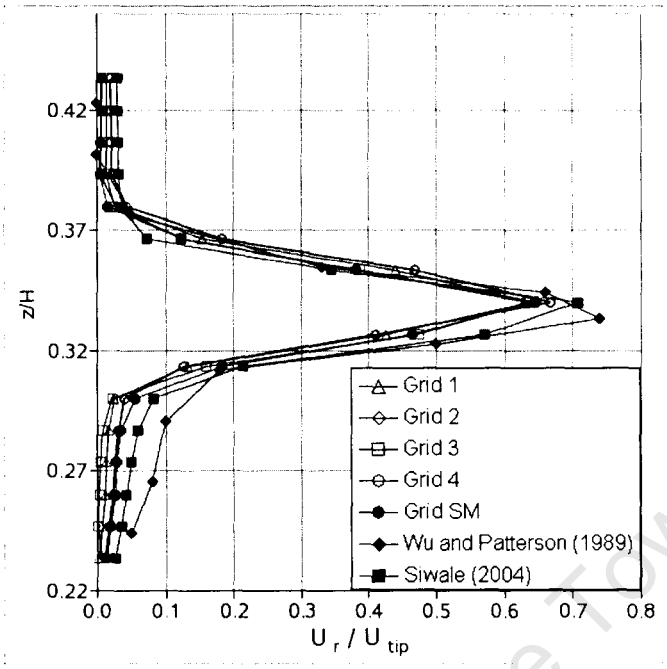

Figure 4.19: Axial profiles of normalized radial velocity at r/T = 0.185

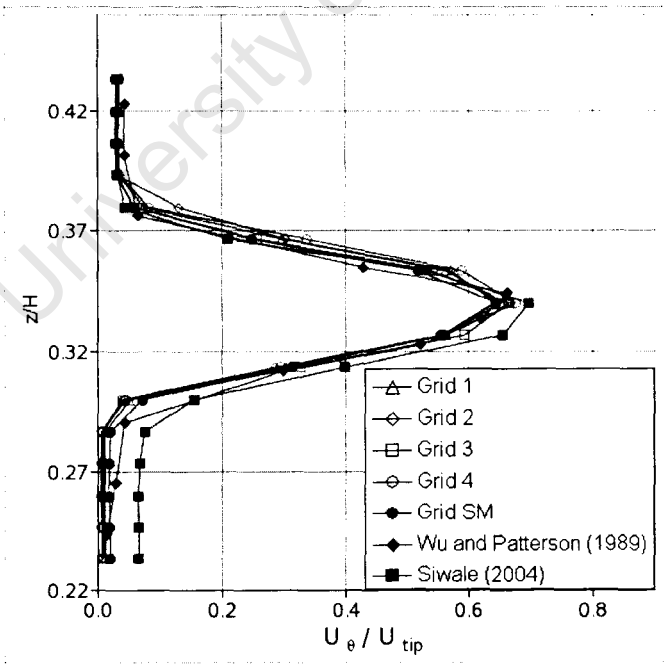

Figure 4.20: Axial profiles of normalized tangential velocity at r/T = 0.185

Turbulent Kinetic Energy Profiles

Turbulent kinetic energy profiles at 10, 20 and 30 impeller rotations, corresponding to an initial gas hold up of GH 1 are compared to profiles presented by Wu and Patterson (1989) and Siwale (2004) in figure 4.21. There is a notable difference in profiles with increasing impeller rotations. However, starting from initial gas hold up concentraions of GH 2 and GH 3 (see figures 4.22 and 4.23), the profiles show more consistency with increasing impeller rotations. There is no change in turbulent kinetic energy profiles corresponding to an initial gas hold up of GH 4 (see figure 4.24). These results tend to suggest that the flow field is not fully developed for simulations corresponding to GH 1, GH 2 and GH 3. Turbulent kinetic energy profiles at 10, 20 and 30 impeller rotations for simulations starting from initial concentrations of GH 1, GH 2, GH 3 and GH 4 are plotted in figures 4.25, 4.26, 4.27 and 4.28 respectively, at a normalized radial position of r/T = 0.285. All profiles under predict the profiles presented by Wu and Patterson (1989) and Siwale (2004). However, what was of interest was the inconsistency for profiles corresponding to GH 1 with increasing impeller rotations. A slight inconsistency for profiles corresponding to GH 2 and GH 3 was also noted with increasing impeller rotations. It should be noted that profiles corresponding to GH 4 show consistency with increasing impeller rotations. These plots suggest that the flow field is not fully developed for simulations corresponding to GH 1, GH 2 and GH 3.

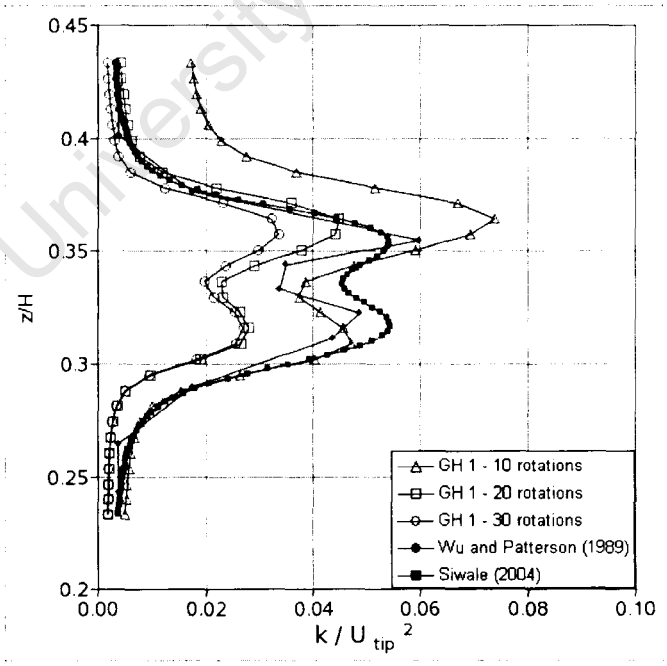

Figure 4.21: Axial profiles of normalized TKE velocity for GH 1 at r/T = 0.185

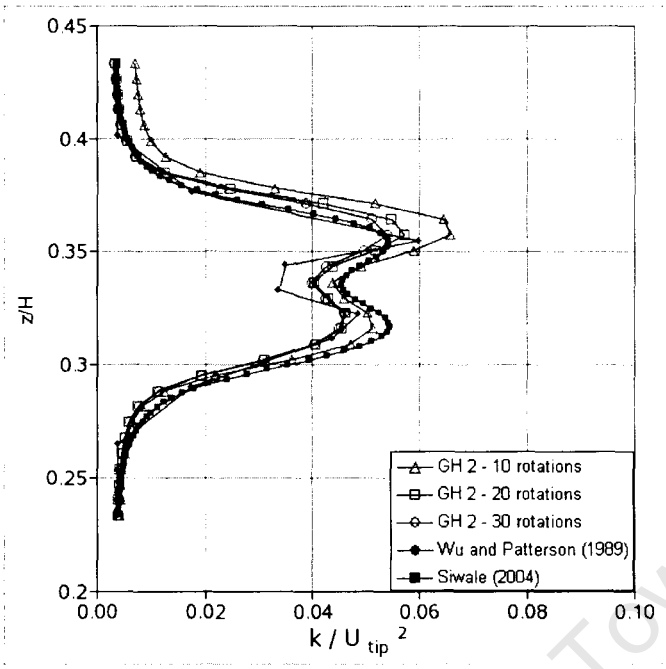

Figure 4.22: Axial profiles of normalized TKE velocity for GH 2 at r/T = 0.185

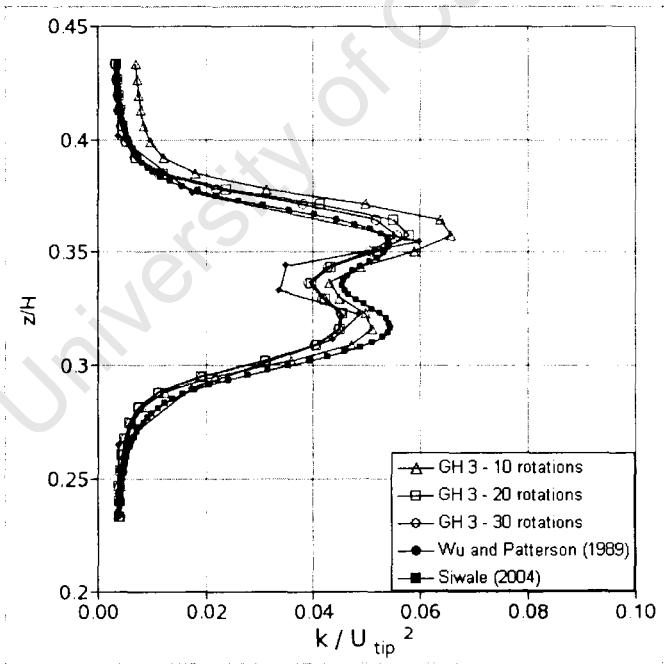

Figure 4.23: Axial profiles of normalized TKE velocity for GH 3 at r/T = 0.185

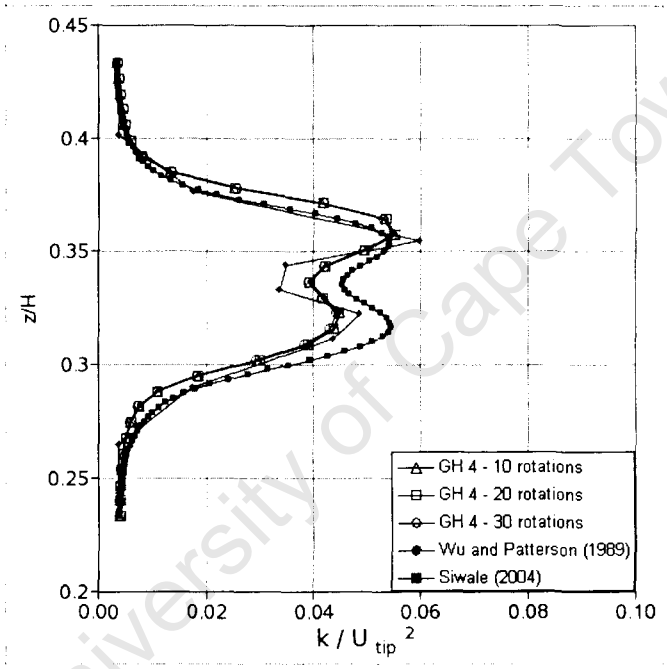

Figure 4.24: Axial profiles of normalized TKE velocity for GH 4 at r/T = 0.185

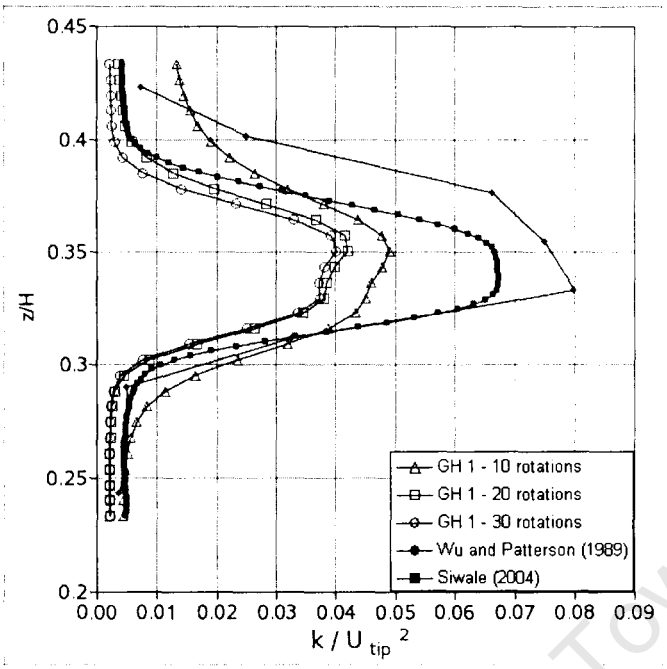

Figure 4.25: Axial profiles of normalized TKE velocity for GH 1 at r/T = 0.285

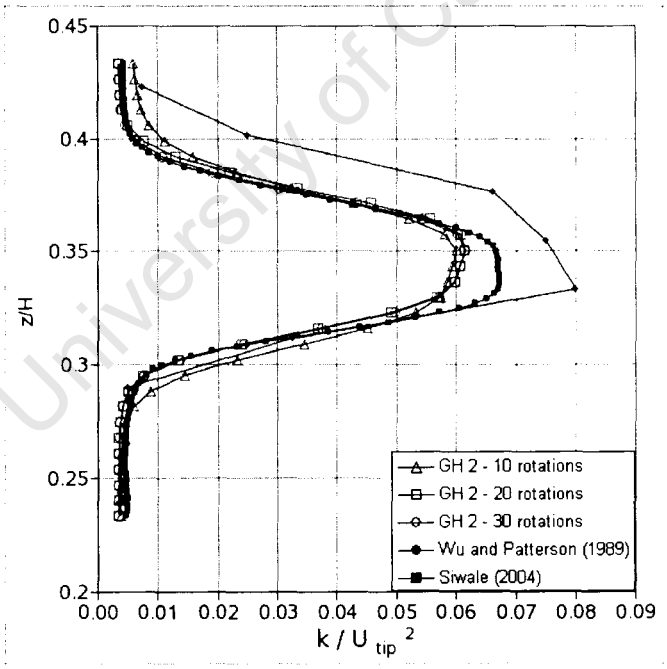

Figure 4.26: Axial profiles of normalized TKE velocity for GH 2 at r/T = 0.285

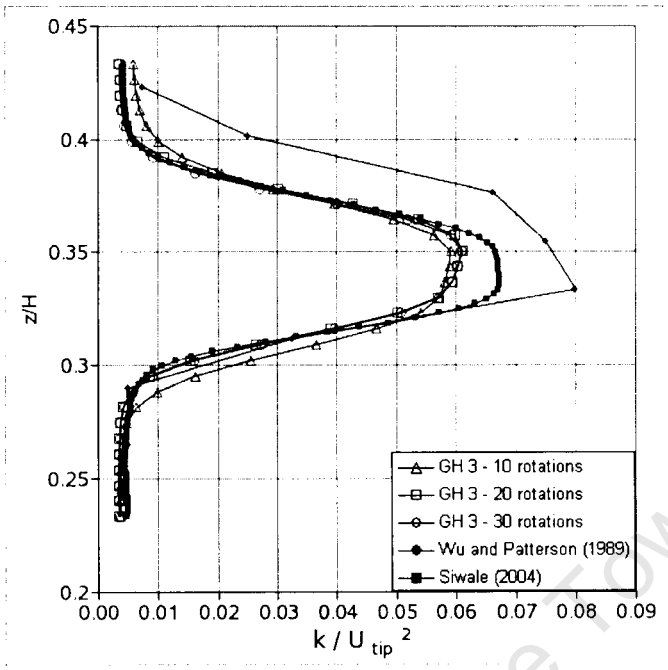

Figure 4.27: Axial profiles of normalized TKE velocity for GH 3 at r/T = 0.285

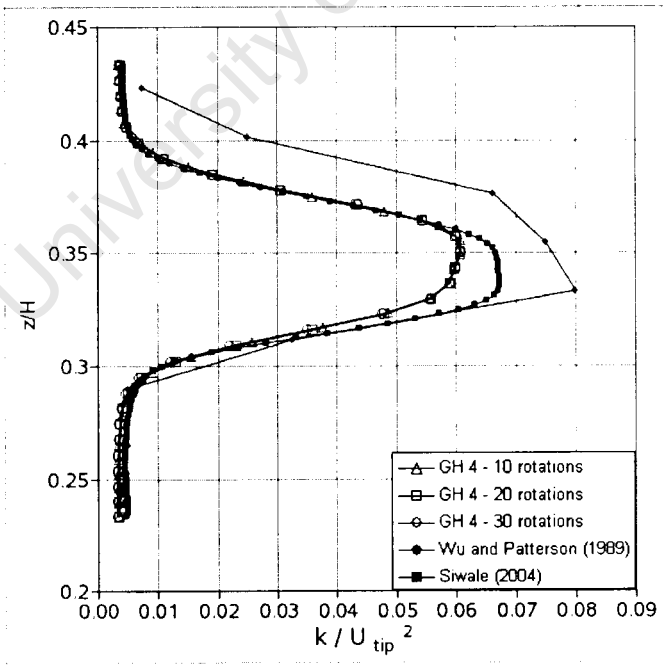

Figure 4.28: Axial profiles of normalized TKE velocity for GH 4 at r/T = 0.285

Turbulent kinetic energy profiles at r/T = 0.185 for the grids investigated are plotted in figure 4.29. Both model profiles (360 ° and 180 ° models) show good correlation with the profiles presented by Wu and Patterson (1989) and Siwale (2004), however the 180 ° model under predicts the profile presented by Siwale (2004). This can be attributed to the choice of discretisation scheme. First order upwind differencing was used for the MRF (180 °) model, while the higher order QUICK scheme was used for the sliding mesh grid (360 ° model). Turbulent kinetic energy profiles at r/T = 0.285 for the grids

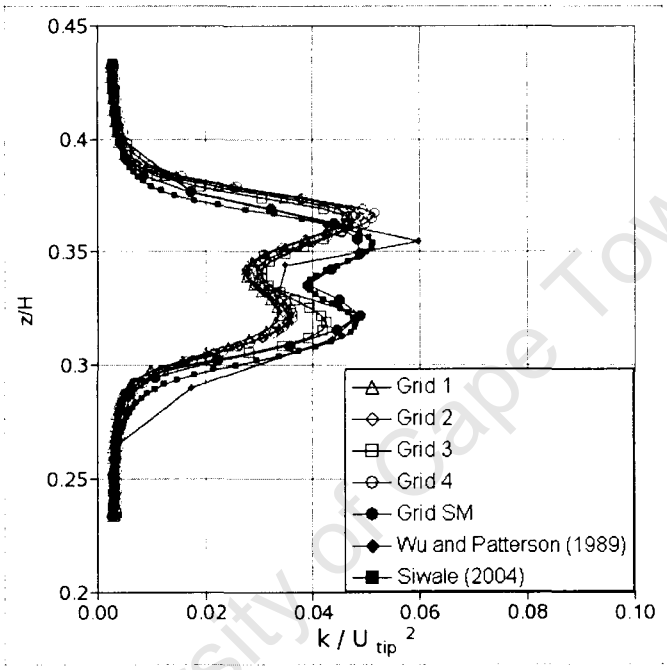

Figure 4.29: Axial profiles of normalized TKE at r/T = 0.185

investigated are plotted in figure 4.30. The profiles show good correlation with that of Siwale (2004).

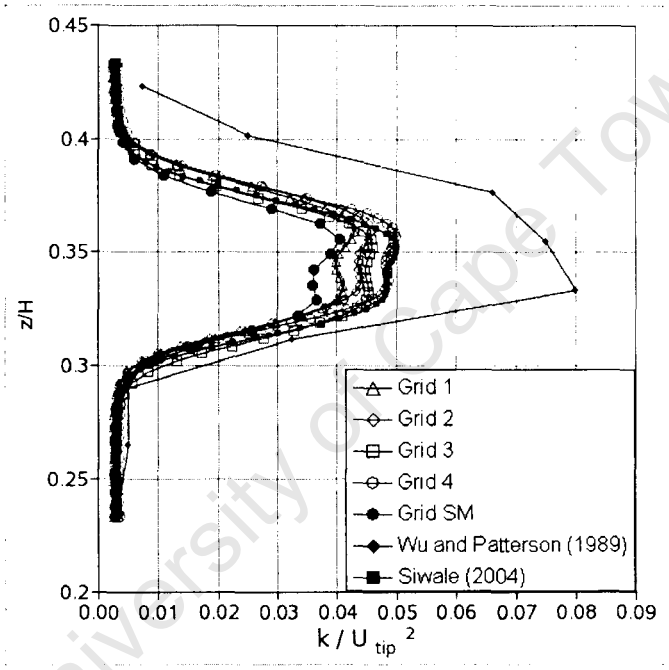

Figure 4.30: Axial profiles of normalized TKE at r/T = 0.285

4.2.2 Comparison with Deglon Data

Mean Tangential Velocity

The mean tangential velocity plots for the sliding mesh model are shown in figures 4.31 through 4.33 and are plotted at intervals of 10, 20 and 30 impeller rotations. The numerical data severely underpredicts the experimental data in the bulk tank (an observation also made for the single phase experimental data), especially starting from an initial gas hold up of GH 1. The reason for this is the same as for the single phase results, i.e., inaccuracies associated with the measurement technique used by Deglon (1998).

Correlation between the experimental and numerical data corresponding to initial concentrations of GH 2, GH 3 and GH 4 improves for the impeller stream, however, the data set corresponding to GH 1 significantly under predicts the experimental data.

Agreement for impeller tip mean tangential velocity for all initial gas hold up conditions is good.

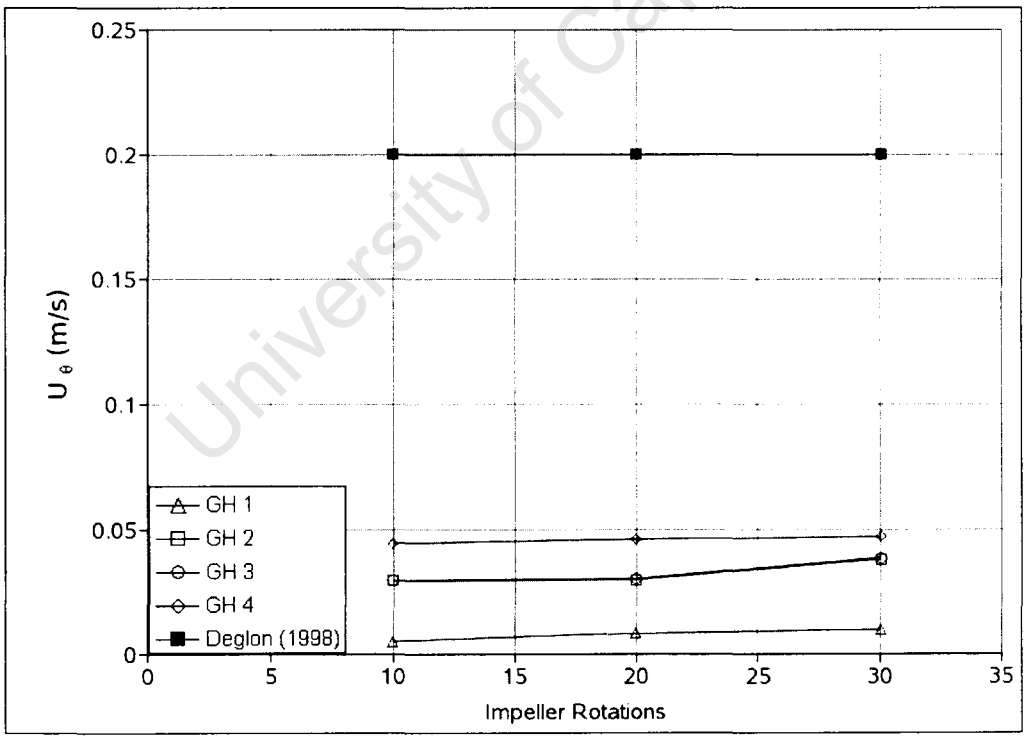

Figure 4.31: Mean tangential velocity vs impeller rotations for the bulk tank

The mean velocity for the MRF model is plotted in figures 4.34 through 4.36 for the 180 ° model as well as the 360 ° model, which constitutes the last data point for figures

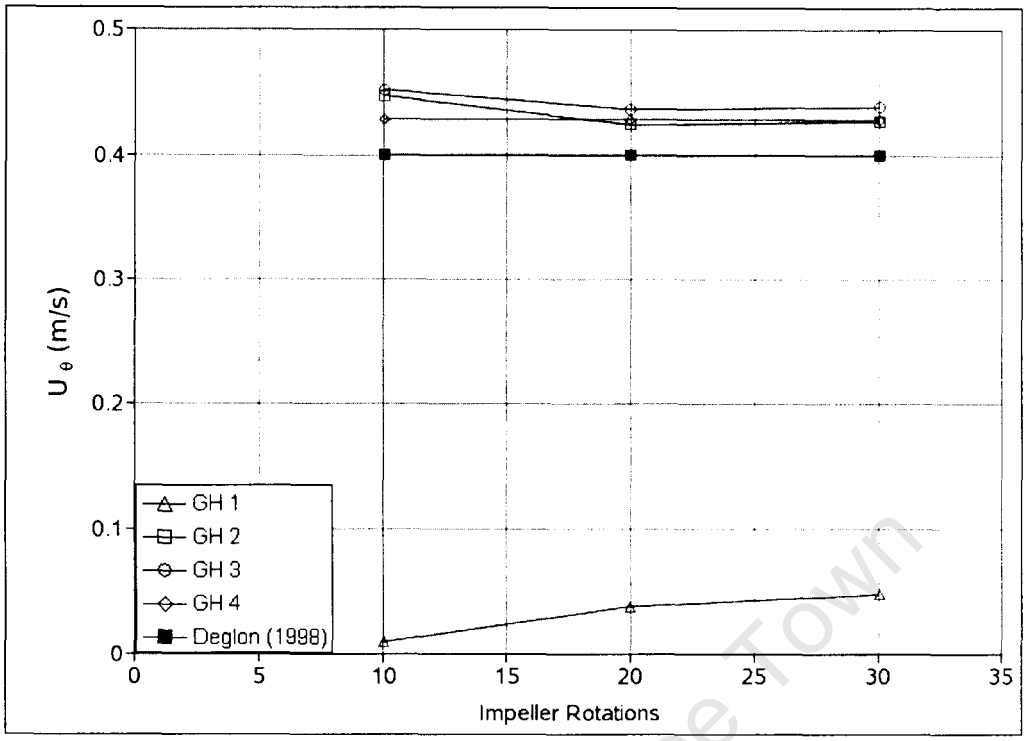

Figure 4.32: Mean tangential velocity vs impeller rotations for the impeller stream

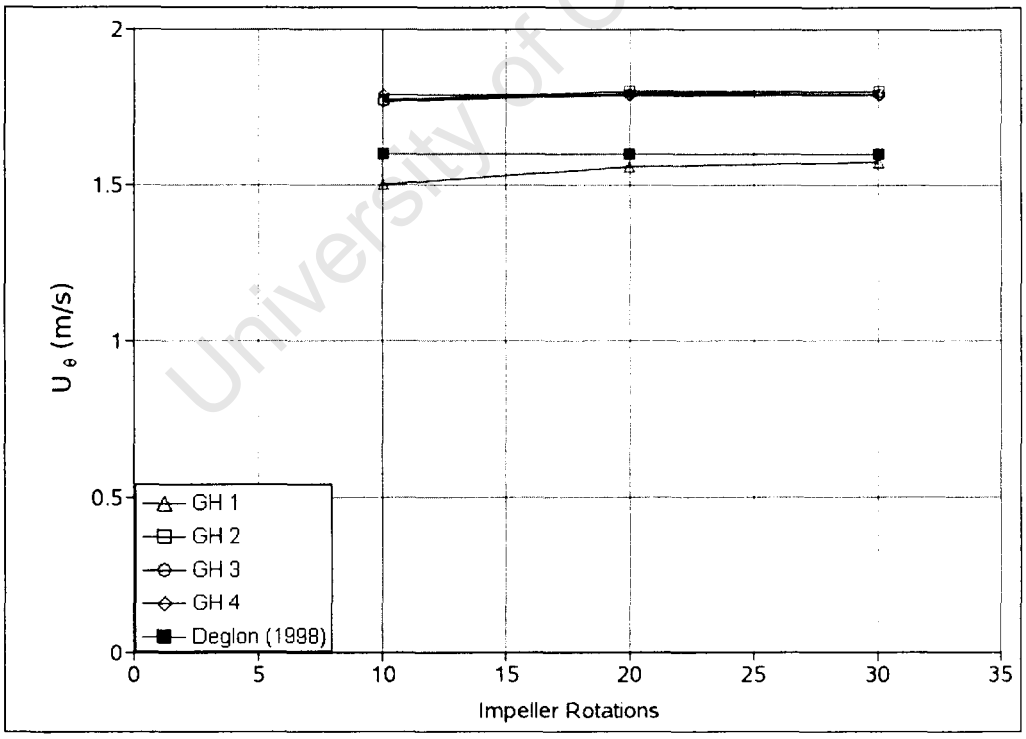

Figure 4.33: Mean tangential velocity vs impeller rotations at the impeller tip

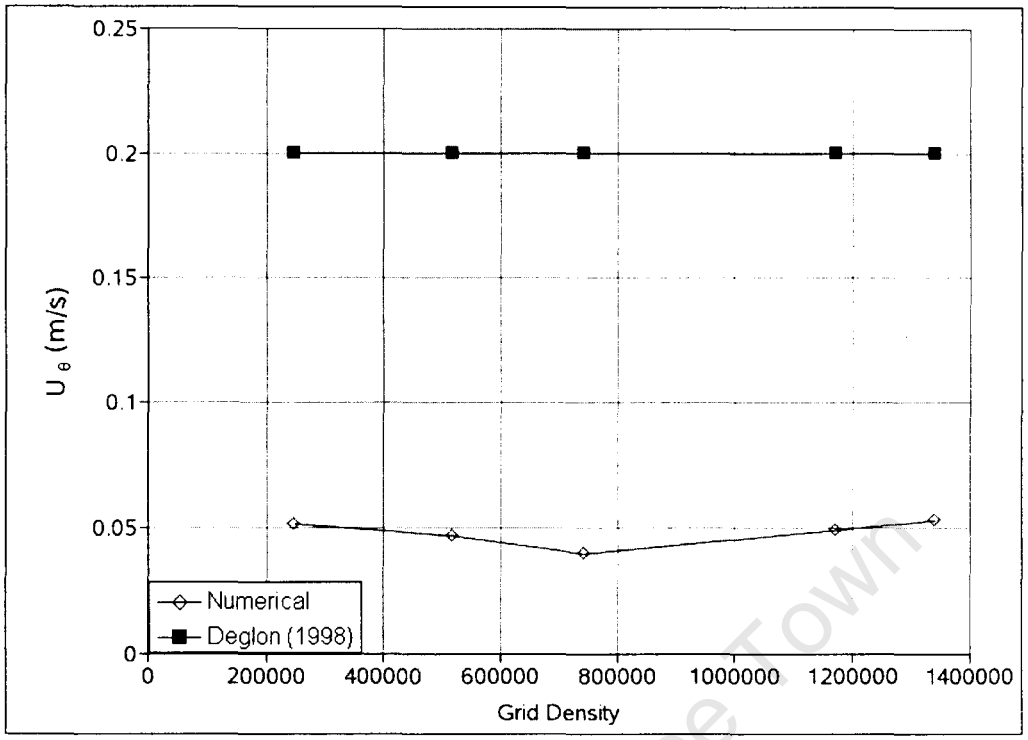

Figure 4.34: Mean tangential velocity vs grid density for the bulk tank

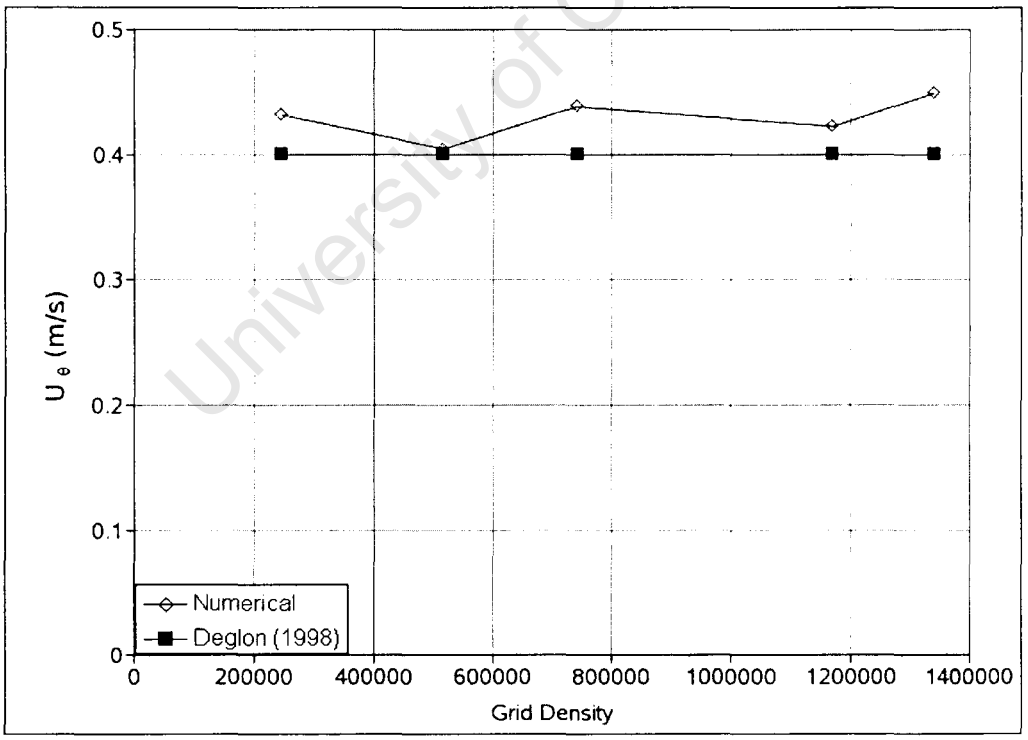

Figure 4.35: Mean tangential velocity vs grid density for the impeller stream

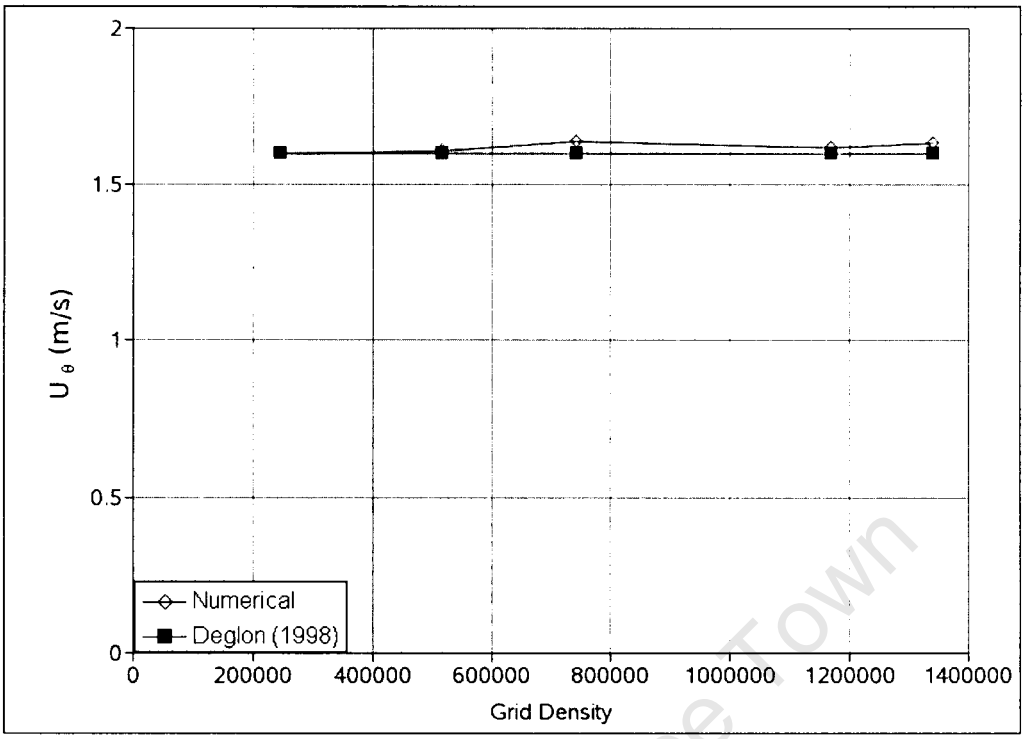

Figure 4.36: Mean tangential velocity vs grid density at the impeller tip

4.34 through 4.36. The trends are generally comparable with the data from sliding mesh model. The mean velocity in the bulk tank is severely under predicted. However, correlation between the experimental and numerical data is very good in the impeller stream and at the impeller tip.

Turbulent RMS Velocities

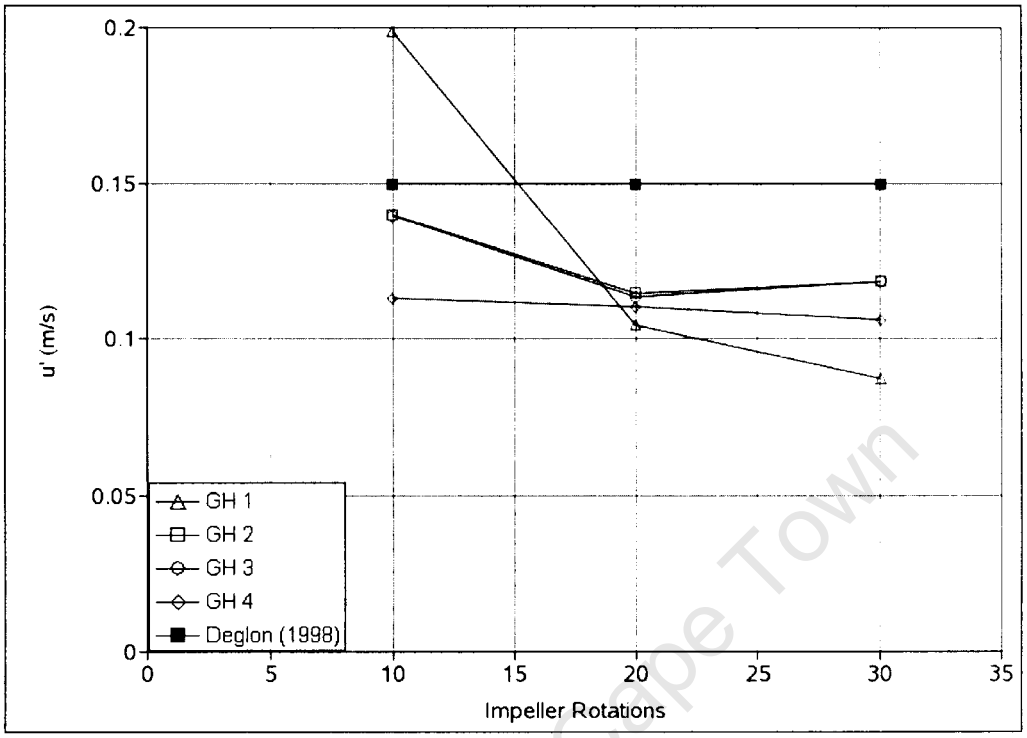

Figure 4.37: RMS velocity vs impeller rotations for the bulk tank

The RMS velocity plots for the sliding mesh model are shown in figures 4.37 through 4.39, at intervals of 10, 20 and 30 impeller rotations. The sliding mesh model predictions in the bulk tank and impeller stream are satisfactory for data corresponding to GH 2, GH 3 and GH 4. Predictions from all initial conditions are poor at the impeller tip. It is thought that the poor correlation is due to the use of different measurement techniques used in this study and that of Deglon (1998). This will be discussed in detail at the end of this chapter.

The RMS velocity data for the MRF model are plotted in figures 4.40 through 4.42. The numerical results are comparable with the sliding mesh data.

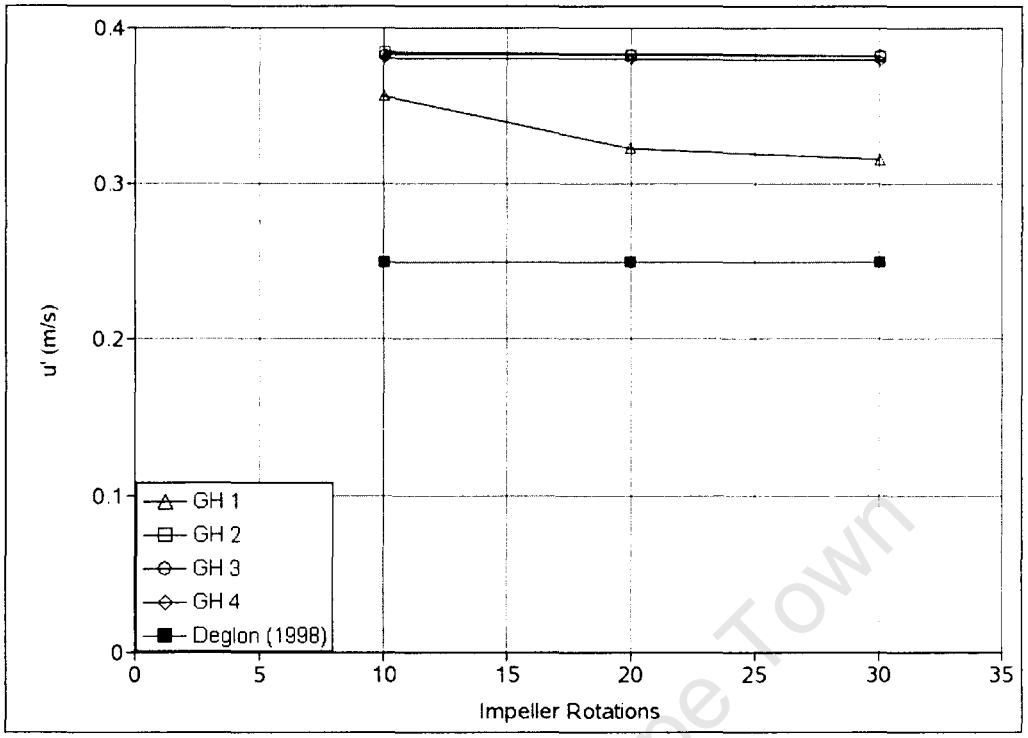

Figure 4.38: RMS velocity vs impeller rotations for the impeller stream

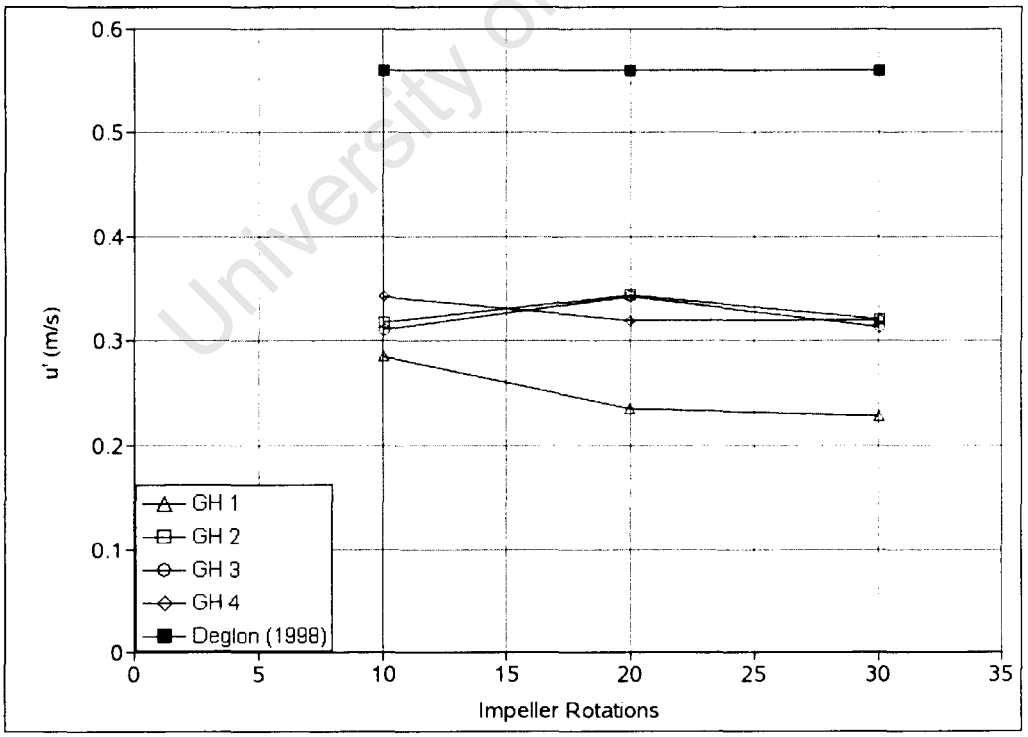

Figure 4.39: RMS velocity vs impeller rotations at the impeller tip

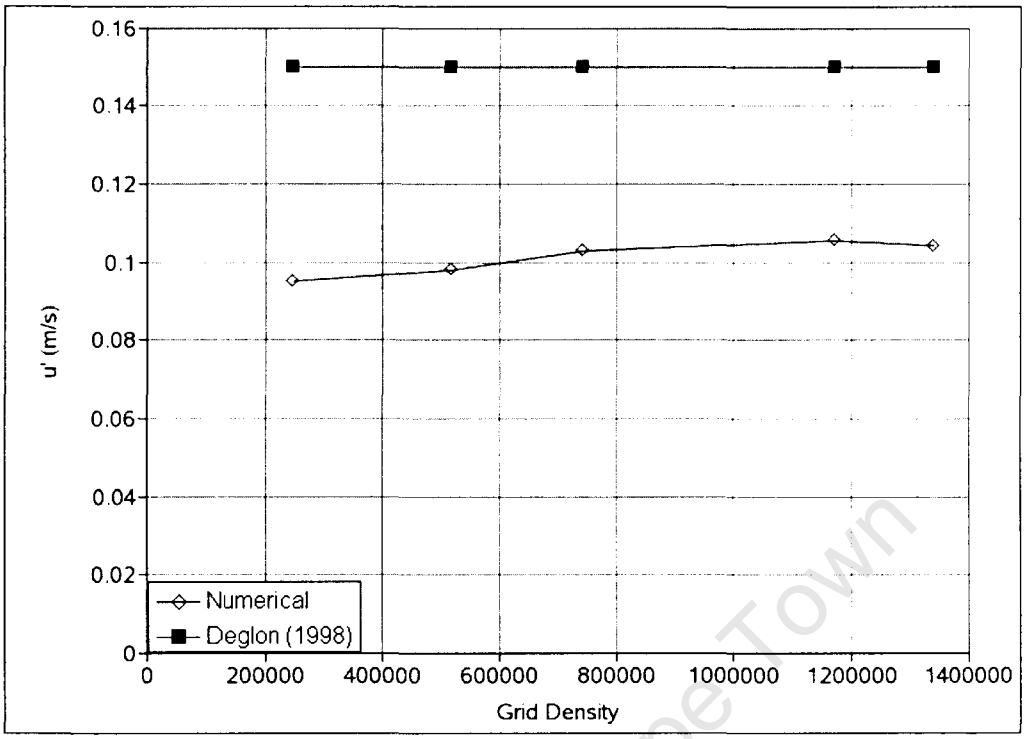

Figure 4.40: RMS velocity vs grid density for the bulk tank

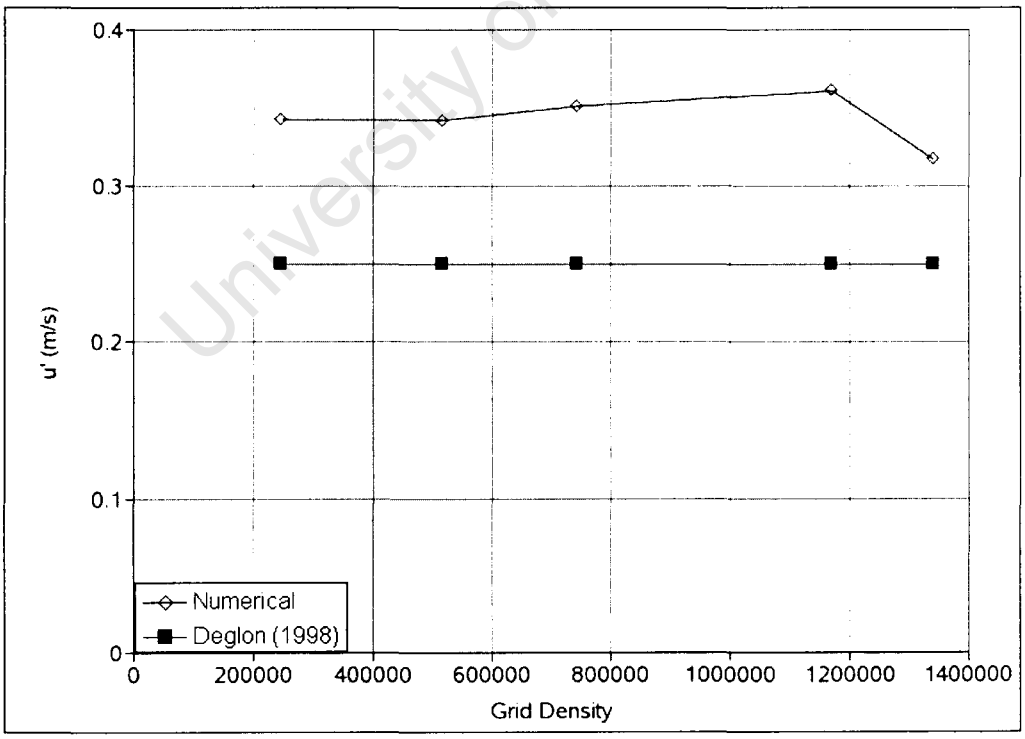

Figure 4.41: RMS velocity vs grid density for the impeller stream

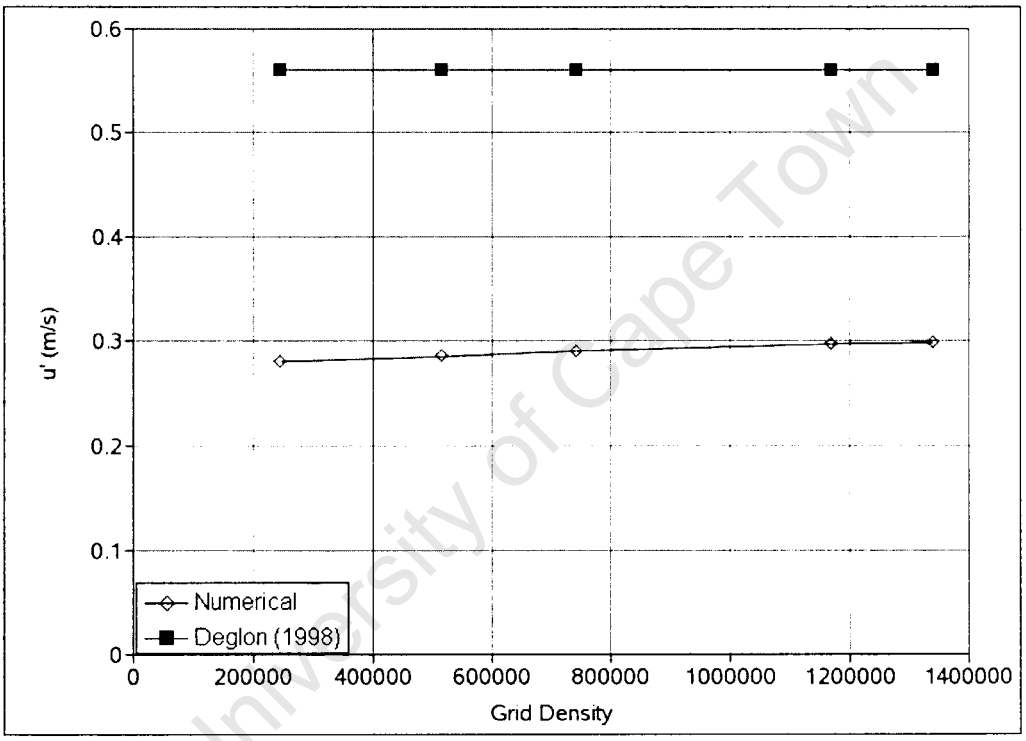

Figure 4.42: RMS velocity vs grid density at the impeller tip

Turbulent Dissipation Rate

The turbulent dissipation rate plots for the sliding mesh model are shown in figures 4.43 through 4.45, at intervals of 10, 20 and 30 impeller rotations. The sliding mesh model predictions in the impeller stream are good for simulations carried out at all initial gas hold up concentrations. Predictions at the impeller tip are poor for all initial conditions. The bulk tank data is poorly predicted for all starting conditions.

The turbulent dissipation rate plots for the MRF model are shown in figures 4.46 through 4.48. The trends are comparable to the sliding mesh model results. It should be noted that the 360 ° model (the last data point) poorly predicts the turbulent dissipation rate in the impeller stream and at the impeller tip. The reasons for this are unclear.

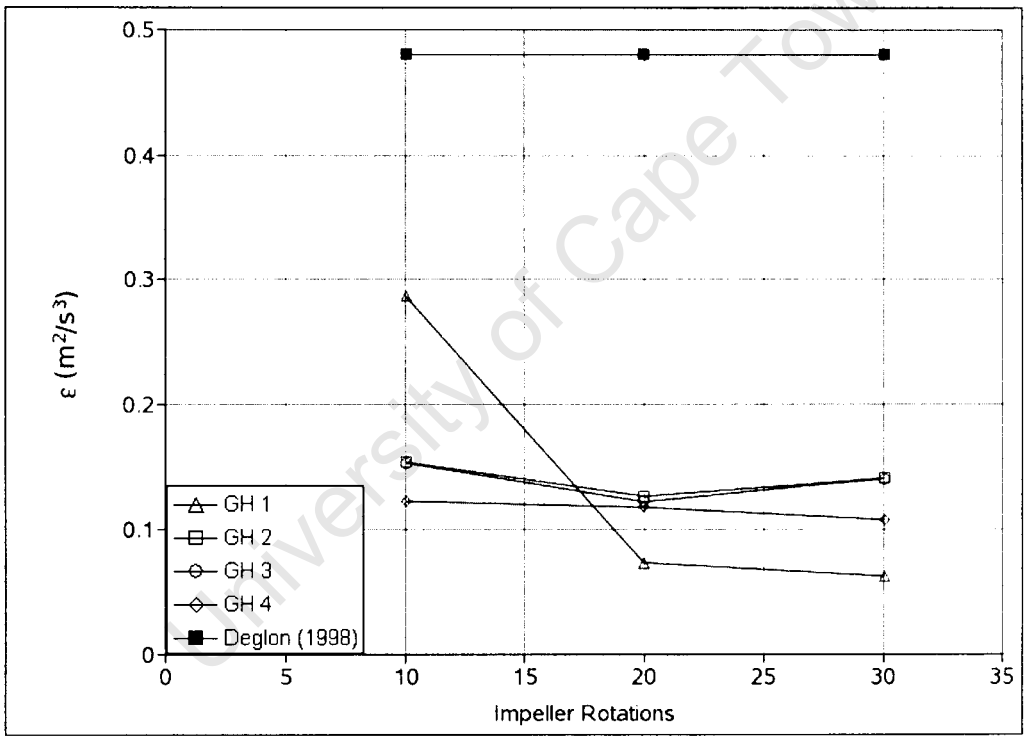

Figure 4.43: Turbulent dissipation rate vs impeller rotations for the bulk tank

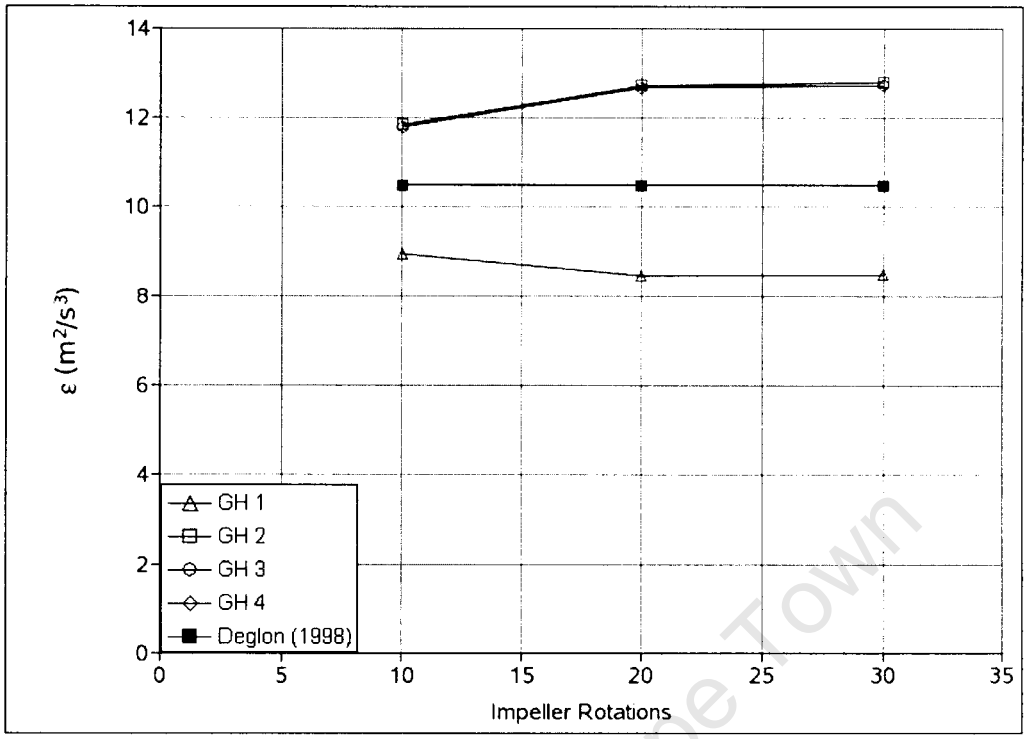

Figure 4.44: Turbulent dissipation rate vs impeller rotations for the impeller stream

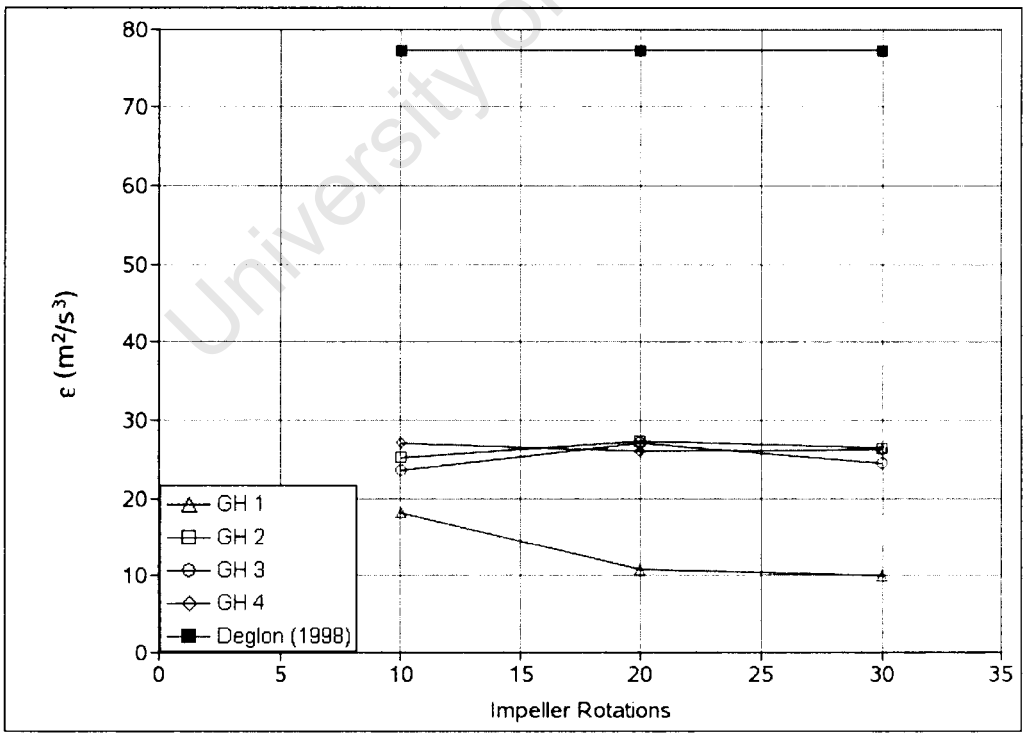

Figure 4.45: Turbulent dissipation rate vs impeller rotations at the impeller tip

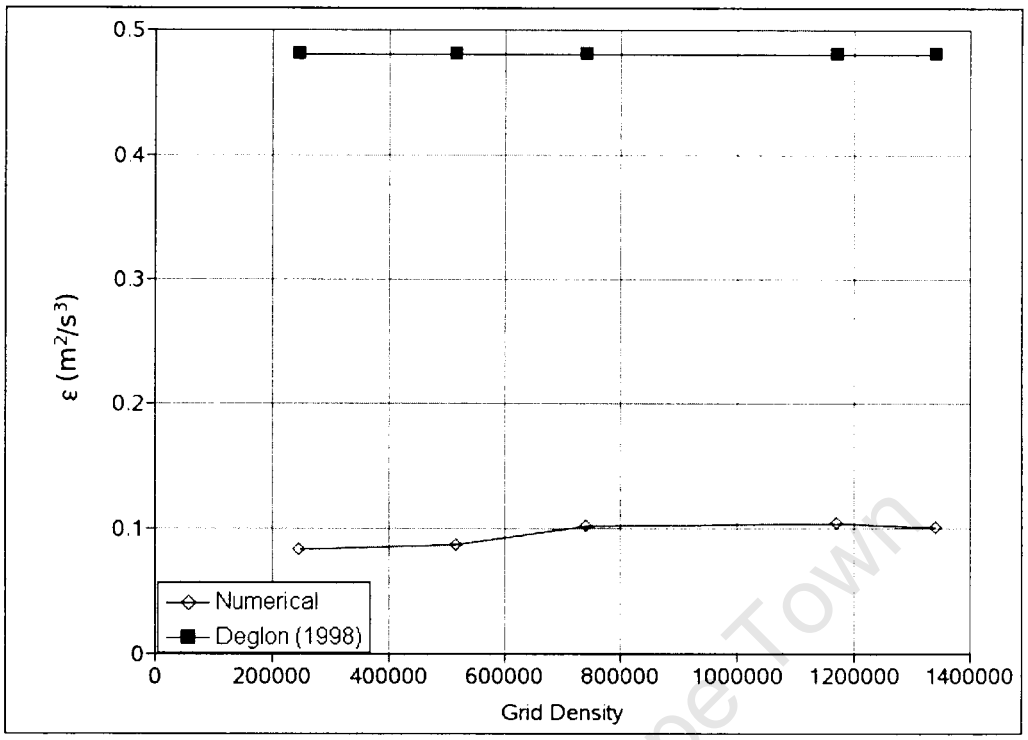

Figure 4.46: Turbulent dissipation rate vs grid density for the bulk tank

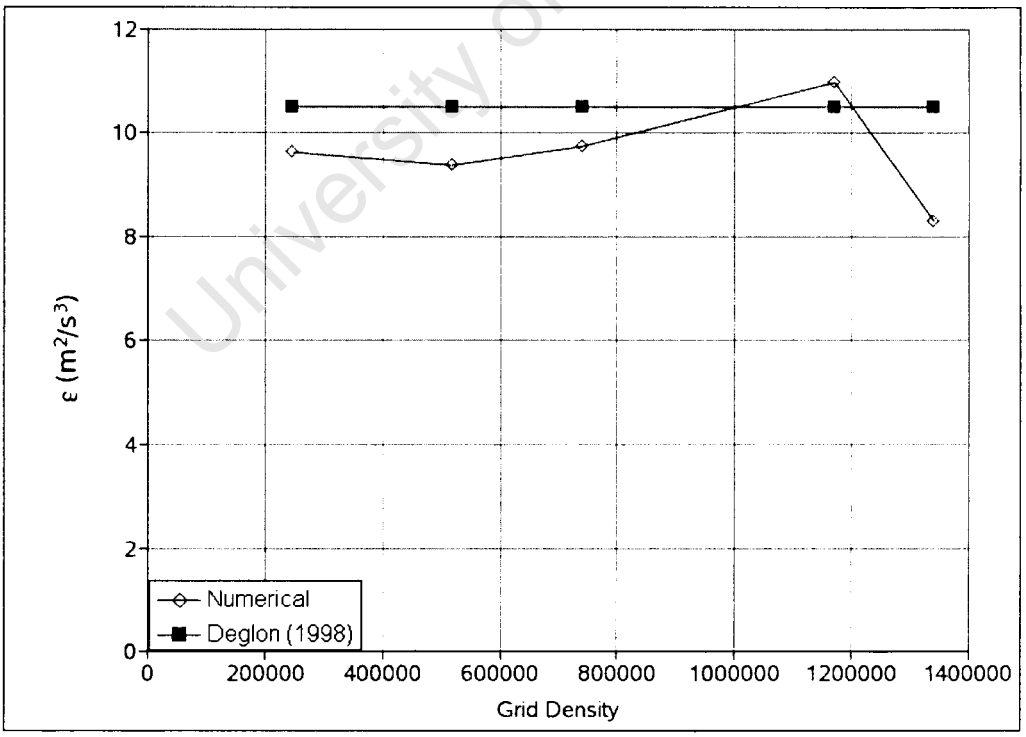

Figure 4.47: Turbulent dissipation rate vs grid density for the impeller stream

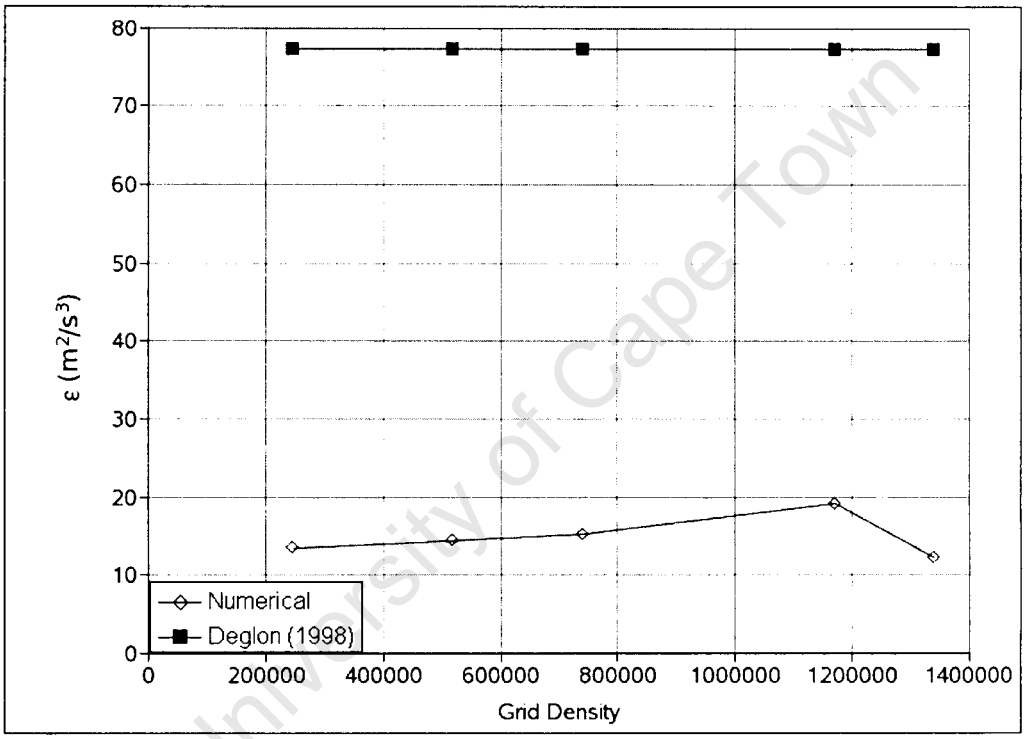

Figure 4.48: Turbulent dissipation rate vs grid density at the impeller tip

Power Draw

The influence of gas hold up on power draw for the sliding mesh model is evident in figure 4.49, where power draw is plotted for various initial gas hold up conditions. Power draw is resolved after 20 impeller rotations for all initial conditions. Predictions are good for all cases.

Power draw for the MRF model for various grid densities is plotted in figure 4.50. Predictions are good for all grid densities. This is expected for the same reasons outlined for the single phase power draw.

The difference between predicted power draw for the MRF and sliding mesh models can be attributed to the discretisation schemes used. First order upwind differencing was used for the MRF model, while the higher order QUICK scheme was used for the sliding mesh model.

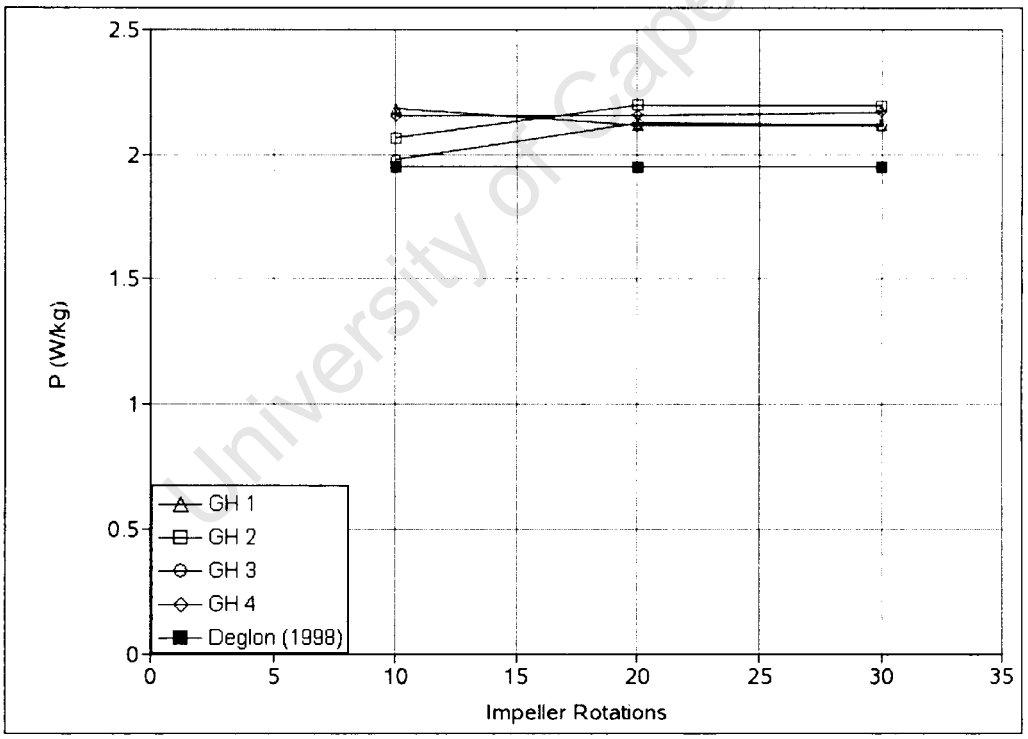

Figure 4.49: Comparison of varying initial gas hold up on power draw

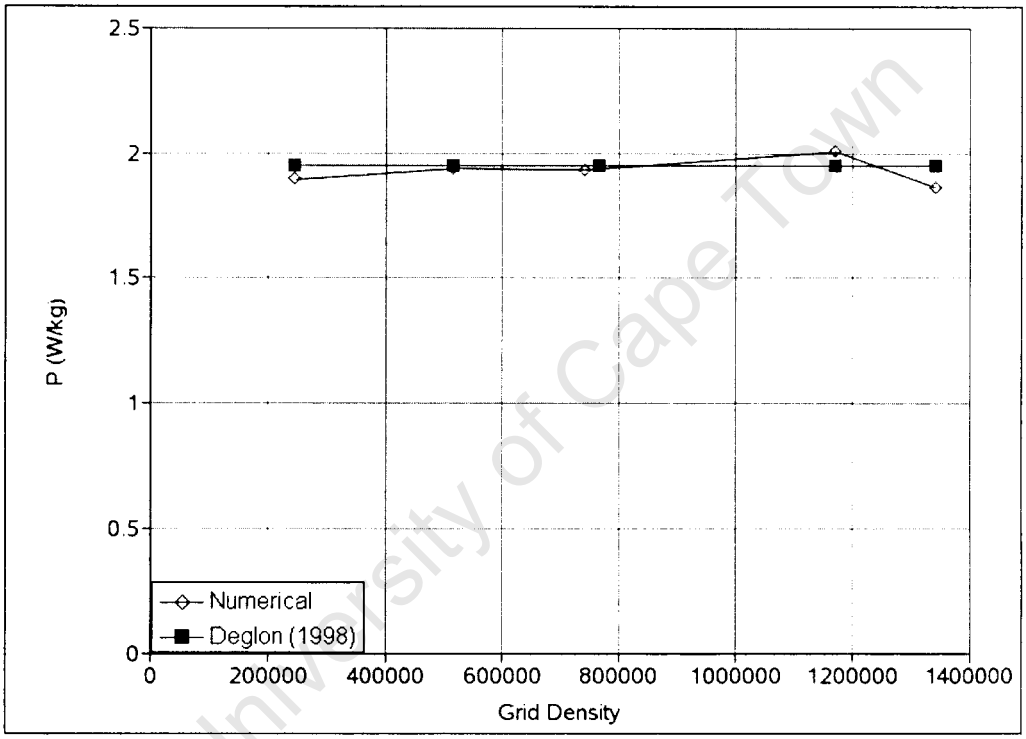

Figure 4.50: Comparison of Power draw for various grid densities

Gas Hold Up

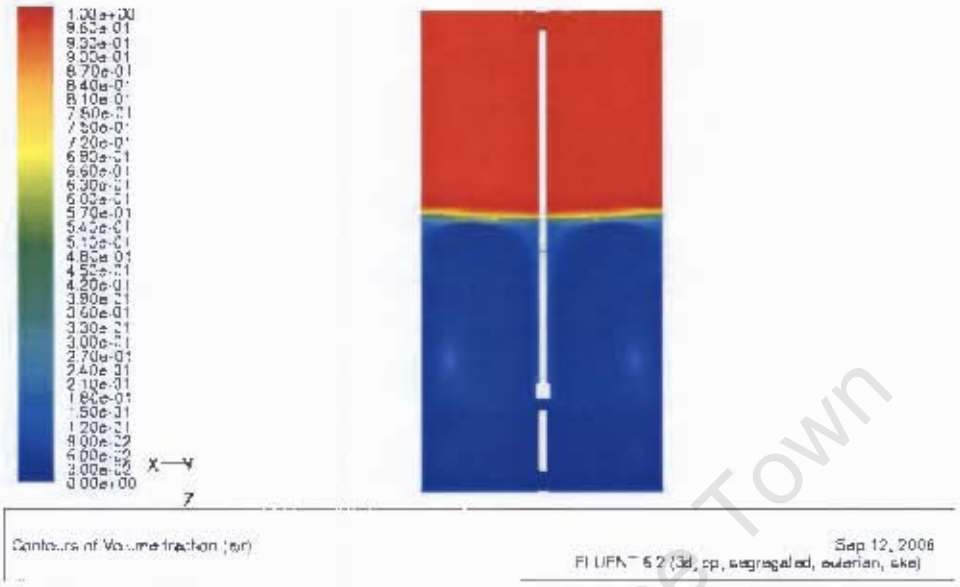

Figure 4.51: Contours of volume fraction in the stirred tank for the MRF model

Contours of volume fraction are shown in figures 4.51 and 4.52. for the MRF and sliding mesh models respectively. The flow field is consistent with the volume fraction flow patterns reported by Morud and Hjertager (1996) and Lane et al. (2002). It can be seen that the circulation zones, described by Morud and Hjertager (1996), formed above and below the impeller are more pronounced for the sliding mesh model (see figure 4.52). However, it should be noted that the higher order QUICK discretisation scheme was used for the sliding mesh model, while first order upwind differencing was used for the MRF model.

Gas hold up is plotted against impeller rotations for the sliding mesh model in figure 4.53. It should be noted that the experimental gas hold up is expected to be higher than the numerical value due to the presence of surfactants. It can be seen that the initial gas hold up makes a significant difference on the final gas hold up. The gas hold up steadily increases for initial concentrations of GH 2 and GH 3 and does not reach a steady state after 30 impeller rotations. However, gas hold up remains relatively constant for with increasing impeller rotations starting from initial concentrations of GH 1 and GH 4.

Gas hold up is plotted for the MRF model in figure 4.54. Gas hold up predictions

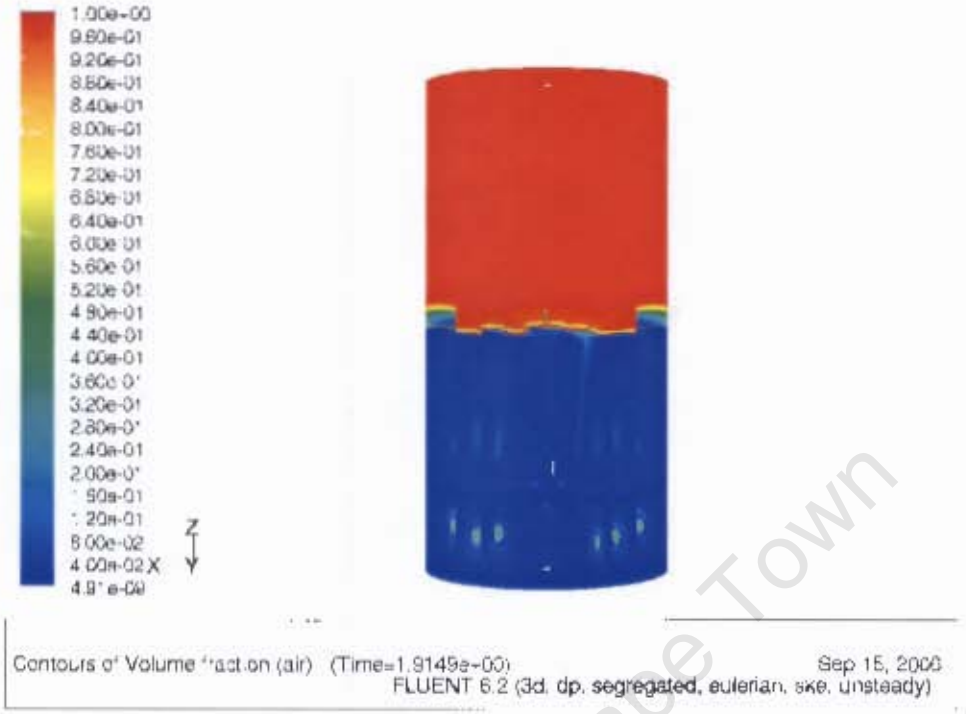

Figure 4.52: Contours of volume fraction in the stirred tank for the SM model

are not completely uniform for all grid densities, but all predictions are more or less within the 0.03 to 0.04 range. The numerical data again under predicts the experimental data, which is expected, in part due to the absence of surfactants in the numerical model.

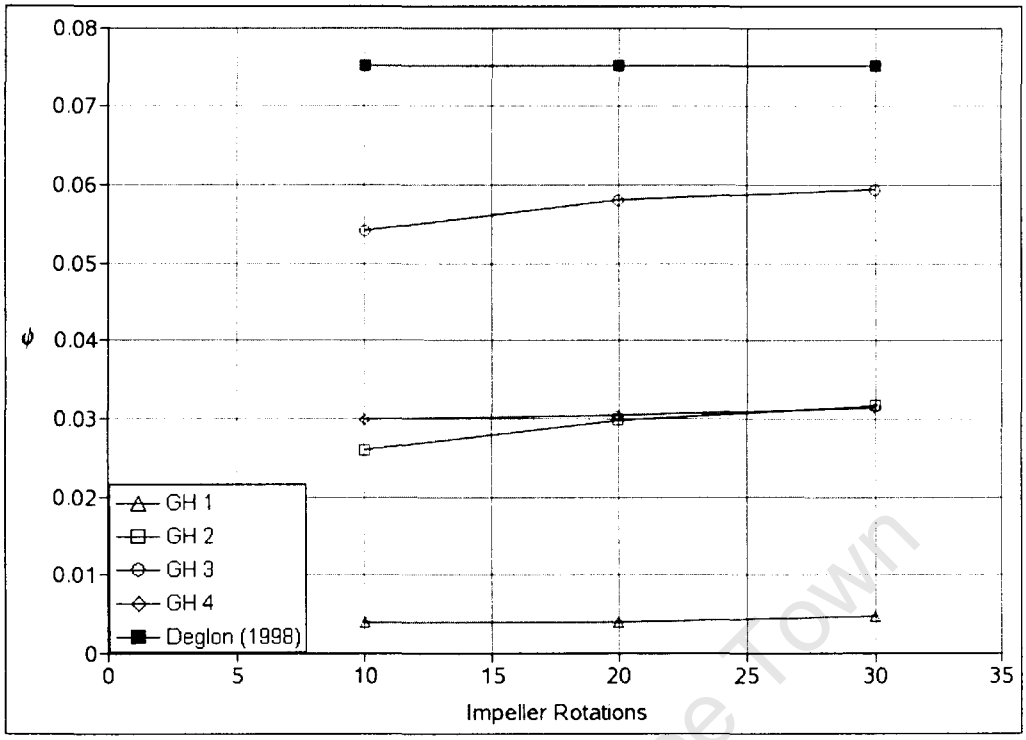

Figure 4.53: Comparison of varying initial Gas hold up

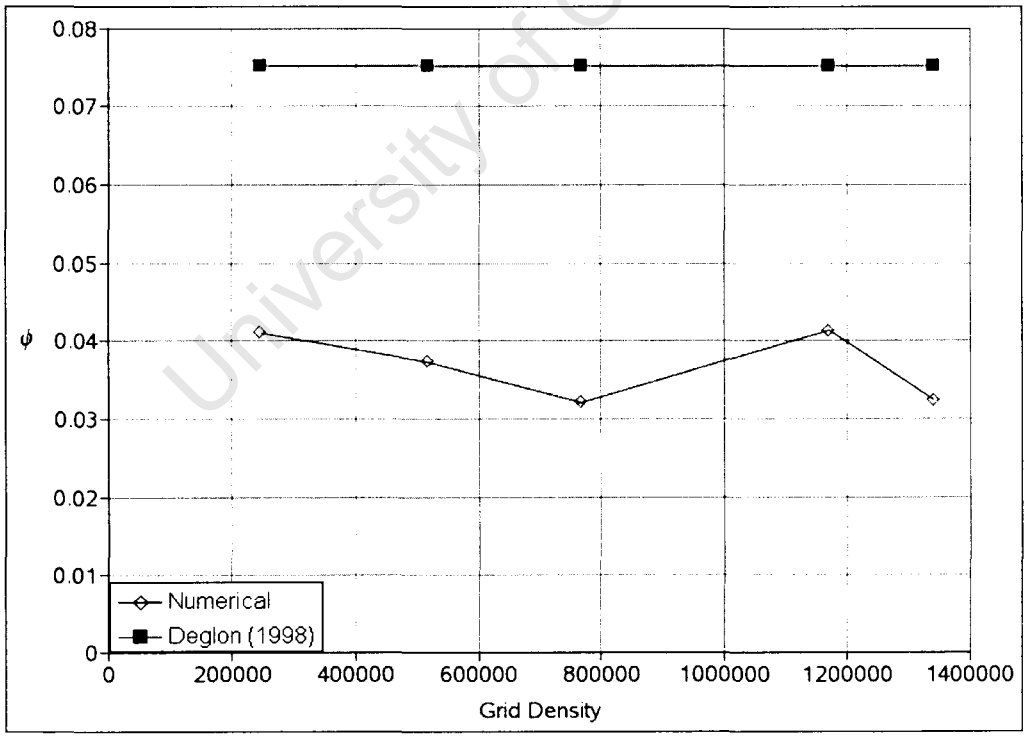

Figure 4.54: Comparison of Gas hold up for various grid densities

4.2.3 Comparison of Single Phase and Multiphase Data Trends

RMS velocity and turbulent dissipation rate trends were compared for the single and multiphase data, for this numerical study and the experimental study carried out by Deglon (1998), to determine the effect of gas on these parameters. In other words, it was of interest to find if the presence of gas increased or decreased these parameters.

Single phase and multiphase trends are compared for RMS velocity in table 4.2. Note that SP and MP indicate single phase and multiphase data respectively. Furthermore, data is presented for an impeller speed of 940 RPM. It can be seen that experimental and numerical trends are similar for the bulk tank and impeller stream, i.e., the presence of gas decreases the RMS velocity. This trend is repeated for the turbulent dissipation rate for the bulk tank and impeller stream as shown in table 4.3. However, at the impeller tip, the experimental data shows an increase in RMS velocity and turbulent dissipation rate, while the numerical data shows a decrease. Possible reasons for this are discussed at the end of this chapter.

Table 4.2: Turbulent RMS velocity (m/s) [940 RPM]

	Deglon (SP)	Deglon (MP)	Numerical (SP)	Numerical (MP)
Bulk tank	0.19	0.15	0.13	0.11
Impeller stream	0.38	0.25	0.42	0.38
Impeller tip	0.53	0.56	0.35	0.32

Table 4.3: Turbulent dissipation rate (m^2/s^3) [940 RPM]

	Deglon (SP)	Deglon (MP)	Numerical (SP)	Numerical (MP)
Bulk tank	0.83	0.48	0.20	0.11
Impeller stream	22.3	10.5	17.7	12.6
Impeller tip	58.8	77.3	46.6	26.2

4.3 Discussion

Single Phase Data

It was found that axial profiles of mean velocity and turbulent kinetic energy were accurately predicted by the single phase model.

Bulk tank data poorly predicted mean velocities, RMS velocities and turbulent dissipation rates presented by Deglon (1998). This can be attributed to the measurement probe used by Deglon (1998) to measure bulk tank parameters. The electrochemical probe used by the author did not take the flow directionality into account and the flow field in the bulk tank is not expected to be as strongly tangential as in the outflow of the impeller. Mean velocity predictions in the impeller stream and at the impeller tip were satisfactory and good respectively. RMS velocity predictions were good in the impeller stream, while satisfactory at the impeller tip. Turbulent dissipation rate predictions in the impeller stream and at the impeller tip were good.

Power draw predictions were accurate for the full range of impeller speeds. This result was expected as higher order discretisation was used for the numerical model and the experimental measurement technique was accurate.

Multiphase Data

Profiles of mean velocity started from all initial gas hold up concentrations showed good correlation with those presented by Wu and Patterson (1989) and Siwale (2004). However, it was noted that mean velocity profiles were under predicted by profiles corresponding to GH 1 and were inconsistent at 10, 20 and 30 impeller rotations. Furthermore, even though there was improved correlation with the Wu and Patterson (1989) and Siwale (2004) profiles for profiles corresponding to GH 2 and GH 3, there was still a lack of consistency with impeller rotations. No such inconsistencies were noted for mean velocity and turbulent kinetic energy profiles corresponding to GH 4. This finding suggests that the flow fields, resulting from simulations started at GH 1, GH 2 and GH 3 are not fully developed, even after 30 impeller rotations. Mean velocity and turbulent kinetic energy profiles predicted by the MRF model showed good correlation with the profiles presented by Wu and Patterson (1989) and Siwale (2004).

Bulk tank data was poorly predicted by both the MRF and sliding mesh models. Sim-

ilar poor correlation was observed for the single phase model and the reason for the poor correlation are the same here. Mean velocity predictions in the impeller stream and at the impeller tip were comparable for the impeller models, apart from predictions corresponding to GH 1. Predictions corresponding to GH 1 were for the most part inconsistent with predictions corresponding to other initial concentrations in all regions of the tank. This finding adds weight to the suggestion that the flow field is not fully developed for simulations corresponding to GH 1. Turbulent RMS velocities and turbulent dissipation rate predictions were satisfactory in the impeller stream, but poor at the impeller tip for both impeller models. This poor correlation can be attributed to the use of different measurement techniques in this study and the one carried out by Deglon (1998). Deglon (1998) used the energy spectrum to determine the RMS velocity from the following equation

$$\overline{u}^2 = \int_0^\infty E_1(n)dn \tag{4.1}$$

Where $E_1(n)$ is the energy spectrum function and n is the frequency. However, the RMS velocity in this study was calculated using equation 2.18, such that the RMS turbulent velocity was given by

$$\overline{u}^2 = \frac{2}{3}k \tag{4.2}$$

Furthermore, turbulence measurements for this study were sampled at the impeller tip in regions unaffected by the periodic component of turbulence, i.e., outside of the trailing vortices behind the impeller blades. It is possible that the periodic component of turbulence was not entirely removed in the data presented by Deglon (1998). For this reason, it is thought that the data presented by Deglon (1998) might contain a significant periodic component, which could be the difference between the turbulence parameter measurements for the two data sets.

Power draw predictions were unaffected by gas hold up and predictions were good for both impeller models. This result was expected as higher order discretisation was used for the numerical model and the experimental measurement technique was accurate.

Gas hold up was found to be dependent on the initial gas hold up. For initial concentrations of GH 2 and GH 3, gas hold up was found to steadily increase even after 30 impeller rotations. However, gas hold up was almost constant after 30 impeller rotations after starting from initial concentrations of GH 1 and GH 4. The trend for the former can be attributed to the fact that the flow field is not yet fully developed after 30 impeller rotations, while the trend for the latter can be attributed to the flow field having

reached a "steady-state", i.e., being fully developed. Simulations carried out from all initial concentrations under predict the experimental gas hold up reported by Deglon (1998). This is due to the absence of surfactants in the numerical model.

Chapter 5

Conclusions and Recommendations

The purpose of this study was to develop a multiphase model for a Rushton turbine-agitated stirred tank. The MRF model was used for single phase flow simulations while the sliding mesh and MRF impeller models were used to simulate multiphase flow. The models were evaluated in terms of mean velocities and turbulence parameters and power draw, as well as gas hold up for the multiphase model. Single phase data was validated using experimental data published by Wu and Patterson (1989) and numerical data presented by Siwale (2004). Multiphase data was primarily validated using data published by Deglon (1998) and also compared to the data presented by Wu and Patterson (1989) and Siwale (2004). From the results, the following conclusions can be drawn.

5.1 Conclusions

5.1.1 Single Phase Model

Axial profiles of mean velocity and turbulent kinetic energy accurately predicted the profiles presented by Wu and Patterson (1989) and Siwale (2004).

Bulk tank data poorly predicted mean velocities, RMS velocities and turbulent dissipation rates presented by Deglon (1998). This was attributed to the measurement probe used by Deglon (1998) to measure bulk tank parameters. Mean velocity predictions in the impeller stream and at the impeller tip were satisfactory and good respectively. RMS velocity predictions were good in the impeller stream, while satisfactory at the impeller tip. Turbulent dissipation rate predictions in the impeller stream and at the impeller tip were good.

Power draw predictions were accurate for the full range of impeller speeds. This result was expected as higher order discretisation was used for the numerical model and the experimental measurement technique was accurate.

It was therefore concluded that the single phase model can predict the single phase experimental data with reasonable (in the case of the data presented by Deglon (1998)) to good (in the case of the data presented by Wu and Patterson (1989) and Siwale (2004)) accuracy.

5.1.2 Multiphase Model

Axial profiles of mean velocity and turbulent kinetic energy corresponding to the MRF and sliding mesh models, showed good correlation with the profiles presented by Wu and Patterson (1989) and Siwale (2004). Only profiles corresponding to GH 1 were notably inconsistent with profiles corresponding to other initial concentrations. It is concluded that the inconsistency is as a result of the flow field being under developed.

Furthermore, upon inspection of turbulent kinetic energy profiles resulting from initial gas hold up concentrations of GH 1, GH 2, GH 3 and GH 4, it can be concluded that patching initial values of gas hold up into the stirred tank does not produce a fully developed flow field, even after 30 impeller rotations. Using the solution from an MRF simulation as the iniitial condition for the sliding mesh model produced the most consistent results.

5.2 Recommendations

From the conclusions drawn, it was evident that MRF model produces reasonable results for a low computational cost, compared to the sliding mesh model. However, the MRF model did not converge to the required convergence criterion after 30 impeller rotations. Therefore, even though the MRF model produced satisfactory results, it is recommended that it should not be used to model multiphase flow in a stirred tank. However, the use of an MRF solution as an input for the sliding mesh model produced consistent results for 10, 20 and 30 impeller rotations. It is therefore recommended that the solution to an MRF simulation be used as the initial condition for the sliding mesh model.

References

Abujelala, M. and Lilley, D.: 1984, Limitations and empirical extensions of the k-ϵ model as applied to turbulent confined swirling flows, *Chemical Engineering Communications* **31**, 223–236.

Aubin, J., Fletcher, D. and Xuereb, C.: 2004, Modeling turbulent flow in stirred tanks with CFD: the influence of the modeling approach, turbulence model and numerical scheme, *Experimental Thermal and Fluid Science* **28**, 431–445.

Bakker, A.: 1992, *Hydrodynamics of Stirred Gas-Liquid Dispersions*, PhD thesis, Delft University of Technology, The Netherlands.

Bartels, C., Breuer, M., Wechsler, K. and Durst, F.: 2002, Computational fluid dynamics applications on parallel-vector computers: computations of stirred vessel flows, *Computers and Fluids* **31**, 69–97.

Brucato, A., Ciofalo, M., Grisafi, F. and Micale, G.: 1998, Numerical prediction of flow fields in baffled stirred vessels: A comparison of alternative modeling approaches, *Chemical Engineering Science* **53**, 3653–3684.

Campolo, M., Sbrizzai, F. and Soldati, A.: 2003, Time-dependent flow structure and lagrangian mixing in rushton impeller baffled-tank reactor, *Chemical Engineering Science* **58**, 1615–1629.

Costes, J. and Couderc, J.: 1988, Study by laser doppler anemometry of the turbulent flow induced by a rushton turbine in a stirred tank: Influence of the size if the units - i. mean flow and turbulence, *Chemical Engineering Science* **43**, 2751–2764.

Cutter, L.: 1966, Flow and turbulence in a stirred tank, *American Institution of Chemical Engineers Journal* **12**, 35–45.

Deen, N., Solberg, T. and Hjertager, B.: 2002, Flow generated by an aerated Rushton impeller: Two phase PIV experiments and numerical simulations, *Canadian Journal of Chemical Engineering* **80**, 638–652.

Deglon, D.: 1998, *A Hydrodynamic investigation of fine particle flotation in a batch flotation cell*, PhD thesis, University of Cape Town, South Africa.

Deglon, D. and Meyer, C.: 2006, CFD Modeling of Stirred Tanks: Numerical Considerations, *Minerals Engineering* **19**, 1059–1068.

Derksen, J. and van den Akker, H.: 1999, Large Eddy Simulations on the flow driven by a rushton turbine, *American Institution of Chemical Engineers Journal* **45**, 209–221.

Deshpande, V. and Ranade, V.: 2003, Simulation of flows in stirred vessels agitated by dual rushton impellers using computational snapshot approach, *Chemical Engineering Communications* **190**, 236–253.

Dyster, K., Koutsakos, E., Jaworski, Z. and Nienow, A.: 1993, An LDA study of the radial discharge velocities generated by a rusthon turbine: Newtonian fluids, $Re \geq 5$, *Transactions of the Institution of Chemical Engineers* **71**, 11–23.

Eggels, J.: 1996, Direct and Large Eddy Simulation of turbulent flow using the Lattice-Boltzmann scheme, *International Journal of Heat and Fluid Flow* **17**, 307–323.

FLUENT: 2005, *Users Guide*, 6.2 edn, Fluent Inc, Centerra Resource Park, 10 Cavendish Court, Lebanon, NH 03766.

Fokema, M., Kresta, S. and Wood, P.: 1994, Importance of using the correct impeller boundary conditions for CFD simulations of stirred tanks, *The Canadian Journal of Chemical Engineering* **72**, 177–183.

Gentric, C., Mignon, D., Bousquet, J. and Tanguy, P.: 2005, Comparison of mixing in two industrial gas-liquid reactors using CFD simulations, *Chemical Engineering Science* **60**, 2253–2272.

Gosman, A., Lekakou, C., Politis, S., Issa, R. and Looney, M.: 1992, Multidimensional modeling of turbulent two-phase flows in stirred vessels, *American Institution of Chemical Engineers Journal* **38**, 1946–1956.

Günkel, A. and Weber, M.: 1975, Flow phenomena in stirred tanks-part1. the impeller stream, *American Institution of Chemical Engineers Journal* **21**, 931–949.

Han, T., Humphrey, J. and Launder, B.: 1981, A comparison of hybrid and quadratic-upstream differencing in high reynolds number elliptic flows, *Computer Methods in Applied Mechanics and Engineering* **29**, 81–95.

Hartmann, H., Derksen, J. and van den Akker, H.: 2004, Assessment of Large Eddy and RANS stirred tank simulations by means of LDA, *Chemical Engineering Science* **59**, 2419–2432.

Harvey, A., Lee, C. and Rogers, S.: 1995, Steady-state modeling and experimental measurement of a baffled impeller stirred tank, *American Institute of Chemical Engineers Journal* **41**, 2177–2186.

Jenne, M. and Reuss, M.: 1999, A critical assessment on the use of the k-ϵ turbulence model for simulation of the turbulent liquid flow induced by a rushton-turbine in a baffled stirred-tank reactor, *Chemical Engineering Science* **54**, 3921–3941.

Kerdouss, F., Bannari, A. and Proulx, P.: 2006, CFD modeling of gas dispersion and bubblse size in a turbine stirred tank, *Chemical Engineering Science* **61**, 3313–3322.

Khopkar, A., Rammohan, A., Ranade, V. and Dudukovic, M.: 2005, Gas liquid flow generated by a rushton turbine in a stirred vessel: CARPT/CT measurements and CFD simulations, *Chemical Engineering Science* **60**, 2215–2229.

Koh, P., Manickam, M. and Schwarz, M.: 2000, CFD simulation of bubble-particle collisions in mineral flotation cells, *Minerals Engineering* **13**, 1455–1463.

Koh, P. and Schwarz, M.: 2003, CFD modeling of bubble-particle collision rates and efficiencies in a flotation cell, *Minerals Engineering* **16**, 1055–1059.

Kresta, S. and Wood, P.: 1991, Prediction of three-dimensional turbulent flow in stirred tanks, *American Institution of Chemical Engineers Journal* **37**, 448–460.

Lane, G., Schwarz, M. and Evans, G.: 2002, Predicting gas-liquid flow in a mechanically stirred tank, *Applied Mathematical Modelling* **26**, 223–235.

Launder, B. and Spalding, D.: 1974, The numerical computation of turbulent flows, *Computer Methods in Applied Mechanics and Engineering* **3**, 269–289.

Luo, J., Gosman, A., Issa, R., Middleton, J. and Fitzgerald, M.: 1993, Full flow field computation of mixing in baffled stirred vessels, *Transactions of the Institution of Chemical Engineers* **71**, 342–344.

Marshall, E. and Bakker, A.: 2003, *Computational Fluid Mixing*, John Wiley and Sons.

Montante, G., Lee, K., Brucato, A. and Yianneskis, M.: 2001, Experiments and predictions of the transition of the flow pattern with impeller clearance in stirred tanks, *Computers and Chemical Engineering* **25**, 729–735.

Morud, K. and Hjertager, B.: 1996, LDA measurements and CFD modeling of gas-liquid flow in a stirred vessel, *Chemical Engineering Science* **51**, 233–249.

Ng, K., Fentiman, K., Lee, K. and Yianneskis, M.: 1998, Assessment of sliding mesh CFD predictions and LDA measurements of flow in a tank stirred by a Rushton impeller, *Transactions of the Institute of Chemical Engineers* **76**, 737–747.

Ranade, V.: 1997, An efficient computational model for simulating flow in stirred vessels, *Chemical Engineering Science* **52**, 4473–4484.

Ranade, V. and Deshpande, V.: 1999, Gas-liquid flow in stirred reactors: Trailing vortices and gas accumulation behind impeller blades, *Chemical Engineering Science* **54**, 2305–2315.

Ranade, V., Joshi, J. and Marathe, A.: 1989, Flow generated by pitched blade turbines II: Simulation using the k-ϵ model, *Chemical Engineering Communications* **81**, 225–248.

Ranade, V., Perrard, M., Sauze, N. L., Xuereb, C. and Bertrand, J.: 2001, Trailing vortices of Rushton turbine: PIV measurements and CFD simulations with snapshot approach, *Transactions of the Institute of Chemical Engineers* **79**, 3–12.

Ranade, V. and van den H.E.A. Akker: 1994, A computational snapshot of gas-liquid flow in baffled stirred reactors, *Chemical Engineering Science* **49**, 5175–5192.

Rigopoulos, S. and Jones, A.: 2003, A hybrid CFD-reaction engineering framework for multiphase reactor modeling: basic concept and application to bubble column reactors, *Chemical Engineering Science* **58**, 3077–3089.

Rushton, J., Costich, E. and Everett, H.: 1950, Power characteristics of mixing impellers - Part 1, *Chemical Engineering Progress* **46**, 395–404.

Schiller, L. and Naumann, A.: 1933, Über die grundlegenden berechnungen bei der schwerkraftaufbereitung, *Zeitschrift Des Vereines Deutscher Ingenieure* **77**, 318–320.

Siwale, N.: 2004, *Modeling of flow in impeller stirred tanks using computational fluid dynamics*, Master's thesis, University of Cape Town, South Africa.

Spicka, P., Dias, M. and Lopes, J.: 2001, Gas-liquid flow in a 2D column: Comparison between experimental data and CFD modeling, *Chemical Engineering Science* **56**, 6367–6383.

Sun, H., Mao, Z. and Yu, G.: 2006, Experimental and numerical study of gas hold-up in surface aerated stirred tanks, *Chemical Engineering Science* **61**, 4098–4110.

Tabor, G., Gosman, A. and Issa, R.: 1996, Numerical simulation of the flow in a mixing vessel stirred by a rushton turbine, *IChemE Symposium Series*, number 140, pp. 25–34.

van der Molen, K. and van Maanen, H.: 1978, Laser-doppler measurements of the turbulent flow in stirred vessels to establish scaling rules, *Chemical Engineering Science* **33**, 1161–1168.

van't Riet, K. and Smith, J.: 1973, The behaviour of gas-liquid mixtures near Rushton turbine blades, *Chemical Engineering Science* **28**, 1031–1037.

van't Riet, K. and Smith, J.: 1975, The trailing vortex system produced by rushton turbine agitators, *Chemical Engineering Science* **30**, 1093–1105.

Versteeg, H. and Malalasekera, W.: 1995, *An Introduction to Computational Fluid Dynamics - The Finite Volume Method*, Prentice Hall.

Wechsler, K., Breuer, M. and Durst, F.: 1999, Steady and unsteady computations of turbulent flows induced by a 4/45° pitched-blade impeller, *Journal of Fluids Engineering* **121**, 318–329.

Wu, H. and Patterson, G.: 1989, Laser doppler measurements of turbulent-flow parameters in a stirred mixer, *Chemical Engineering Science* **44**, 2207–2221.

Wu, H., Patterson, G. and van Doorn, M.: 1989, Distribution of turbulence energy dissipation rates in a rushton turbine stirred mixer, *Experiments in Fluids* **8**, 153–160.

Yianneskis, M., Popiolek, Z. and Whitelaw, J.: 1987, An experimental study of the steady and unsteady flow characteristics of stirred reactors, *Journal of Fluid Mechanics* **175**, 537–555.

Appendix A

Single phase results data

A.1 Mean Velocity Data

Table A.1: Mean velocity data for the Bulk Tank

$N(RPM)$	$U_\theta(m/s)$
310	0.027
630	0.04
940	0.066
1260	0.073

Table A.2: Mean velocity data for the Impeller Stream

$N(RPM)$	$U_\theta(m/s)$
310	0.15
630	0.29
940	0.42
1260	0.57

Table A.3: Mean velocity data at the Impeller Tip

$N(RPM)$	$U_\theta(m/s)$
310	0.59
630	1.2
940	1.81
1260	2.28

A.2 RMS Velocity Data

Table A.4: RMS velocity data for the Bulk Tank

$N(RPM)$	$u'(m/s)$
310	0.04136
630	0.08482
940	0.1271
1260	0.1712

Table A.5: RMS velocity data for the Impeller Stream

$N(RPM)$	$u'(m/s)$
310	0.1381
630	0.2848
940	0.4206
1260	0.5694

Table A.6: RMS velocity data at the Impeller Tip

$N(RPM)$	$u'(m/s)$
310	0.1196
630	0.2366
940	0.3460
1260	0.4674

A.3 Turbulent Dissipation Rate data

Table A.7: Turbulent Dissipation Rate data for the Bulk Tank

$N(RPM)$	$\epsilon(m^2/s^3)$
310	0.006928
630	0.05860
940	0.2014
1260	0.4736

Table A.8: Turbulent Dissipation Rate data for the Impeller Stream

$N(RPM)$	$\epsilon(m^2/s^3)$
310	0.6069
630	5.340
940	17.66
1260	42.90

Table A.9: Turbulent Rate data at the Impeller Tip

$N(RPM)$	$\epsilon(m^2/s^3)$
310	1.938
630	15.03
940	46.64
1260	114.8

A.4 Power Draw data

Table A.10: Power draw data for various impeller speeds

$N(RPM)$	$P(W/kg)$
310	0.08
630	0.69
940	2.3
1260	5.51

Appendix B

Multiphase model results data

B.1 Mean Velocity Data

Table B.1: Mean velocity data for the Bulk Tank - MRF model

	Grid 1	Grid 2	Grid 3	Grid 4	Grid SM
$U_\theta(m/s)$	0.05166	0.04693	0.03978	0.04922	0.05318

Table B.2: Mean velocity data for the Bulk Tank - SM model

	IR	GH 1	GH 2	GH 3	GH 4
$U_\theta(m/s)$	10	0.005656	0.02976	0.02990	0.04480
$U_\theta(m/s)$	20	0.008869	0.03022	0.03066	0.04633
$U_\theta(m/s)$	30	0.01019	0.03844	0.03905	0.04725

Table B.3: Mean velocity data for the Impeller Stream - MRF Model

	Grid 1	Grid 2	Grid 3	Grid 4	Grid SM
$U_\theta(m/s)$	0.4315	0.4043	0.4382	0.4223	0.4490

Table B.4: Mean velocity data for the Impeller Stream - SM model

	IR	GH 1	GH 2	GH 3	GH 4
$U_\theta(m/s)$	10	0.009891	0.4470	0.4518	0.4283
$U_\theta(m/s)$	20	0.03835	0.4240	0.4364	0.4284
$U_\theta(m/s)$	30	0.04793	0.4265	0.4382	0.4281

Table B.5: Mean velocity data at the Impeller Tip - MRF Model

	Grid 1	Grid 2	Grid 3	Grid 4	Grid SM
$U_\theta(m/s)$	1.598	1.608	1.638	1.618	1.633

Table B.6: Mean velocity data at the Impeller Tip - SM model

	IR	GH 1	GH 2	GH 3	GH 4
$U_\theta(m/s)$	10	1.502	1.772	1.767	1.789
$U_\theta(m/s)$	20	1.559	1.801	1.791	1.787
$U_\theta(m/s)$	30	1.574	1.800	1.790	1.788

B.2 Turbulent RMS Velocity Data

Table B.7: RMS velocity data for the Bulk Tank - MRF Model

	Grid 1	Grid 2	Grid 3	Grid 4	Grid SM
$u'(m/s)$	0.09519	0.09804	0.1029	0.1055	0.1042

Table B.8: RMS velocity data for the Bulk Tank - SM model

	IR	GH 1	GH 2	GH 3	GH 4
$u'(m/s)$	10	0.1985	0.1400	0.1396	0.1131
$u'(m/s)$	20	0.1044	0.1146	0.1135	0.1104
$u'(m/s)$	30	0.08734	0.1183	0.1184	0.1061

Table B.9: RMS velocity data for the Impeller Stream - MRF Model

	Grid 1	Grid 2	Grid 3	Grid 4	Grid SM
$u'(m/s)$	0.3424	0.3419	0.3509	0.3606	0.3169

Table B.10: RMS velocity data for the Impeller Stream - SM model

	IR	GH 1	GH 2	GH 3	GH 4
$u'(m/s)$	10	0.009891	0.3844	0.3827	0.3802
$u'(m/s)$	20	0.03835	0.3828	0.3829	0.3798
$u'(m/s)$	30	0.04793	0.3818	0.3821	0.3791

Table B.11: RMS velocity data at the Impeller Tip - MRF Model

	Grid 1	Grid 2	Grid 3	Grid 4	Grid SM
$u'(m/s)$	0.2806	0.2853	0.2907	0.2971	0.2984

Table B.12: RMS velocity data at the Impeller Tip - SM model

	IR	GH 1	GH 2	GH 3	GH 4
$u'(m/s)$	10	0.2853	0.3182	0.3112	0.3426
$u'(m/s)$	20	0.2354	0.3441	0.3426	0.3196
$u'(m/s)$	30	0.2285	0.3212	0.3135	0.3202

B.3 Turbulent Dissipation Rate data

Table B.13: Turbulent Dissipation Rate data for the Bulk Tank - MRF Model

	Grid 1	Grid 2	Grid 3	Grid 4	Grid SM
$\epsilon(m^2/s^3)$	0.08353	0.08740	0.1021	0.1040	0.1010

Table B.14: Turbulent Dissipation Rate data for the Bulk Tank - SM model

	IR	GH 1	GH 2	GH 3	GH 4
$\epsilon(m^2/s^3)$	10	0.2867	0.1542	0.1533	0.1229
$\epsilon(m^2/s^3)$	20	0.07339	0.1268	0.1224	0.1179
$\epsilon(m^2/s^3)$	30	0.06257	0.1411	0.1408	0.1080

Table B.15: Turbulent Dissipation Rate data for the Impeller Stream - MRF Model

	Grid 1	Grid 2	Grid 3	Grid 4	Grid SM
$\epsilon(m^2/s^3)$	9.624	9.375	9.745	10.97	8.286

Table B.16: Turbulent Dissipation Rate data for the Impeller Stream - SM model

	IR	GH 1	GH 2	GH 3	GH 4
$\epsilon(m^2/s^3)$	10	8.953	11.84	11.79	12.65
$\epsilon(m^2/s^3)$	20	8.466	12.72	12.67	12.62
$\epsilon(m^2/s^3)$	30	8.487	12.79	12.72	12.64

Table B.17: Turbulent Dissipation Rate data at the Impeller Tip - MRF Model

	Grid 1	Grid 2	Grid 3	Grid 4	Grid SM
$\epsilon(m^2/s^3)$	13.44	14.41	15.25	19.18	12.19

Table B.18: Turbulent Dissipation Rate data at the Impeller Tip - SM model

	IR	GH 1	GH 2	GH 3	GH 4
$\epsilon(m^2/s^3)$	10	18.14	25.18	23.55	27.04
$\epsilon(m^2/s^3)$	20	10.81	27.34	27.05	26.02
$\epsilon(m^2/s^3)$	30	10.02	26.46	24.45	26.22

B.4 Power Draw Data

Table B.19: Power draw data - MRF Model

	Grid 1	Grid 2	Grid 3	Grid 4	Grid SM
$P(W/kg)$	1.893	1.938	1.933	2.006	1.863

Table B.20: Power draw data - SM model

	IR	GH 1	GH 2	GH 3	GH 4
$P(W/kg)$	10	2.183	1.978	2.067	2.153
$P(W/kg)$	20	2.117	2.125	2.197	2.155
$P(W/kg)$	30	2.115	2.118	2.195	2.166

B.5 Gas hold up Data

Table B.21: Gas hold up data - MRF Model

	Grid 1	Grid 2	Grid 3	Grid 4	Grid SM
ϕ	0.04104	0.03730	0.03209	0.04137	0.03238

Table B.22: Gas hold up data - SM model

	IR	GH 1	GH 2	GH 3	GH 4
ϕ	10	0.003997	0.02607	0.05418	0.02999
ϕ	20	0.004010	0.02983	0.05813	0.03050
ϕ	30	0.004785	0.03169	0.05945	0.03147

Appendix C

Comparative Data

C.1 Single Phase Data

C.1.1 Mean Velocity Profile Data

Table C.1: Normalized radial velocity profiles at r/T = 0185

z/H	310	630	940	1260
0.2333	0.0005993	0.001289	0.0006579	0.001935
0.2466	0.01213	0.01483	0.01536	0.01592
0.2600	0.01778	0.02083	0.02200	0.02208
0.2733	0.02310	0.02656	0.02851	0.02800
0.2866	0.02759	0.03164	0.03456	0.03338
0.3000	0.02581	0.03083	0.03530	0.03313
0.3133	0.1572	0.1558	0.1349	0.1516
0.3266	0.5323	0.5326	0.4855	0.5245
0.3400	0.7320	0.7457	0.7630	0.7519
0.3533	0.3468	0.3447	0.3783	0.3496
0.3666	0.06421	0.06020	0.05770	0.05826
0.3800	0.01479	0.01810	0.008510	0.01627
0.3933	0.02089	0.02702	0.01742	0.02526
0.4066	0.02077	0.02610	0.01769	0.02426
0.4200	0.01992	0.02449	0.01798	0.02267
0.4333	0.01950	0.02366	0.01838	0.02195

Table C.2: Normalized tangential velocity profiles at r/T = 0185

z/H	310	630	940	1260
0.2333	0.001076	0.001438	0.004820	0.001245
0.2466	0.002663	0.003167	0.004102	0.0007172
0.2600	0.004096	0.004697	0.003104	0.002346
0.2733	0.004943	0.005562	0.002891	0.003239
0.2866	0.0009488	0.001283	0.008398	0.001167
0.3000	0.06420	0.06413	0.07159	0.06585
0.3133	0.3815	0.3745	0.3462	0.3677
0.3266	0.6611	0.6648	0.6538	0.6635
0.3400	0.7367	0.7424	0.7505	0.7447
0.3533	0.5774	0.5750	0.5925	0.5776
0.3666	0.2499	0.2322	0.2253	0.2276
0.3800	0.08882	0.06736	0.03321	0.05805
0.3933	0.03974	0.02092	0.01146	0.01165
0.4066	0.03785	0.01917	0.01253	0.009705
0.4200	0.03832	0.01972	0.01157	0.009931
0.4333	0.03907	0.02050	0.01047	0.01049

C.1.2 Turbulent Kinetic Energy Data

Table C.3: Normalized TKE profile data for 310 and 630 RPM (r/T = 0.185)

z/H	630 RPM	310 RPM
0.2333	0.005031	0.005004
0.2350	0.005086	0.005063
0.2405	0.005218	0.005218
0.2461	0.005293	0.005309
0.2517	0.005402	0.005419
0.2573	0.005594	0.005595
0.2629	0.005937	0.005901
0.2685	0.006494	0.006398
0.2741	0.007335	0.007156
0.2797	0.008585	0.008302
0.2853	0.01059	0.01020
0.2909	0.01431	0.01387
0.2965	0.02084	0.02062
0.3021	0.03009	0.03050
0.3049	0.03464	0.03545
0.3077	0.03884	0.03999
0.3105	0.04322	0.04460
0.3133	0.04706	0.04853
0.3161	0.05004	0.05150
0.3189	0.05200	0.05339
0.3217	0.05287	0.05417
0.3245	0.05276	0.05398
0.3273	0.05184	0.05305
0.3301	0.05040	0.05169
0.3329	0.04881	0.05026
0.3357	0.04750	0.04914
0.3385	0.04695	0.04877
0.3413	0.04738	0.04933
0.3441	0.04876	0.05080
0.3469	0.05077	0.05292
0.3497	0.05293	0.05523
0.3525	0.05472	0.05722
0.3552	0.05568	0.05844
0.3580	0.05550	0.05854
0.3608	0.05404	0.05733
0.3636	0.05136	0.05484
0.3664	0.04826	0.05182
0.3692	0.04342	0.04687
0.3748	0.03041	0.03305
0.3804	0.01946	0.02106
0.3860	0.01255	0.01335
0.3916	0.009009	0.009409
0.3972	0.007098	0.007357
0.4028	0.005895	0.006127
0.4084	0.005073	0.005316
0.4140	0.004512	0.004769
0.4196	0.004145	0.004407
0.4252	0.003918	0.004175
0.4308	0.003800	0.004044
0.4333	0.003786	0.004011

Table C.4: Normalized TKE profile data for 310 and 630 RPM (r/T = 0.285)

z/H	630 RPM	310 RPM
0.2333	0.004662	0.004587
0.2350	0.004670	0.004595
0.2405	0.004696	0.004618
0.2461	0.004708	0.004628
0.2517	0.004716	0.004634
0.2573	0.004745	0.004657
0.2629	0.004804	0.004707
0.2685	0.004898	0.004790
0.2741	0.005048	0.004929
0.2797	0.005302	0.005178
0.2853	0.005803	0.005681
0.2909	0.006936	0.006819
0.2965	0.009586	0.009398
0.3021	0.01529	0.01472
0.3049	0.01979	0.01886
0.3077	0.02538	0.02401
0.3105	0.03180	0.02992
0.3133	0.03862	0.03625
0.3161	0.04543	0.04269
0.3189	0.05185	0.04886
0.3217	0.05749	0.05444
0.3245	0.06209	0.05915
0.3273	0.06551	0.06280
0.3301	0.06775	0.06535
0.3329	0.06903	0.06693
0.3357	0.06965	0.06780
0.3385	0.06993	0.06824
0.3413	0.07019	0.06855
0.3441	0.07058	0.06893
0.3469	0.07108	0.06942
0.3497	0.07148	0.06989
0.3525	0.07151	0.07012
0.3552	0.07084	0.06981
0.3580	0.06920	0.06870
0.3608	0.06646	0.06660
0.3636	0.06261	0.06345
0.3664	0.05785	0.05937
0.3692	0.05187	0.05401
0.3748	0.03886	0.04163
0.3804	0.02718	0.02977
0.3860	0.01767	0.01964
0.3916	0.01118	0.01240
0.3972	0.007491	0.008097
0.4028	0.005720	0.005956
0.4084	0.004953	0.005009
0.4140	0.004626	0.004596
0.4196	0.004479	0.004401
0.4252	0.004403	0.004292
0.4308	0.004354	0.004223
0.4333	0.004335	0.004200

Table C.5: Normalized TKE profile data for 940 and 1260 RPM (r/T = 0.185)

z/H	1260 RPM	940 RPM
0.2333	0.005062	0.005291
0.2350	0.005118	0.005358
0.2405	0.005241	0.005469
0.2461	0.005301	0.005457
0.2517	0.005403	0.005482
0.2573	0.005600	0.005615
0.2629	0.005959	0.005937
0.2685	0.006543	0.006518
0.2741	0.007422	0.007429
0.2797	0.008723	0.008800
0.2853	0.01080	0.01099
0.2909	0.01458	0.01486
0.2965	0.02109	0.02114
0.3021	0.03016	0.02937
0.3049	0.03456	0.03312
0.3077	0.03860	0.03652
0.3105	0.04286	0.04026
0.3133	0.04660	0.04369
0.3161	0.04952	0.04654
0.3189	0.05145	0.04860
0.3217	0.05231	0.04975
0.3245	0.05221	0.05004
0.3273	0.05131	0.04960
0.3301	0.04990	0.04863
0.3329	0.04834	0.04746

z/H	1260 RPM	940 RPM
0.3357	0.04707	0.04656
0.3385	0.04662	0.04648
0.3413	0.04718	0.04747
0.3441	0.04869	0.04947
0.3469	0.05081	0.05215
0.3497	0.05303	0.05489
0.3525	0.05482	0.05706
0.3552	0.05573	0.05820
0.3580	0.05543	0.05800
0.3608	0.05382	0.05630
0.3636	0.05098	0.05313
0.3664	0.04770	0.04928
0.3692	0.04275	0.04345
0.3748	0.02976	0.02880
0.3804	0.01907	0.01747
0.3860	0.01246	0.01104
0.3916	0.009093	0.008043
0.3972	0.007264	0.006508
0.4028	0.006088	0.005556
0.4084	0.005254	0.004885
0.4140	0.004658	0.004389
0.4196	0.004247	0.004026
0.4252	0.003979	0.003771
0.4308	0.003821	0.003608
0.4333	0.003571	0.003792

Table C.6: Normalized TKE profile data for 940 and 1260 RPM (r/T = 0.285)

z/H	1260 RPM	940 RPM
0.2333	0.004763	0.005001
0.2350	0.004770	0.005016
0.2405	0.004784	0.005042
0.2461	0.004786	0.005031
0.2517	0.004783	0.004990
0.2573	0.004800	0.004954
0.2629	0.004851	0.004950
0.2685	0.004940	0.004981
0.2741	0.005078	0.005049
0.2797	0.005305	0.005169
0.2853	0.005732	0.005391
0.2909	0.006675	0.005855
0.2965	0.008915	0.006934
0.3021	0.01401	0.009611
0.3049	0.01826	0.01223
0.3077	0.02378	0.01626
0.3105	0.03028	0.02168
0.3133	0.03730	0.02826
0.3161	0.04439	0.03557
0.3189	0.05112	0.04309
0.3217	0.05706	0.05027
0.3245	0.06192	0.05665
0.3273	0.06553	0.06189
0.3301	0.06789	0.06577
0.3329	0.06924	0.06836

z/H	1260 RPM	940 RPM
0.3357	0.06986	0.06986
0.3385	0.07012	0.07054
0.3413	0.07032	0.07078
0.3441	0.07064	0.07089
0.3469	0.07108	0.07108
0.3497	0.07146	0.07137
0.3525	0.07149	0.07162
0.3552	0.07085	0.07161
0.3580	0.06929	0.07105
0.3608	0.06666	0.06972
0.3636	0.06296	0.06749
0.3664	0.05837	0.06442
0.3692	0.05259	0.06012
0.3748	0.03991	0.04938
0.3804	0.02838	0.03787
0.3860	0.01875	0.02664
0.3916	0.01196	0.01732
0.3972	0.007965	0.01077
0.4028	0.005993	0.007025
0.4084	0.005122	0.005247
0.4140	0.004741	0.004481
0.4196	0.004566	0.004144
0.4252	0.004474	0.003976
0.4308	0.004417	0.003881
0.4333	0.004395	0.003852

C.2 Data for Gas Hold Up investigation

C.2.1 Mean Velocity Data

Table C.7: Normalized radial velocity profile data for GH1

z/H	10 IR	20 IR	30 IR
0.2333	0.02415	0.002445	0.006643
0.2466	0.01724	0.006174	0.01089
0.2600	0.01079	0.008545	0.01365
0.2733	0.007331	0.009483	0.01472
0.2866	0.004678	0.01150	0.01691
0.3000	0.06253	0.03213	0.03655
0.3133	0.2423	0.1812	0.1818
0.3266	0.5218	0.4947	0.4942
0.3400	0.6332	0.6735	0.6896
0.3533	0.4089	0.4008	0.3900
0.3666	0.1810	0.1334	0.1142
0.3800	0.04985	0.007478	0.007008
0.3933	0.004564	0.01195	0.001002
0.4066	0.009260	0.01175	0.003990
0.4200	0.01358	0.01078	0.006088
0.4333	0.01839	0.009208	0.009267

Table C.8: Normalized radial velocity profile data for GH2

z/H	10 IR	20 IR	30 IR
0.2333	0.005107	0.02241	0.02515
0.2466	0.01071	0.03146	0.03469
0.2600	0.01563	0.03955	0.04322
0.2733	0.01795	0.04347	0.04734
0.2866	0.02100	0.04980	0.05403
0.3000	0.02506	0.04739	0.05161
0.3133	0.1502	0.1425	0.1473
0.3266	0.4977	0.4827	0.4889
0.3400	0.6882	0.7260	0.7281
0.3533	0.3901	0.4166	0.4123
0.3666	0.09750	0.09820	0.09821
0.3800	0.007122	0.004189	0.01407
0.3933	0.01628	0.006372	0.01851
0.4066	0.01407	0.009413	0.02030
0.4200	0.01302	0.01052	0.02079
0.4333	0.01198	0.01177	0.02131

Table C.9: Normalized radial velocity profile data for GH3

z/H	10 IR	20 IR	30 IR
0.2333	0.003032	0.02176	0.02415
0.2466	0.008105	0.02999	0.03283
0.2600	0.01255	0.03734	0.04063
0.2733	0.01463	0.04094	0.04445
0.2866	0.01736	0.04675	0.05067
0.3000	0.02257	0.04368	0.04760
0.3133	0.1499	0.1407	0.1449
0.3266	0.4990	0.4818	0.4866
0.3400	0.6826	0.7214	0.7226
0.3533	0.3748	0.4063	0.4019
0.3666	0.08897	0.09053	0.08794
0.3800	0.007481	0.003472	0.01305
0.3933	0.01498	0.006614	0.01935
0.4066	0.01288	0.009892	0.02177
0.4200	0.01201	0.01096	0.02235
0.4333	0.01125	0.01201	0.02276

Table C.10: Normalized radial velocity profile data for GH4

z/H	10 IR	20 IR	30 IR
0.2333	0.02524	0.02567	0.02763
0.2466	0.03492	0.03562	0.03801
0.2600	0.04342	0.04443	0.04715
0.2733	0.04747	0.04861	0.05148
0.2866	0.05397	0.05537	0.05849
0.3000	0.05054	0.05196	0.05495
0.3133	0.1435	0.1447	0.1459
0.3266	0.4838	0.4848	0.4852
0.3400	0.7224	0.7226	0.7240
0.3533	0.4140	0.4155	0.4181
0.3666	0.1015	0.1035	0.1059
0.3800	0.01123	0.01267	0.01525
0.3933	0.01421	0.01522	0.01816
0.4066	0.01694	0.01792	0.02088
0.4200	0.01775	0.01869	0.02165
0.4333	0.01850	0.01936	0.02233

Table C.11: Normalized tangential velocity profile data for GH1

z/H	10 IR	20 IR	30 IR
0.2333	0.03393	0.002820	0.004691
0.2466	0.03570	0.003391	0.005725
0.2600	0.03664	0.004255	0.007041
0.2733	0.03735	0.004633	0.007637
0.2866	0.04463	0.003664	0.007090
0.3000	0.1135	0.03747	0.03367
0.3133	0.3367	0.2838	0.2801
0.3266	0.5221	0.5239	0.5232
0.3400	0.5570	0.5891	0.5991
0.3533	0.4447	0.4683	0.4674
0.3666	0.2422	0.2194	0.1929
0.3800	0.09087	0.03925	0.01183
0.3933	0.04833	0.009438	0.005851
0.4066	0.03855	0.005216	0.006913
0.4200	0.03632	0.004098	0.006735
0.4333	0.03416	0.002864	0.006080

Table C.12: Normalized tangential velocity profile data for GH2

z/H	10 IR	20 IR	30 IR
0.2333	0.0003492	0.01091	0.009814
0.2466	0.001214	0.009508	0.008439
0.2600	0.002729	0.007880	0.006778
0.2733	0.003553	0.007119	0.005978
0.2866	0.006244	0.005733	0.004476
0.3000	0.06314	0.05270	0.05168
0.3133	0.3416	0.3172	0.3176
0.3266	0.6137	0.6037	0.6038
0.3400	0.6902	0.7067	0.7067
0.3533	0.5591	0.5811	0.5796
0.3666	0.2629	0.2601	0.2600
0.3800	0.05003	0.02749	0.03514
0.3933	0.01874	0.005384	0.01645
0.4066	0.01582	0.004979	0.01668
0.4200	0.01529	0.005009	0.01706
0.4333	0.01487	0.005149	0.01772

Table C.13: Normalized tangential velocity profile data for GH3

z/H	10 IR	20 IR	30 IR
0.2333	0.0005794	0.008730	0.009276
0.2466	0.001373	0.007569	0.008013
0.2600	0.003239	0.006230	0.006514
0.2733	0.004223	0.005617	0.005806
0.2866	0.007297	0.004621	0.004603
0.3000	0.06510	0.05362	0.05379
0.3133	0.3448	0.3222	0.3229
0.3266	0.6167	0.6049	0.6044
0.3400	0.6884	0.7035	0.7025
0.3533	0.5475	0.5712	0.5653
0.3666	0.2443	0.2424	0.2363
0.3800	0.04578	0.02838	0.03251
0.3933	0.01884	0.01018	0.01828
0.4066	0.01628	0.009939	0.01863
0.4200	0.01580	0.01007	0.01909
0.4333	0.01544	0.01037	0.01987

Table C.14: Normalized tangential velocity profile data for GH4

z/H	10 IR	20 IR	30 IR
0.2333	0.01563	0.01182	0.01507
0.2466	0.01385	0.01043	0.01375
0.2600	0.01166	0.008799	0.01208
0.2733	0.01058	0.008026	0.01123
0.2866	0.008435	0.006606	0.009519
0.3000	0.05300	0.05256	0.05447
0.3133	0.3174	0.3172	0.3169
0.3266	0.6010	0.6003	0.6001
0.3400	0.7032	0.7022	0.7025
0.3533	0.5834	0.5832	0.5843
0.3666	0.2711	0.2728	0.2756
0.3800	0.04948	0.05165	0.05264
0.3933	0.02861	0.03038	0.03093
0.4066	0.02880	0.03062	0.03123
0.4200	0.02924	0.03113	0.03178
0.4333	0.03002	0.03202	0.03274

C.2.2 Turbulent Kinetic Energy Data

Table C.15: Normalized TKE profile data for GH1 (r/T = 0.185)

z/H	10 IR	20 IR	30 IR
0.2333	0.004999	0.001860	0.001812
0.2402	0.005165	0.001876	0.001823
0.2471	0.005385	0.001920	0.001860
0.2540	0.005681	0.002008	0.001941
0.2609	0.006094	0.002162	0.002087
0.2678	0.006713	0.002409	0.002328
0.2747	0.007774	0.002793	0.002709
0.2816	0.01000	0.003466	0.003375
0.2885	0.01531	0.005106	0.004978
0.2954	0.02623	0.009719	0.009438
0.3022	0.04040	0.01895	0.01830
0.3091	0.04725	0.02648	0.02549
0.3160	0.04557	0.02803	0.02699
0.3229	0.04129	0.02634	0.02524
0.3298	0.03724	0.02311	0.02147
0.3367	0.03857	0.02288	0.01970
0.3436	0.04754	0.02909	0.02365
0.3505	0.05926	0.03781	0.02988
0.3574	0.06938	0.04418	0.03358
0.3643	0.07388	0.04482	0.03213
0.3712	0.06698	0.03578	0.02325
0.3781	0.05158	0.02185	0.01228
0.3850	0.03682	0.01194	0.006040
0.3919	0.02760	0.007786	0.003926
0.3988	0.02286	0.006248	0.003145
0.4057	0.02042	0.005488	0.002684
0.4126	0.01909	0.005015	0.002358
0.4195	0.01828	0.004675	0.002112
0.4264	0.01775	0.004415	0.001924
0.4333	0.01740	0.004210	0.001779

Table C.16: Normalized TKE profile data for GH2 (r/T = 0.185)

z/H	10 IR	20 IR	30 IR
0.2333	0.004130	0.003826	0.003910
0.2402	0.004226	0.003878	0.003960
0.2471	0.004378	0.003982	0.004062
0.2540	0.004613	0.004169	0.004249
0.2609	0.004969	0.004486	0.004567
0.2678	0.005520	0.005006	0.005089
0.2747	0.006443	0.005880	0.005969
0.2816	0.008263	0.007545	0.007637
0.2885	0.01250	0.01127	0.01135
0.2954	0.02183	0.01921	0.01923
0.3022	0.03602	0.03094	0.03086
0.3091	0.04705	0.04045	0.04022
0.3160	0.05125	0.04537	0.04504
0.3229	0.05036	0.04628	0.04591
0.3298	0.04586	0.04298	0.04260
0.3367	0.04374	0.04026	0.03971
0.3436	0.04912	0.04372	0.04261
0.3505	0.05884	0.05172	0.04961
0.3574	0.06582	0.05724	0.05402
0.3643	0.06464	0.05485	0.05106
0.3712	0.05174	0.04196	0.03882
0.3781	0.03306	0.02459	0.02283
0.3850	0.01909	0.01241	0.01168
0.3919	0.01253	0.007252	0.006917
0.3988	0.009903	0.005420	0.005182
0.4057	0.008662	0.004567	0.004346
0.4126	0.007961	0.004054	0.003834
0.4195	0.007502	0.003702	0.003484
0.4264	0.007182	0.003449	0.003236
0.4333	0.006950	0.003265	0.003062

Table C.17: Normalized TKE profile data for GH3 (r/T = 0.185)

z/H	10 IR	20 IR	30 IR
0.2333	0.004085	0.003792	0.003962
0.2402	0.004180	0.003837	0.004001
0.2471	0.004330	0.003931	0.004091
0.2540	0.004560	0.004106	0.004263
0.2609	0.004908	0.004406	0.004564
0.2678	0.005447	0.004904	0.005068
0.2747	0.006349	0.005750	0.005928
0.2816	0.008140	0.007379	0.007574
0.2885	0.01235	0.01107	0.01126
0.2954	0.02169	0.01903	0.01920
0.3022	0.03599	0.03094	0.03099
0.3091	0.04706	0.04045	0.04031
0.3160	0.05103	0.04503	0.04472
0.3229	0.04979	0.04555	0.04514
0.3298	0.04507	0.04220	0.04177

z/H	10 IR	20 IR	30 IR
0.3367	0.04302	0.03962	0.03918
0.3436	0.04875	0.04333	0.04263
0.3505	0.05893	0.05197	0.05062
0.3574	0.06587	0.05799	0.05566
0.3643	0.06378	0.05509	0.05189
0.3712	0.04987	0.04126	0.03822
0.3781	0.03121	0.02373	0.02182
0.3850	0.01804	0.01197	0.01113
0.3919	0.01205	0.007096	0.006683
0.3988	0.009674	0.005380	0.005091
0.4057	0.008533	0.004562	0.004302
0.4126	0.007877	0.004061	0.003811
0.4195	0.007444	0.003714	0.003472
0.4264	0.007139	0.003465	0.003232
0.4333	0.006920	0.003285	0.003063

Table C.18: Normalized TKE profile data for GH4 (r/T = 0.185)

z/H	10 IR	20 IR	30 IR
0.2333	0.003869	0.003942	0.003821
0.2402	0.003918	0.003990	0.003872
0.2471	0.004014	0.004086	0.003969
0.2540	0.004190	0.004261	0.004143
0.2609	0.004490	0.004563	0.004443
0.2678	0.004985	0.005063	0.004940
0.2747	0.005820	0.005908	0.005781
0.2816	0.007391	0.007501	0.007359
0.2885	0.01088	0.01103	0.01085
0.2954	0.01844	0.01862	0.01831
0.3022	0.02982	0.02993	0.02935
0.3091	0.03910	0.03905	0.03828
0.3160	0.04394	0.04377	0.04306
0.3229	0.04497	0.04475	0.04425
0.3298	0.04203	0.04181	0.04147

z/H	10 IR	20 IR	30 IR
0.3367	0.03943	0.03927	0.03901
0.3436	0.04234	0.04226	0.04197
0.3505	0.04971	0.04967	0.04925
0.3574	0.05517	0.05520	0.05470
0.3643	0.05328	0.05348	0.05312
0.3712	0.04144	0.04182	0.04178
0.3781	0.02503	0.02548	0.02565
0.3850	0.01305	0.01344	0.01360
0.3919	0.007734	0.008046	0.008144
0.3988	0.005782	0.006041	0.006100
0.4057	0.004855	0.005084	0.005122
0.4126	0.004292	0.004502	0.004528
0.4195	0.003906	0.004103	0.004120
0.4264	0.003631	0.003819	0.003829
0.4333	0.003434	0.003615	0.003619

Table C.19: Normalized TKE profile data for GH1 (r/T = 0.285)

z/H	10 IR	20 IR	30 IR
0.2333	0.004274	0.002175	0.002067
0.2402	0.004400	0.002168	0.002060
0.2471	0.004564	0.002167	0.002060
0.2540	0.004786	0.002173	0.002067
0.2609	0.005114	0.002189	0.002082
0.2678	0.005645	0.002221	0.002111
0.2747	0.006584	0.002287	0.002165
0.2816	0.008313	0.002451	0.002292
0.2885	0.01140	0.002952	0.002673
0.2954	0.01637	0.004508	0.003918
0.3022	0.02353	0.008731	0.007590
0.3091	0.03176	0.01674	0.01522
0.3160	0.03880	0.02640	0.02501
0.3229	0.04328	0.03454	0.03360
0.3298	0.04501	0.03808	0.03730
0.3367	0.04605	0.03849	0.03720
0.3436	0.04780	0.03974	0.03799
0.3505	0.04900	0.04194	0.04012
0.3574	0.04782	0.04159	0.03924
0.3643	0.04382	0.03666	0.03302
0.3712	0.03792	0.02833	0.02337
0.3781	0.03176	0.01963	0.01409
0.3850	0.02643	0.01277	0.007684
0.3919	0.02217	0.008264	0.004279
0.3988	0.01909	0.005875	0.002962
0.4057	0.01695	0.004764	0.002528
0.4126	0.01549	0.004253	0.002371
0.4195	0.01451	0.003992	0.002299
0.4264	0.01382	0.003829	0.002253
0.4333	0.01332	0.003711	0.002217

Table C.20: Normalized TKE profile data for GH2 (r/T = 0.285)

z/H	10 IR	20 IR	30 IR
0.2333	0.003784	0.003477	0.003514
0.2402	0.003763	0.003449	0.003486
0.2471	0.003765	0.003436	0.003474
0.2540	0.003800	0.003442	0.003481
0.2609	0.003894	0.003470	0.003512
0.2678	0.004112	0.003535	0.003580
0.2747	0.004630	0.003675	0.003726
0.2816	0.005894	0.004018	0.004077
0.2885	0.008783	0.004955	0.005029
0.2954	0.01436	0.007476	0.007585
0.3022	0.02332	0.01342	0.01363
0.3091	0.03444	0.02393	0.02432
0.3160	0.04505	0.03680	0.03737
0.3229	0.05327	0.04900	0.04961
0.3298	0.05734	0.05678	0.05719
0.3367	0.05859	0.05978	0.05994
0.3436	0.05946	0.06068	0.06074
0.3505	0.06001	0.06150	0.06145
0.3574	0.05808	0.06080	0.06027
0.3643	0.05210	0.05575	0.05430
0.3712	0.04264	0.04565	0.04322
0.3781	0.03224	0.03338	0.03039
0.3850	0.02300	0.02195	0.01906
0.3919	0.01580	0.01297	0.01080
0.3988	0.01115	0.007563	0.006325
0.4057	0.008559	0.005060	0.004478
0.4126	0.007229	0.004094	0.003821
0.4195	0.006557	0.003731	0.003581
0.4264	0.006180	0.003562	0.003472
0.4333	0.005954	0.003472	0.003418

Table C.21: Normalized TKE profile data for GH3 (r/T = 0.285)

z/H	10 IR	20 IR	30 IR
0.2333	0.003674	0.003443	0.003577
0.2402	0.003654	0.003408	0.003528
0.2471	0.003661	0.003390	0.003497
0.2540	0.003709	0.003389	0.003487
0.2609	0.003830	0.003412	0.003504
0.2678	0.004111	0.003479	0.003571
0.2747	0.004784	0.003644	0.003747
0.2816	0.006388	0.004084	0.004220
0.2885	0.009866	0.005311	0.005532
0.2954	0.01611	0.008481	0.008864
0.3022	0.02549	0.01536	0.01596
0.3091	0.03653	0.02638	0.02713
0.3160	0.04663	0.03894	0.03965
0.3229	0.05402	0.05026	0.05076
0.3298	0.05728	0.05704	0.05724

z/H	10 IR	20 IR	30 IR
0.3367	0.05813	0.05944	0.05947
0.3436	0.05890	0.06032	0.06035
0.3505	0.05909	0.06109	0.06099
0.3574	0.05635	0.05981	0.05908
0.3643	0.04952	0.05375	0.05198
0.3712	0.03964	0.04276	0.04005
0.3781	0.02932	0.03013	0.02705
0.3850	0.02057	0.01904	0.01631
0.3919	0.01408	0.01098	0.009179
0.3988	0.01011	0.006586	0.005699
0.4057	0.007984	0.004723	0.004366
0.4126	0.006911	0.004025	0.003887
0.4195	0.006363	0.003746	0.003693
0.4264	0.006049	0.003604	0.003592
0.4333	0.005857	0.003520	0.003536

Table C.22: Normalized TKE profile data for GH4 at 10 IR (r/T = 0.285)

z/H	10 IR
0.2333	0.003674
0.2402	0.003654
0.2471	0.003661
0.2540	0.003709
0.2609	0.003830
0.2678	0.004111
0.2747	0.004784
0.2816	0.006388
0.2885	0.009866
0.2954	0.01611
0.3022	0.02549
0.3091	0.03653
0.3160	0.04663
0.3229	0.05402
0.3298	0.05728
0.3367	0.05813
0.3436	0.05890
0.3505	0.05909
0.3574	0.05635
0.3643	0.04952
0.3712	0.03964
0.3781	0.02932
0.3850	0.02057
0.3919	0.01408
0.3988	0.01011
0.4057	0.007984
0.4126	0.006911
0.4195	0.006363
0.4264	0.006049
0.4333	0.005857

Table C.23: Normalized TKE profile data for GH4 at 20 and 30 IR (r/T = 0.285)

z/H	20 IR	30 IR
0.2333	0.003448	0.003821
0.2402	0.003438	0.003872
0.2471	0.003443	0.003969
0.2540	0.003465	0.004143
0.2609	0.003510	0.004443
0.2678	0.003589	0.004940
0.2747	0.003738	0.005781
0.2816	0.004067	0.007359
0.2885	0.004928	0.01085
0.2954	0.007239	0.01831
0.3022	0.01282	0.02935
0.3091	0.02301	0.03828
0.3160	0.03579	0.04306
0.3229	0.04805	0.04425
0.3298	0.05590	0.04147
0.3367	0.05893	0.03901
0.3436	0.05988	0.04197
0.3505	0.06073	0.04925
0.3574	0.05988	0.05470
0.3643	0.05431	0.05312
0.3712	0.04340	0.04178
0.3781	0.03052	0.02565
0.3850	0.01915	0.01360
0.3919	0.01100	0.008144
0.3988	0.006638	0.006100
0.4057	0.004813	0.005122
0.4126	0.004115	0.004528
0.4195	0.003820	0.004120
0.4264	0.003659	0.003829
0.4333	0.003559	0.003619

C.3 Data for Grid Density investigation

C.3.1 Mean Velocity Profile Data

Table C.24: Normalized radial velocity profiles at r/T = 0185

z/H	Grid 1	Grid 2	Grid 3	Grid 4	Grid SM
0.2333	0.002030	0.006636	0.006781	0.01060	0.01371
0.2466	0.007736	0.01269	0.001290	0.01736	0.02041
0.2600	0.01145	0.01708	0.002625	0.02275	0.02613
0.2733	0.01346	0.01948	0.004624	0.02592	0.02877
0.2866	0.01654	0.02325	0.007789	0.03090	0.03431
0.3000	0.02514	0.03261	0.02157	0.03921	0.05584
0.3133	0.1320	0.1326	0.1605	0.1278	0.1838
0.3266	0.4254	0.4238	0.4733	0.4107	0.4634
0.3400	0.6415	0.6449	0.6320	0.6672	0.6472
0.3533	0.4388	0.4498	0.3859	0.4688	0.3801
0.3666	0.1543	0.1674	0.1240	0.1832	0.1241
0.3800	0.02710	0.03712	0.02554	0.04376	0.01516
0.3933	0.005069	0.01218	0.01357	0.02184	0.004110
0.4066	0.005138	0.01193	0.01378	0.02096	0.005650
0.4200	0.006113	0.01263	0.01422	0.02058	0.006624
0.4333	0.007059	0.01319	0.01430	0.01991	0.007847

Table C.25: Normalized tangential velocity profiles at r/T = 0185

z/H	Grid 1	Grid 2	Grid 3	Grid 4	Grid SM
0.2333	0.01222	0.007022	0.009291	0.007001	0.01976
0.2466	0.01163	0.006457	0.009274	0.006474	0.01895
0.2600	0.01087	0.005614	0.009507	0.005608	0.01820
0.2733	0.01055	0.005245	0.009428	0.005327	0.01807
0.2866	0.01188	0.006461	0.006960	0.007272	0.02081
0.3000	0.05120	0.039437	0.03993	0.04304	0.07065
0.3133	0.3038	0.2859	0.3267	0.2943	0.3136
0.3266	0.5634	0.5615	0.5937	0.5619	0.5555
0.3400	0.6534	0.6433	0.6656	0.6757	0.6435
0.3533	0.5640	0.5711	0.5419	0.5892	0.5193
0.3666	0.2975	0.3033	0.2576	0.3378	0.2485
0.3800	0.07447	0.1303	0.05929	0.08219	0.05842
0.3933	0.03367	0.03236	0.03005	0.03582	0.03102
0.4066	0.03211	0.03033	0.02885	0.03328	0.02895
0.4200	0.03265	0.03070	0.02938	0.03344	0.02903
0.4333	0.03396	0.03191	0.03056	0.03456	0.02955

C.3.2 Turbulent Kinetic Energy Data

Table C.26: Normalized TKE profile data for Grids 1 - 3 (r/T = 0.185)

z/H	Grid 1	Grid 2	Grid 3
0.2333	0.002482	0.002877	0.003201
0.2350	0.002492	0.002889	0.003203
0.2397	0.002522	0.002901	0.003185
0.2445	0.002518	0.002877	0.003167
0.2493	0.002510	0.002856	0.003168
0.2541	0.002522	0.002865	0.003202
0.2589	0.002570	0.002920	0.003277
0.2637	0.002667	0.003031	0.003403
0.2685	0.002821	0.003210	0.003593
0.2733	0.003046	0.003469	0.003861
0.2781	0.003360	0.003831	0.004234
0.2829	0.003812	0.004339	0.004771
0.2877	0.004558	0.005124	0.005664
0.2925	0.006160	0.006652	0.007581
0.2973	0.009657	0.009961	0.01203
0.3021	0.01560	0.01625	0.02074
0.3054	0.02007	0.02152	0.02802
0.3088	0.02418	0.02630	0.03423
0.3122	0.02812	0.03052	0.03903
0.3155	0.03118	0.03358	0.04180
0.3189	0.03305	0.03517	0.04248
0.3222	0.03368	0.03536	0.04146
0.3256	0.03324	0.03444	0.03929
0.3289	0.03200	0.03281	0.03656
0.3323	0.03037	0.03090	0.03386

z/H	Grid 1	Grid 2	Grid 3
0.3357	0.02874	0.02909	0.03163
0.3390	0.02763	0.02782	0.03040
0.3424	0.02755	0.02755	0.03053
0.3457	0.02875	0.02852	0.03208
0.3491	0.03128	0.03080	0.03483
0.3525	0.03484	0.03425	0.03834
0.3558	0.03884	0.03850	0.04203
0.3592	0.04261	0.04295	0.04513
0.3625	0.04546	0.04674	0.04677
0.3659	0.04695	0.04899	0.04638
0.3692	0.04472	0.04717	0.04203
0.3740	0.03467	0.03753	0.03049
0.3788	0.02235	0.02519	0.01897
0.3836	0.01244	0.01455	0.01093
0.3884	0.007078	0.008373	0.006988
0.3932	0.004844	0.005671	0.005295
0.3980	0.003897	0.004509	0.004448
0.4028	0.003386	0.003886	0.003921
0.4076	0.003049	0.003480	0.003547
0.4124	0.002804	0.003188	0.003269
0.4172	0.002620	0.002972	0.003060
0.4220	0.002482	0.002813	0.002907
0.4268	0.002379	0.002700	0.002800
0.4316	0.002308	0.002627	0.002732
0.4333	0.002291	0.002612	0.002717

Table C.27: Normalized TKE profile data for Grid 4 (r/T = 0.185)

z/H	Grid 4
0.2333	0.003534
0.2350	0.003557
0.2397	0.003583
0.2445	0.003569
0.2493	0.003556
0.2541	0.003579
0.2589	0.003661
0.2637	0.003815
0.2685	0.004055
0.2733	0.004401
0.2781	0.004886
0.2829	0.005572
0.2877	0.006605
0.2925	0.008380
0.2973	0.01161
0.3021	0.01753
0.3042	0.02048
0.3063	0.02313
0.3084	0.02582
0.3105	0.02840
0.3126	0.03074

z/H	Grid 4
0.3147	0.03276
0.3168	0.03435
0.3189	0.03545
0.3210	0.03605
0.3231	0.03614
0.3252	0.03580
0.3273	0.03510
0.3294	0.03415
0.3315	0.03307
0.3336	0.03196
0.3357	0.03094
0.3378	0.03013
0.3399	0.02966
0.3420	0.02962
0.3441	0.03008
0.3462	0.03109
0.3483	0.03264
0.3504	0.03470
0.3524	0.03715
0.3545	0.03987
0.3566	0.04270

z/H	Grid 4
0.3587	0.04545
0.3608	0.04792
0.3629	0.04987
0.3650	0.05107
0.3671	0.05154
0.3692	0.04943
0.3740	0.03811
0.3788	0.02582
0.3836	0.01565
0.3884	0.009689
0.3932	0.006902
0.3980	0.005562
0.4028	0.004780
0.4076	0.004254
0.4124	0.003876
0.4172	0.003601
0.4220	0.003405
0.4268	0.003276
0.4316	0.003201
0.4333	0.003185

Table C.28: Normalized TKE profile data for Grids 1 - 3 (r/T = 0.285)

z/H	Grid 1	Grid 2	Grid 3
0.2333	0.002520	0.002954	0.003125
0.2350	0.002526	0.002940	0.003098
0.2397	0.002554	0.002888	0.003008
0.2445	0.002560	0.002832	0.002934
0.2493	0.002549	0.002785	0.002882
0.2541	0.002530	0.002752	0.002857
0.2589	0.002511	0.002736	0.002860
0.2637	0.002500	0.002739	0.002891
0.2685	0.002503	0.002759	0.002952
0.2733	0.002525	0.002800	0.003054
0.2781	0.002579	0.002870	0.003227
0.2829	0.002690	0.002992	0.003551
0.2877	0.002928	0.003222	0.004219
0.2925	0.003474	0.003710	0.005643
0.2973	0.004712	0.004782	0.008380
0.3021	0.007417	0.007112	0.01304
0.3054	0.01053	0.009916	0.01741
0.3088	0.01469	0.01382	0.02240
0.3122	0.01955	0.01857	0.02761
0.3155	0.02468	0.02377	0.03265
0.3189	0.02965	0.02902	0.03717
0.3222	0.03404	0.03391	0.04083
0.3256	0.03750	0.03803	0.04342
0.3289	0.03980	0.04112	0.04487
0.3323	0.04087	0.04302	0.04534
0.3357	0.04092	0.04382	0.04518
0.3390	0.04038	0.04385	0.04485
0.3424	0.03982	0.04359	0.04474
0.3457	0.03971	0.04350	0.04500
0.3491	0.04027	0.04383	0.04552
0.3525	0.04130	0.04455	0.04592
0.3558	0.04238	0.04532	0.04571
0.3592	0.04292	0.04569	0.04449
0.3625	0.04246	0.04520	0.04209
0.3659	0.04087	0.04362	0.03865
0.3692	0.03796	0.04061	0.03417
0.3740	0.03214	0.03450	0.02686
0.3788	0.02571	0.02757	0.01982
0.3836	0.01904	0.02041	0.01357
0.3884	0.01311	0.01406	0.008921
0.3932	0.008527	0.009196	0.006004
0.3980	0.005520	0.006047	0.004448
0.4028	0.003866	0.004328	0.003689
0.4076	0.003069	0.003492	0.003311
0.4124	0.002696	0.003091	0.003104
0.4172	0.002508	0.002884	0.002979
0.4220	0.002399	0.002768	0.002898
0.4268	0.002322	0.002698	0.002847
0.4316	0.002262	0.002657	0.002816
0.4333	0.002243	0.002649	0.002810

Table C.29: Normalized TKE profile data for Grid 4 (r/T = 0.285)

z/H	Grid 4
0.2333	0.003557
0.2350	0.003541
0.2397	0.003484
0.2445	0.003432
0.2493	0.003391
0.2541	0.003365
0.2589	0.003361
0.2637	0.003378
0.2685	0.003418
0.2733	0.003485
0.2781	0.003588
0.2829	0.003752
0.2877	0.004041
0.2925	0.004606
0.2973	0.005758
0.3021	0.008155
0.3042	0.009883
0.3063	0.01214
0.3084	0.01488
0.3105	0.01799
0.3126	0.02140

z/H	Grid 4
0.3147	0.02498
0.3168	0.02863
0.3189	0.03223
0.3210	0.03568
0.3231	0.03885
0.3252	0.04165
0.3273	0.04401
0.3294	0.04587
0.3315	0.04721
0.3336	0.04806
0.3357	0.04849
0.3378	0.04858
0.3399	0.04848
0.3420	0.04832
0.3441	0.04821
0.3462	0.04824
0.3483	0.04843
0.3504	0.04878
0.3525	0.04920
0.3545	0.04959
0.3566	0.04983

z/H	Grid 4
0.3587	0.04978
0.3608	0.04933
0.3629	0.04840
0.3650	0.04695
0.3671	0.04511
0.3692	0.04251
0.3740	0.03504
0.3788	0.02719
0.3836	0.01947
0.3884	0.01309
0.3932	0.008628
0.3980	0.005996
0.4028	0.004647
0.4076	0.003989
0.4124	0.003651
0.4172	0.003461
0.4220	0.003345
0.4268	0.003271
0.4316	0.003226
0.4333	0.003215

Table C.30: Normalized TKE profile data for Grid SM (r/T = 0.185)

z/H	Grid SM
0.2333	0.002847
0.2373	0.002834
0.2445	0.002846
0.2517	0.002912
0.2589	0.003058
0.2661	0.003314
0.2733	0.003728
0.2805	0.004424
0.2877	0.006008
0.2949	0.01075
0.3021	0.02227
0.3088	0.03561
0.3155	0.04441
0.3222	0.04876
0.3290	0.04502
0.3357	0.03909
0.3424	0.04352
0.3491	0.04881
0.3558	0.04838
0.3625	0.04401
0.3692	0.03228
0.3765	0.01720
0.3838	0.008535
0.3911	0.005386
0.3983	0.004280
0.4056	0.003701
0.4129	0.003316
0.4201	0.003041
0.4274	0.002844
0.4333	0.002731

Table C.31: Normalized TKE profile data for Grid SM (r/T = 0.285)

z/H	Grid SM
0.2333	0.002745
0.2373	0.002710
0.2445	0.002678
0.2517	0.002669
0.2589	0.002679
0.2661	0.002710
0.2676	0.002724
0.2733	0.002780
0.2805	0.002945
0.2877	0.003416
0.2949	0.004885
0.3021	0.009066
0.3088	0.01651
0.3155	0.02559
0.3222	0.03330
0.3289	0.03649
0.3357	0.03593
0.3424	0.03610
0.3491	0.03886
0.3558	0.04045
0.3625	0.03705
0.3692	0.02894
0.3765	0.01882
0.3837	0.01089
0.3909	0.006115
0.3981	0.004019
0.4038	0.003412
0.4053	0.003243
0.4126	0.002941
0.4198	0.002793
0.4270	0.002705
0.4333	0.002657